1

Microstructures of Metallic Materials from Additive Manufacturing

Coordinated by Christophe COLIN
Centre des Matériaux, Mines ParisTech, Évry, France

Microstructures resulting from metal additive manufacturing (AM) have, depending on the process, similarities with those resulting from multi-pass welding (wire arc additive manufacturing (WAAM) and laser metal deposition (LMD)), but also very specific characteristics, often associated with even faster fusion-solidification kinetics (laser powder bed fusion (L-PBF)). This chapter reviews the main classes of materials and alloys commonly tested in AM (steel, nickel, titanium and aluminum alloys) in order to describe the basic microstructural elements associated with the different processes and illustrate them with different representative alloys. As a preamble to this chapter, it would be interesting to briefly summarize some common characteristics of materials produced with AM and to return to the origin of the microstructures formed. We will limit the scope here to raw manufactured microstructures, with the effects of post-processing and the microstructure–mechanical properties relations being dealt with, respectively, in Chapters 2 and 3. All the concepts mentioned in this introduction are reviewed in a targeted manner in the sections specific to the different materials considered: steels, nickel-based alloys, titanium-based alloys and aluminum alloys.

First of all, the various processes considered here, which lead to fusion in the form of powder or wire (L-PBF, electron powder bed fusion (E-PBF), WAAM and

Additive Manufacturing of Metal Alloys 2,
coordinated by Patrice PEYRE and Éric CHARKALUK.

LMD), can be related to processes of microcasting or microwelding, with the formation of small melted areas moved in 3D leading to the construction of the part. What differentiates these different processes is the thermal cycle T = f(t) imposed on the material and its spatial distribution over time T = f (x, y, z, t), with speeds of cooling in proximity to the molten zone variable between 10^2 and 10^4 K/s (WAAM, LMD) or 10^5 and 10^7 K/s (L-PBF) (see section 1.2 on L-PBF in Chapter 1 of Volume 1) of Whatever the material considered, the grain structures are then conditioned by the thermal gradient G and the local velocity V_s of the isotherms, and in particular by the ratio G/V_s (for the solidification morphology: columnar, equiaxed, etc.), by the product $G.V_s$ (for the fineness of the microstructure) and by the annealing temperature T_r generated by the successive accumulation of the layers of material at all points of the already solidified material.

First of all, AM processes as a whole induce a particular kind of solidification due to the presence of a significant thermal gradient in the direction of manufacture (z-axis = BD (buildling direction)), which is most often located at the apex of the melt-pool (where the melting isotherm is perpendicular to the z-axis). This thermal characteristic, linked to the strong dilution in depth of one layer on another, often generates a columnar microstructure subject to selective grain growth. Each crystal system has preferential growth directions due to the anisotropy of the energy of the solid–liquid interface. For cubic materials, <001> directions are the preferred growth directions (Dong 2007). The dendrites will therefore grow in the <001> direction closest to the direction of the thermal gradient. The growth direction of grain 1 (Figure 1.1) is parallel to the main direction of the thermal gradient, unlike the growth direction of grains 2 (disorientation of about 20°) and 3 (misorientation of about –5°). As a result, the growth rate and undercooling of the grain 2 dendrites are greater than those of neighboring grains 1 and 3. The growth front of grain 2 is then positioned under those of the neighboring grains and ends up being blocked, and only grains 1 and 3 remain. This then results in a strong texture and anisotropy in the mechanical properties. Too much undercooling, associated with a high growth rate and/or an insufficient temperature gradient, can lead either to the nucleation of equiaxed grains (without preferential orientation) upstream of the solidification front or to the destabilization and fragmentation of the columnar dendritic front.

The growth of nuclei and/or fragments leads to a columnar-to-equiaxed transition (CET), translated by microstructure selection maps such as that proposed by Kou (2003), within which one can schematically position the four metal AM processes (Figure 1.2). We find there that the L-PBF process generally favors a very fine microstructure with a columnar and cellular growth mode, that the E-PBF and

DED-LMD processes induce less fine microstructures with essentially columnar growth modes and that the WAAM process generates a coarser columnar or equiaxed microstructure.

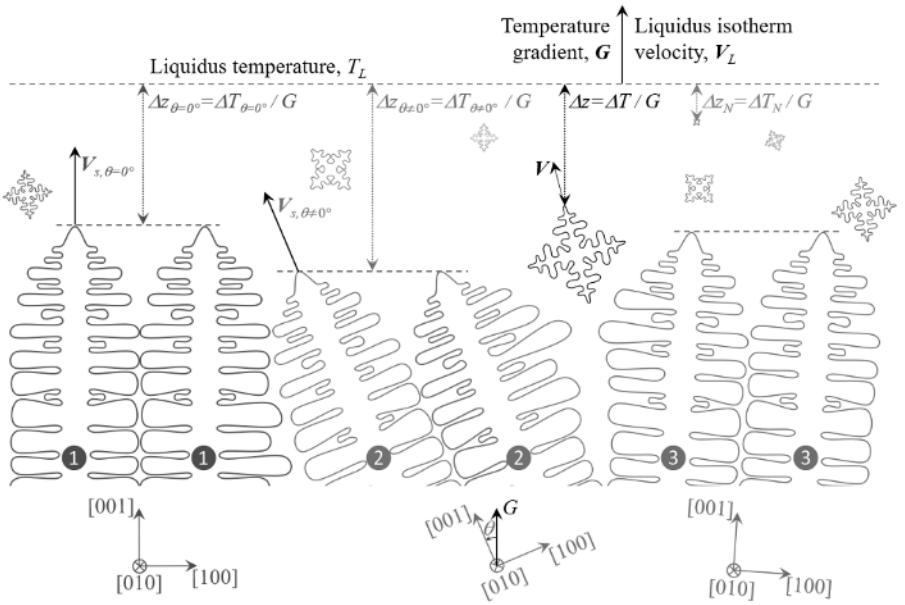

Figure 1.1. *Dendritic growth competition between columnar grains of different orientations (in red, green and blue) and equiaxed grains (in gray) germinating in the liquid during directional solidification at a constant temperature gradient G and isotherm velocity VL. Note that secondary dendrites can hardly be distinguished in L-PBF. For a color version of this figure, see www.iste.co.uk/peyre/alloys2.zip*

All concepts related to "rapid" solidification and the selection of microstructures are discussed in more detail in section 1.1.

In accordance with the value of the annealing temperature T_r reached at a point (x,y,z) of the part over time (local thermal history), the material, after solidification and until the part is finished, can undergo different metallurgical evolutions: (1) a fine precipitation starting from a supersaturated solid solution, (2) a transformation of the metastable phases into more stable phases, (3) a decomposition of the martensitic phases that can be accompanied by twinning to accommodate deformations (section 1.4 on titanium alloys), (4) homogenization of the composition (reduction in the size of chemical segregations), (5) partial recrystallization by annihilation of thermal dislocations and (6) an enlargement of the phases and finally a partial relaxation of the

internal stresses. All these microstructural changes can take place more or less simultaneously, because they are essentially governed by physical phenomena, such as diffusion, that intensify with temperature and time.

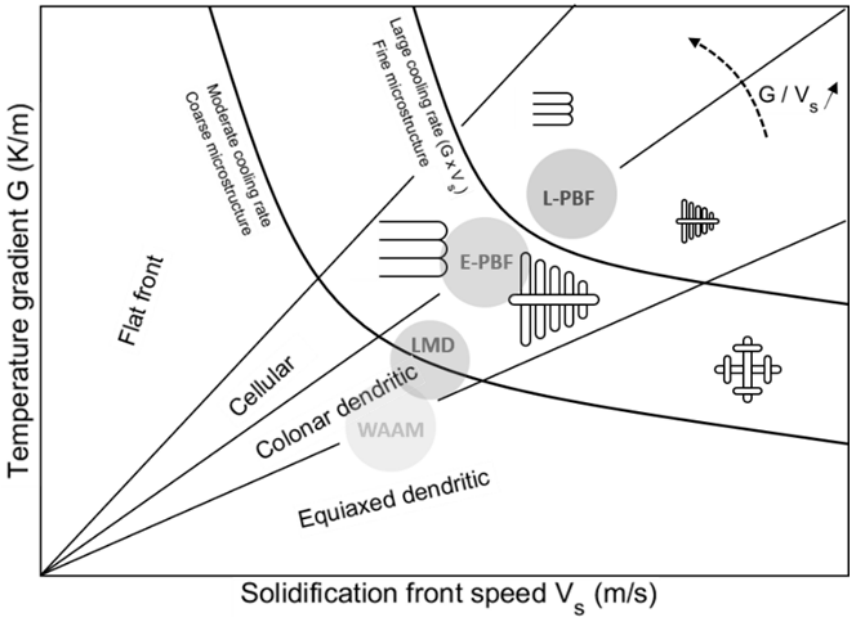

Figure 1.2. *Map of alloy solidification modes according to Kou (2003). For a color version of this figure, see www.iste.co.uk/peyre/alloys2.zip*

If we consider the microstructures resulting from the L-PBF process, which are perhaps more singular compared to typical processes (casting, forge), and if we compare them with those resulting from the three other additive processes, they present common characteristics, whatever the nature of the alloys produced:

– they are columnar, oriented in the direction of manufacture, which is the case for most of the processes mentioned above, with the exception of LMD and WAAM, which can induce equiaxed grains on solidification if the dilution between layers is low; the L-PBF process gives a much too low layer thickness (see Table 1.4 in Volume 1);

– they result from rapid solidification, potentially involving solid–liquid interfaces that are no longer in thermodynamic equilibrium, with high cooling rates ~10^5–10^7 K/s and solidification speeds between 0.1 and 1 m/s, which generally lead to a fine cellular microstructure (~1 µm), intercellular chemical segregation, and

supersaturation of the matrix in alloy elements (the case of steels, such as aluminum alloys). On this point, and because of the faster kinetics, the chemical segregations are lower and more localized than those resulting from other processes;

– they have, in the optimized state, a porosity between 0.01 and 0.5%; lack of fusion; and microcavities or keyhole porosities of sizes between 0.5 μm and 50 μm. In comparison, the LMD, E-PBF and WAAM processes generate fewer pores because they are formed under conditions with less energy concentration: (1) they generate less vaporization, (2) they have larger melt zones that promote degassing effects or (3) they are formed under a secondary vacuum (the case of E-PBF);

– they can present a variation in the chemical composition compared to that of the initial powder because of the phenomenon of selective vaporization (the case of the vaporization of aluminum in Ti-6Al-4V (section 1.4) or magnesium in aluminum alloys (section 1.5)). This phenomenon is less frequent with other less energy-intensive processes;

– they contain a high density of dislocations ($\sim 10^{11} cm^{-2}$) resulting from the rapid contraction of the liquid metal during its solidification, located near the intercellular spaces (Yan et al. 2017), which creates a form of "thermal hardening", often (with the exception of certain aluminum alloys) making the material "recrystallizable" during post-L-PBF annealing (Kreitcberg et al. 2017), with simultaneous formation of macles, and can result in fairly favorable mechanical properties (good compromise between mechanical strength and ductility: the case of stainless steels (section 1.2)). On this point, the LMD, E-PBF and WAAM processes have less capacity for recrystallization in the raw state;

– they accelerate the growth kinetics of precipitates during thermal post-processing due to the supersaturation of the matrix in alloying elements (the case of δ phase 5 in γ″-hardened superalloys (section 1.3)). On the other hand, processes such as WAAM, LMD and E-PBF generate more advanced states of precipitation in raw production conditions due to a more pronounced thermal annealing effect (average temperature during manufacture). In this regard, this thermal annealing effect often generates phase gradient materials (e.g. this is the case for a certain number of raw titanium alloys in LMD (section 1.4)).

1.1. Solidification microstructures from AM processes

The principles defining the formation of solidification structures in wide growth rate and temperature gradient ranges typical of AM processes are discussed here.

Section 1.1 written by Charles-André GANDIN.

The generated microstructures only rarely represent the thermodynamic equilibrium state. They are the result of competitions between nucleation and growth of phases in unsteady mass and energy transfer regimes. However, at the solid–liquid interface, thermodynamic equilibrium can be preserved. In cases of extreme velocities where it is not, solute trapping comes into play, complicating the explanation of microstructural morphologies and their phase and solute compositions.

1.1.1. *Introduction*

Solidification is present in AM processes involving a melting step. This is the case for powder bed fusion processes using a heat source (L-PBF and E-PBF); fusion processes with a projected powder (direct energy deposition (DED)), for example, using a laser source (LMD); or processes for depositing material by electric arc wire fusion (WAAM). These technologies are described in Chapter 1 of Volume 1.

The formation of a solid can occur below the characteristic temperature of thermodynamic equilibrium. For an alloy of composition w_0, this temperature is called the liquidus, $T_L^{\alpha l}$. It coincides with the eutectic temperature, $T_E^{\alpha\beta l}$, when the composition approaches that of the eutectic, $w_E^{\alpha\beta l}$. The size of the microstructure is strongly dependent on the temperature gradient, G, and the *solidification rate*, V_s, prevailing at the solid–liquid interface during growth. Thus, the primary, λ_1, and secondary, λ_2, dendritic spacings and the eutectic interlamellar spacing, λ_e, follow the following trends (Dantzig and Rappaz 2016):

$$\lambda_1 \propto G^{-1/2} V_s^{-1/4} \quad [1.1]$$

$$\lambda_2 \propto G^{-1/3} V_s^{-1/3} \quad [1.2]$$

$$\lambda_e \propto V_s^{-1/2} \quad [1.3]$$

A first estimate of G and V_s can be based on isotherms $T_L^{\alpha l}$ and $T_E^{\alpha\beta l}$. Moreover, in the case of directional growth, called columnar growth, the orientation of the microstructure can also be approximated by that of the temperature gradient. These first elements indicate the importance of the analysis of heat transfers to understand and control solidification microstructures.

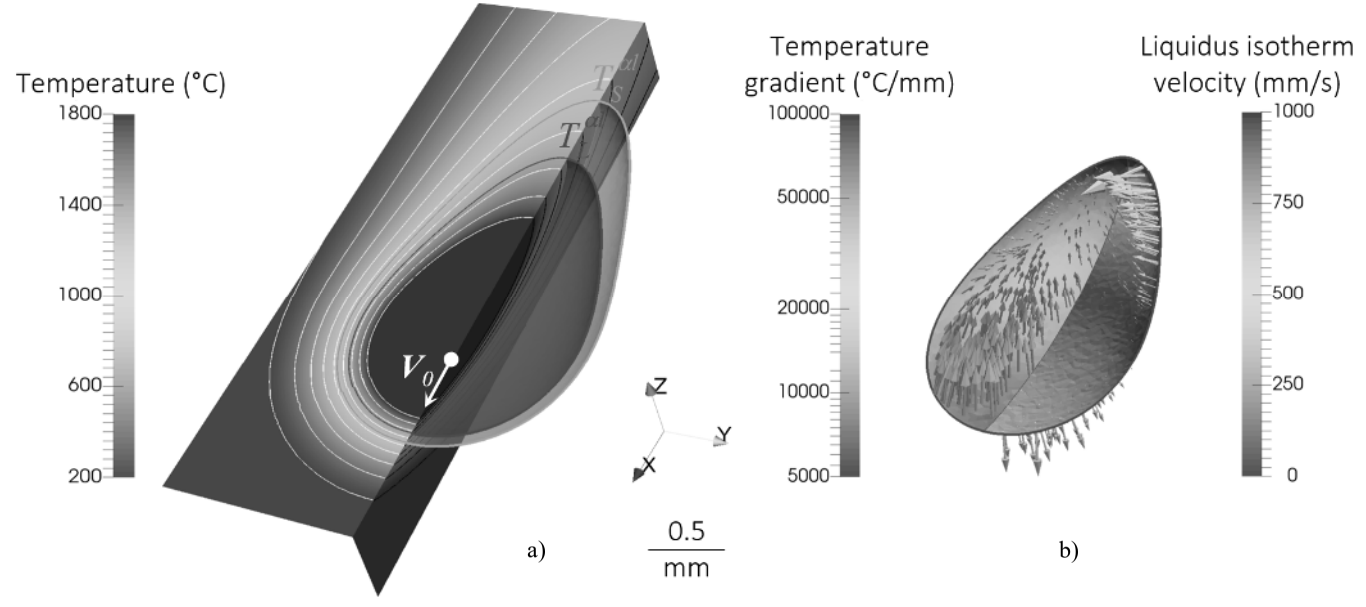

Figure 1.3. *Distributions (a) of the temperature and (b) of the temperature gradient and the velocity of the isotherm of the liquidus of the alloy, T_L^{α} (red surfaces and contours), representative of the diffusion of heat in a metallic material during an additive manufacturing process using a moving heat source V_0. For a color version of this figure, see www.iste.co.uk/peyre/alloys2.zip*

COMMENTS ON FIGURE 1.3.– *The melting of the material generates a melt-pool in the region of temperature above* T_L^{al} *and a mushy zone, that is, a mixture of solid and liquid phases, between* T_L^{al} *and the solidus isotherm of the alloy ((a), green surface and contour). Material: Inconel 718 with* $T_L^{al} = 1{,}337°C$ *and* $T_S^{al} = 1{,}075°C$*, according to Antonsson and Fredriksson 2005; thermal diffusivity,* $a_{th} = 10^{-5}\ m^2\ s^{-1}$*, thermal conductivity,* $K = 30\ W\ m^{-1}\ K^{-1}$*, initial temperature,* $T_0 = 20°C$*. Heat source according to the model from Cline and Anthony (1977): power,* $P_0 = 100\ W$*, standard deviation of the Gaussian distribution representing the spatial distribution of energy around the center of the heat source,* $10^{-4}\ m$*, velocity,* $V_0 = 1\ m\ s^{-1}$*. The central position of the heat source is represented by the white dot on the surface of the melt-pool.*

Figure 1.3 shows an illustration of a temperature field generating a liquid pool from the melting of a metallic material according to the model described by Cline and Anthony (1977). The material is characterized by its thermal diffusivity, a_{th}, its thermal conductivity, K, and its initial temperature, T_0. The heat source moves linearly at the speed V_0. It is also described by its power, P_0, and its spatial Gaussian distribution of energy, with the standard deviation representing here the diameter of the source. The temperature field at instant t is then given by an analytical formula. Other analytical forms exist, such as the solution from Rosenthal (1946), a simplified version of the Cline and Anthony's solution for a point heat source (i.e. zero standard deviation). The limitations of these solutions are numerous: purely stationary regimes, absence of the effect of convective transport and movements of the liquid–gas interface, constant properties with temperature, etc. Numerical modeling is therefore relevant in this context, as evidenced by Chapter 4 of Volume 1. However, the orders of magnitude given in Figure 1.3 are sufficient to realize the variations in G and V_s and, as a result of using equations [1.1]–[1.3], variations in microstructure size and orientation. In front of the heat source, the $T_L^{\alpha l}$ isotherm velocities shown in Figure 1.3 come out of the melt-pool, which represents the propagation of heat in the cold material, that is, fusion. Conversely, behind the heat source, the isotherm of the liquidus propagates toward the melt-pool already formed, indicating its cooling and therefore its solidification. Obviously, it is the region downstream from the heat source that interests us for the study of the formation of solidification microstructures. In this region, going up from the bottom of the melt-pool toward its upper surface behind the heat source, we also observe that G decreases as V_s increases. The ratio G/V_s is therefore high at the bottom of the melt-pool and low at its upper surface. This evolution is indicative of a columnar directional growth, from the bottom of the melt-pool, whereas an equiaxed growth is possible at the surface of the melt-pool (Hunt 1984). These analyses can be summarized in maps representing domains of G and V_s in which columnar and equiaxed microstructures are found (Kurz and Fisher 1998; Dantzig and Rappaz 2009) (example in Figure 1.2).

Given the speed and temperature gradient domains involved, the rest of this section describes a series of phenomena explaining the formation of solidified microstructures in AM processes, including high-speed solidification. The following concepts are introduced: growth kinetics and morphologies of microstructures, the thermodynamic equilibrium of the interface, the competition of growth between microstructures and the selection of grain structures. We limit ourselves to dendritic and eutectic structures, omnipresent in the transformations of metallic alloys from a liquid.

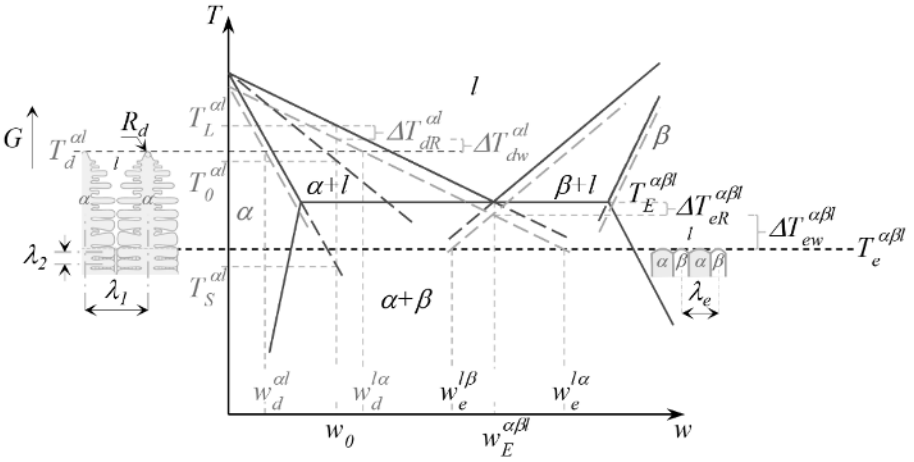

Figure 1.4. *Schematic representations (center) of a phase diagram for a binary alloy and of the dendritic (left) and eutectic (right) microstructures growing in a temperature gradient, G, with indication of the temperatures, lengths, curvature undercooling, chemical undercooling and characteristic chemical compositions. For a color version of this figure, see www.iste.co.uk/peyre/alloys2.zip*

COMMENTS ON FIGURE 1.4.– *The dashed lines schematize the equilibria in the presence of a curvature (in gray) and the T_0 lines (in red) (see text). The effects of solidification rate on the modification of thermodynamic equilibria are not included here.*

1.1.2. *Growth kinetics with local interface equilibrium*

The literature is rich in works explaining the kinetics and morphologies of solidification microstructures. We limit ourselves below to the case of binary alloys. In addition, we consider dilute alloys and a linearized representation of the phase diagram, as schematized in Figure 1.4: the slopes of the boundaries between

a single-phase liquid, l, crystalline solid domains, α and β, and a bi-phasic domain, $\alpha+l$, $\beta+l$ and $\alpha+\beta$, are constant. For the alloy with composition w_0 at a temperature T such that the solid α and liquid phases coexist, of respective solute chemical compositions $w^{\alpha l}$ and $w^{l\alpha}$, the thermodynamic equilibrium of the mixture is characterized by the partition coefficient $k^{\alpha l} = w^{\alpha l}/w^{l\alpha}$. In the example in Figure 1.4, $w^{\alpha l} < w^{l\alpha}$ in the biphasic domain $\alpha+l$, so that $k^{\alpha l} < 1$ at the interface between the solid α and the liquid, reflecting the chemical segregation of the solute in the liquid from the interface αl. When the solid α grows at the solidification rate V_s, the solute then accumulates in the liquid at the solid–liquid interface. Similarly, although the temperature can be deemed constant at the interface, the energy of the solid is lower than that of the liquid which, during solidification, releases heat. These segregated quantities, solute and energy, will have to be evacuated by diffusion in the liquid. Moreover, when the interface αl is not planar, its curvature adds an undercooling proportional to the s/l interfacial energy. Diffusive and curvature phenomena generate a deviation from the thermodynamic equilibrium, which is represented in Figure 1.4 by dendritic and eutectic undercooling $\Delta T_d^{\alpha l} = T_L^{\alpha l} - T_d^{\alpha l}$ and $\Delta T_e^{\alpha l} = T_E^{\alpha\beta l} - T_e^{\alpha\beta l}$, where $T_d^{\alpha l}$ and $T_e^{\alpha\beta l}$ are, respectively, the growth temperatures of the α dendritic and $\alpha+\beta$ eutectic microstructures. We can observe in Figure 1.4 that the eutectic structure is interdendritic, that is to say that it grows in the residual liquid with a composition close to the eutectic, $w_E^{\alpha\beta l}$, due to the accumulation of the solute rejected at the interface αl during dendritic growth. In directional growth, that is, in a temperature gradient G, the growth fronts are thus below the equilibrium temperatures $T_L^{\alpha l}$ and $T_E^{\alpha\beta l}$. This situation is encountered in AM where G/V_s is high, V_s can then be estimated using the velocity of isotherms $T_L^{\alpha l}$ and $T_E^{\alpha\beta l}$ deduced from the overall energy balance carried out at the process level (Figure 1.3). In general, and without going into the details that can be found in several reference works (Kurz and Fisher 1989), growth undercooling is written as the sum of several contributions (energy diffusion is neglected here because very often in AM a columnar constrained growth is observed):

$$\Delta T_d^{\alpha l} = -m^{l\alpha} w_0 \left(\frac{(1-k^{\alpha l})\mathrm{Iv}(\mathrm{Pe}_w)}{1-(1-k^{\alpha l})\mathrm{Iv}(\mathrm{Pe}_w)} \right) + \frac{2\Gamma^{\alpha l}}{R_d} \qquad [1.4]$$

$$\Delta T_e^{\alpha\beta l} = A_w \, Pe_{\lambda_e} + A_R/\lambda_e \qquad [1.5]$$

The first contribution of equation [1.4] is the undercooling of chemical origin, $\Delta T_{d,w}^{\alpha,l} = -m^{l\alpha}\left(w_d^{l\alpha} - w_0\right)$, related to the diffusion of the solute in the liquid. It is estimated by the product of the slope of the liquidus of the phase diagram, $m^{l\alpha}$, and the gap between the composition far from the interface, w_0, and the composition of the liquid at the interface, $w_d^{\alpha l} = w_0 \left(1-(1-k^{\alpha l})\mathrm{Iv}(\mathrm{Pe}_w)\right)^{-1}$. The latter is given by the

Ivantsov solution Iv(Pe_w) of the steady diffusion profile of the solute in the liquid for a value of the Peclet number, $Pe_w = (R_d V_s)/(2 D^l)$, where R_d is the radius of the parabolic tip representative of the dendritic growth shape and D^l is the chemical diffusion coefficient of the solute in the liquid. The second contribution of equation [1.4] is that of the curvature at the tip of the dendrite, $\Delta T_{dR}^{\alpha l} = 2\Gamma^{\alpha l}/R_d$, the Gibbs Thomson coefficient. As for equation [1.5], it is also the sum of a chemical undercooling, $\Delta T_{ew}^{\alpha\beta l} = A_w\, Pe_{\lambda_e}$, and a curvature undercooling, $\Delta T_{eR}^{\alpha\beta l} = A_R/\lambda_e$, with $Pe_{\lambda_e} = (\lambda_e V_s)/D^l$ the Péclet number being associated with the eutectic interlamellar spacing $\lambda_e = (A_R/A_w)^{1/2}(D^l/V_s)^{1/2}$ and this expression justifying equation [1.3]. The coefficients A_R and A_w are defined by the properties of the phase diagram and physicochemical properties such as the Gibbs–Thomson coefficients between the solid and liquid phases, αl and βl (Kurz and Fisher 1989; Dantzig and Rappaz 2016).

However, if the growth rate is not too high, the solid–liquid interface can be considered to be at equilibrium, that is, its compositions can always be read on the equilibrium phase diagram in the presence of a curvature of the interface. The equilibrium diagram then remains the basic tool to work from. The diagram with curvature must be preferred to that without curvature because it always represents a thermodynamic equilibrium where the free energy of the solid phase accounts for its curvature. Note also that the curvature of the s/l interface certainly modifies the thermodynamic equilibrium, but independently of the speed of the interface.

1.1.3. *Loss of local interface equilibrium at high solidification rates*

The contributions above express the solute diffusion effects as well as those of the curvature of the interface. In doing so, they always assume that the solid and liquid at the interface are in thermodynamic equilibrium. When the solid is growing in the liquid at the solidification rate V_s, we have seen that the interface is the site of solute exchanges between the solid and liquid phases. To maintain a constant value of the partition coefficient, equal to that read on the phase diagram, the atoms will need time to be evacuated from the interface zone by diffusion in the liquid. It is this assumption that is made to develop the models given by equations [1.4] and [1.5]. The interface is then always at local thermodynamic equilibrium, despite the equilibrium deviations linked to the solute diffusion fluxes, as well as to the curvature. To achieve this, the diffusion length of the atoms in the liquid, D^l/V_s, must be much larger than the thickness of the interface, δ, where D^l represents the diffusion coefficient of the solute in the liquid. This condition can be written as:

$$Pe_\delta << 1 \text{ with } Pe_\delta = \delta V_s/D^l \qquad [1.6]$$

where Pe_δ represents the dimensionless Peclet number, the ratio of variables δ and D^l/V_s. In practice, for a rough (also called diffuse) interface representative of most metal alloys, δ is around a few atomic layers (10^{-9} m). The diffusion coefficient in the liquid is approximately 10^{-9} $m^2\,s^{-1}$, and the deviation from this interface thermodynamic equilibrium condition takes place for velocities close to 1 $m\,s^{-1}$. To translate the deviation from the thermodynamic equilibrium of the interface as a function of the solidification rate, Aziz (1982) introduced an effective partition coefficient, $k_v^{\alpha l}$, function of the Peclet number, Pe_δ:

$$k_v^{\alpha l} = \frac{k^{\alpha l} + Pe_\delta}{1 + Pe_\delta} \qquad [1.7]$$

So, when Pe_δ is low enough, the effective partition coefficient tends toward that of equilibrium $k^{\alpha l}$. On the other hand, for sufficiently high values of Pe_δ, $k_v^{\alpha l}$ tends toward 1, which reflects "solute trapping" or the absence of chemical redistribution at the interface. The solid–liquid interface is then no longer in thermodynamic equilibrium. By extension, it has also been proposed to modify the slope of the liquidus of the equilibrium phase diagram, $m^{l\alpha}$, to account for the speed of the interface (Boettinger and Coriell 1986):

$$m_v^{l\alpha} = m^{l\alpha}\left(1 + \frac{k^{\alpha l} - k_v^{\alpha l}(1 + \ln(k^{\alpha l}/k_v^{\alpha l}))}{1 - k^{\alpha l}}\right) \qquad [1.8]$$

The chemical undercooling is then given by $-m_v^{l\alpha}(w_d^{l\alpha} - w_0)$. Again, at low speed, $m_v^{l\alpha}$ tends toward $m^{l\alpha}$, the value at equilibrium. Although equations [1.7] and [1.8] propose a model of the evolution of the thermodynamic properties to describe the partition of the solute at the interface according to the solidification rate, they do not give the unique value toward which the chemical composition must tend for a sufficiently high speed. It is the analysis by Baker and Cahn (1971) that provides the necessary construction. The thermodynamic equilibrium condition given by the equality of chemical potentials, $\mu^l = \mu^\alpha$, is replaced by a condition given by the free enthalpy of the phases, $G^l = G^\alpha$. The first case corresponds to the common tangent of curves G^l and G^α at temperature T and pressure p of the mixture. It provides access to the equilibrium compositions of the phases, $w^{\alpha l}$ and $w^{l\alpha}$, and therefore at value $k^{\alpha l}$, thus constructing the phase diagram in Figure 1.4. The second case more simply looks for the composition at which the free enthalpies of the phases are equal at temperature T of the mixture, thus corresponding to the solute trapping condition. Conversely, one can investigate at what temperature an alloy of known composition can give rise to solidification without segregation between the solid and liquid phases. In a phase diagram, this temperature is sometimes referred to as the line T_0 (Kurz and Fisher 1989; Dantzig and Rappaz 2016). It is shown in the two-phase domain $\alpha + l$ in Figure 1.4.

Another phenomenon giving rise to a deviation from thermodynamic equilibrium is the attachment kinetics of atoms. This designates the capacity of the atoms of a liquid to reorganize to join a growing α solid phase. To quantify it, we introduce a kinetic undercooling, $\Delta T_{dc}^{\alpha l}$, inversely proportional to the velocity of the solid–liquid interface:

$$\Delta T_{dc}^{\alpha l} = V_s/\mu_k \qquad [1.9]$$

where $\mu_k = (\Delta S_f V_{son})/(R T_f)$ is the kinetic attachment coefficient with R the ideal gas constant, T_f is the melting point of the pure body, ΔS_f is the entropy of fusion and V_{son} is the speed of sound (around 1,000 m s^{-1}) (Turnbull 1962). For a metal with a rough interface, μ_k is around 10^3 m s^{-1} K^{-1}. Solid growth rates of the order of 1 m s^{-1} are required for attachment kinetic undercooling to play a role. In fact, at extreme speeds (100–1000 m s^{-1}), some systems also show that the atoms no longer have time to reorganize at the interface to form a crystal. The atoms of the liquid freeze and a glassy phase can be observed.

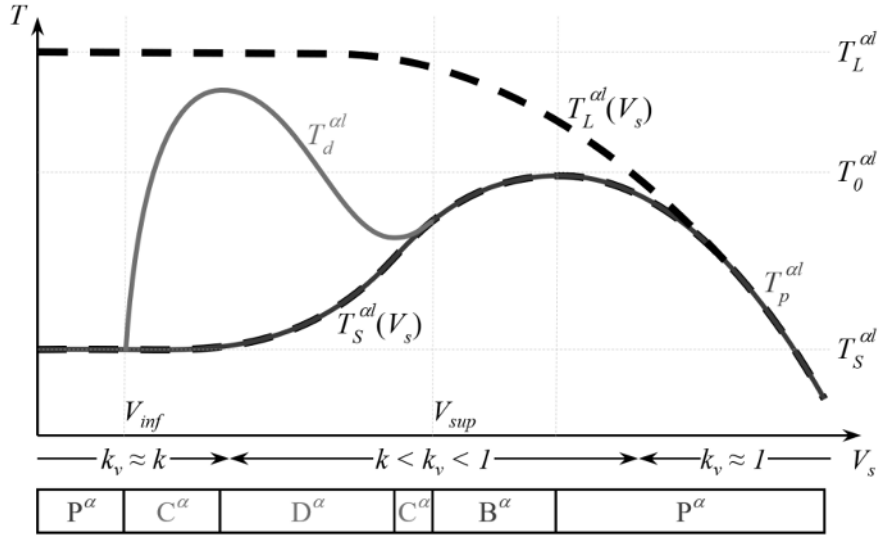

Figure 1.5. *Growth temperature of a solid–liquid interface as a function of its velocity V_s for a flat interface morphology, $T_p^{\alpha l}$ (in red), and a cellular or dendritic one, $T_d^{\alpha l}$ (in green). For a color version of this figure, see www.iste.co.uk/peyre/alloys2.zip*

COMMENTS ON FIGURE 1.5.– *The schematic representation is given here for an alloy of known composition, the solid at the interface consisting of a single phase and the growth being directional in a fixed temperature gradient (recomposed from*

Gremaud (1990)). The identified morphologies are planar (P), cellular (C), dendritic (D) and banded (B).

Figure 1.5 gives an illustration of the temperature of a dendritic structure, $T_d^{\alpha l}$, calculated using equations [1.4] and [1.7]–[1.9]. Note that the model covers both dendritic and cellular morphologies, that is, dendritic without secondary branches. As additional morphologies have been mentioned, flat front and banded, we now introduce them.

1.1.4. *Growth morphologies*

Speed limits exist that define the morphologies of microstructures. Mullins and Sekerka (1964) establish a stability analysis of a flat front αl. The expression for this limit is $V_{inf} = G\, D^l/\Delta T_0$, where $\Delta T_0 = T_L^{\alpha l} - T_S^{\alpha l}$ is the solidification interval of the alloy defined by the thermodynamic equilibrium temperature values at the start and end of solidification, considering only the two-phase equilibrium $\alpha + l$. This speed corresponds to the constitutional undercooling limit (Tiller et al. 1953) for which the flat front can only grow stationary at the solidus of the alloy, $T_S^{\alpha l}$, the temperature gradient at the interface, G, being higher than its chemical counterpart, $m^{l\alpha} G_w^{l\alpha}$, where $G_w^{l\alpha}$ represents the composition gradient of the solute in the liquid at the interface αl.

Considering the orders of magnitude typical for metal alloys and AM processes, $\Delta T_0 = 100$ K, $G = 10^5$ K m^{-1}, and $D^l = 10^{-9}$ m^2 s^{-1}, we obtain $V_{inf} = 10^{-6}$ m s^{-1}. Considering the velocity field represented in Figure 1.3, we do not expect to meet this condition of existence of the flat front in AM. Indeed, even if the speed at the bottom of the melt-pool starts from zero, it increases very rapidly to reach several millimeters per second only a few micrometers behind the heat source. This speed limit, V_{inf}, below which growth morphology is flat, P^{α}, is represented in Figure 1.5.

For a higher solidification rate, the morphology becomes cellular, C^{α}, then dendritic, D^{α}, the latter corresponding to the diagrams of Figures 1.1 and 1.4. For even higher speeds, the interface αl gradually re-stabilizes, reassuming a cellular morphology, C^{α}, then a flat front, P^{α}. This is the limit of absolute stability at high speed. Again, an analytic expression can be derived, $V_{sup} = (D^l\, \Delta T_0)/(k^{\alpha l}\, \Gamma^{\alpha l})$. It is interesting to note the absence of the temperature gradient in this expression, as well as the presence of the Gibbs–Thomson coefficient reflecting the effect of the interfacial energy. It is indeed this energy that stabilizes the interface perturbations at high solidification rates. By taking typical values of the properties previously introduced and adding $\Gamma^{\alpha l} = 2 \times 10^{-7}$ K m and $k^{\alpha l} = 0.5$, we obtain $V_{sup} = 1$ m s^{-1}.

Thus, in areas of beads where the liquidus isotherm is the fastest, it could be that this limit is reached. Moreover, this was the order of magnitude used in microstructure studies concerning laser remelting in the 1990s, giving rise to the observation of the transition C^{α} – P^{α} at high solidification rates (Kurz and Trivedi 1996). In Figure 1.5, it can also be noted that a growth regime in the form of a banded microstructure, B^{α}, is encountered close to the stability of the flat front V_{sup} (Kurz and Trivedi 1996). Its explanation requires that the effects of non-equilibrium growth of the interface be accounted for. Generally speaking, it is close to this speed V_{sup} that the effects of deviation from thermodynamic equilibrium are present in metallic alloys. Beyond a certain speed, the crystalline phase α can no longer form and the liquid is frozen in the form of a metallic glass. This can be observed for powder atomization and melt spinning processes and the speeds here are estimated to be around 100 m s^{-1} (Dantzig and Rappaz 2016).

The temperature of a flat front, $T_p^{\alpha l}$, can also be calculated as a function of the solidification rate. Since the steady-state growth of the flat front can only be achieved at the solidus of the alloy, $T_p^{\alpha l} = T_S^{\alpha l}$, its undercooling $\Delta T_p^{\alpha l}$ is the sum of the chemical contribution, $\Delta T_{pw}^{\alpha l} = m_v^{l\alpha}\left(w_p^{l\alpha} - w_0\right)$ where $w_p^{l\alpha} = w_0 / k_v^{\alpha l}$ is the composition of the liquid at the solidus temperature, plus the kinetic contribution given by equation [1.9].

For a rate less than V_{inf}, that is to say a low rate, $k_v^{\alpha l} = k^{\alpha l}$, $m_v^{\alpha l} = m^{\alpha l}$ and V_s/μ_k is negligible, so that $\Delta T_p^{\alpha l} = \Delta T_0$ corresponding to growth at the solidus temperature. By increasing the speed, the solidus is affected, $T_S^{\alpha l}\left(V_s\right)$, as shown in Figure 1.5. We note that the liquidus temperature is also affected and that it is only at very high rates that $T_L^{\alpha l}\left(V_s\right)$ and $T_S^{\alpha l}\left(V_s\right)$ are close to T_0, with $k_v^{\alpha l}$ tending toward 1. However, as illustrated in Figure 1.5, the kinetic undercooling contribution is already present before $T_L^{\alpha l} = T_S^{\alpha l} = T_0$ and the temperature of the flat front continues to decrease. Complete solute trapping only takes place for a solidification rate that has exceeded the absolute stability velocity, V_{sup}. The curves describing the cellular/dendritic and flat front structures in Figure 1.5 naturally meet at the stability limits of the flat front. The selected structure is the one with the highest growth temperature and therefore requires the lowest equilibrium deviation. The stability regimes of the structures expected as a function of the speed can then be listed in the ascending order: P^{α}, C^{α}, D^{α}, C^{α}, B^{α} and P^{α}.

Figure 1.6 gives a summary of the evolution of the structures observed for an alloy of eutectic composition Al–33 wt% Cu (Zimmermann 1990). Although the growth theories are different from those of dendritic microstructures, we find the

schematic description of the role velocity on the microstructures as the solidification of the pool occurs. We note in particular the decrease in the size of the interlamellar spacing with solidification front velocity predicted by equation [1.3] and the transition to a banded structure at high speed. In fact, chemical contributions, curvature and kinetics are also at the origin of these evolutions. It should be noted, however, that the structure described for the single-phase microstructure growing in the liquid close to the absolute stability limit is replaced by a coarser wavy eutectic structure.

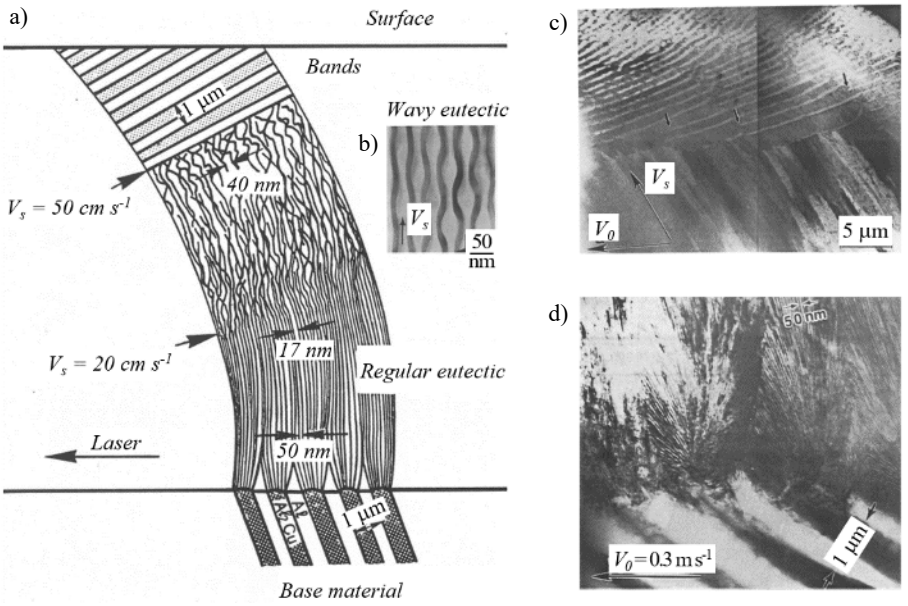

Figure 1.6. *Solidification structures of an alloy of eutectic composition Al–33 wt.% Cu observed in a longitudinal cross section XZ (according to Zimmermann 1990)*

COMMENTS ON FIGURE 1.6.– *See for reference Figure 1.3. Structures in the center of a laser trace showing a schematic representation of (a) the microstructural evolutions from the unmelted base material to the upper metal surface and (d) the regular and (b) wavy eutectic composition and the transition to a band structure (c) (according to Zimmermann 1990).*

1.1.5. *Growth competition between microstructures*

Figures 1.5 and 1.6 introduced and illustrated the principles of growth competition during the solidification of an alloy. They must be supplemented by the possible competition between different types of microstructures.

Thus, we see in Figure 1.4 that the diagram shows, for the same alloy of composition w_0, both a dendritic structure and a eutectic structure. The figure suggests that $T_d^{\alpha l} > T_e^{\alpha\beta l}$. This situation is a special case because it is also possible to find, for the same alloy composition, situations for which $T_d^{\alpha l} < T_e^{\alpha\beta l}$. This can happen by changing the rate of solidification. In this case, for the eutectic structure $\alpha + \beta$ developing at a temperature higher than that of the single-phase dendritic structure α, the latter will be prevented from growing. In Figure 1.4, this principle can be extended to competition with a βl structure, so that a total of three types of structures can compete. Depending on the growth conditions, the microstructure selected will not be the one with the highest equilibrium phase onset temperature, but rather the one with the highest growth temperature. It should be noted here that the same principle is applied in Figure 1.5 to establish which of the growth morphologies of an αl interface is selected.

Figure 1.7 schematizes the construction using the same phase diagram as in Figure 1.4 in a simplified way and for the composition alloy w_0. The growth temperatures of the microstructures resulting from the equilibria αl, βl and $\alpha\beta l$ are calculated as a function of the solidification rate and transferred to the right. The upper part of the figure indicates which of the microstructures are the most stable on the basis of the criterion of the maximum growth temperature. It is thus found that, at very low growth rates, it is a eutectic structure which is favored. This result is not intuitive but corresponds to the fact that the α structure with a flat front grows at a much lower temperature defined by the solidus of the mixture αl at composition w_0, below the eutectic growth temperature. This lower limit is of little interest for AM as mentioned above.

On the other hand, while the microstructure resulting from the single-phase interface αl is present in a wide range of rates in Figure 1.7, the eutectic microstructure, then a microstructure from the βl interface, become stable again at higher rates. For the alloy considered, it is then possible to plot on the phase diagram the domains of microstructure formation according to the rate of solidification. The procedure carried out over the entire composition range defines the coupled zone, that is, the region of the phase diagram where only the eutectic structure appears, but also the regions where the single-phase primary phases α and β are formed. It should be noted that the method described only applies to determining the structure growing at the highest temperature, called the primary solidification structure, without predicting

the secondary phases formed from the liquid state, such as the inter-dendritic eutectic structure illustrated in Figure 1.4. Figure 1.7 therefore identifies the regions of composition and rate allowing the formation of one type of primary microstructure. By extension the microstructure selection map is constructed, such as in the Al-Fe (Gilgien et al. 1995) and Al-Cu (Gill and Kurz 1995) systems, for wide rate and chemical composition ranges. Maps and studies of competition between microstructures also exist in more limited domains for Ni-Al (Hunziker and Kurz 1999; Tourret et al. 2011) and Fe-Ni (Hunziker et al. 1998; Vandyoussefi et al. 2000; Dobler et al. 2004), including in particular peritectic microstructures, as well as for some multi-component systems.

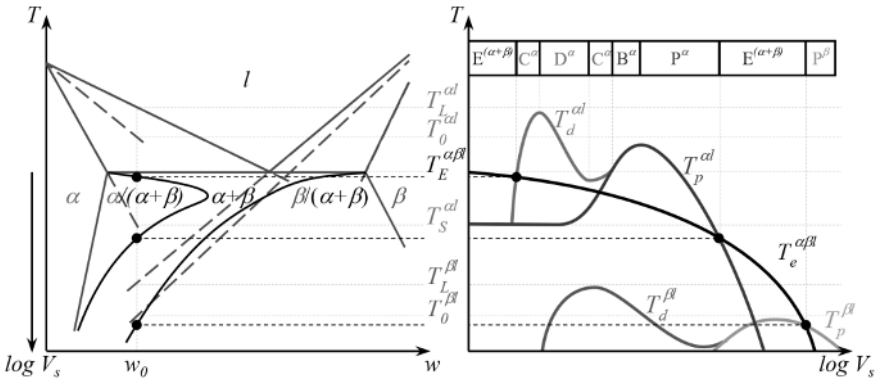

Figure 1.7. *Principle of the coupled zone in the case of a binary eutectic system. For a color version of this figure, see www.iste.co.uk/peyre/alloys2.zip*

COMMENTS ON FIGURE 1.7.– *For the alloy with composition w_0, the single-phase solidification microstructures α and β can form as well as the eutectic two-phase structure $\alpha + \beta$. On the right, the growth temperatures of these three structures are plotted against velocity using growth kinetics models (e.g. equations [1.4] and [1.5]). The structure adopting the highest growth temperature is assumed to be the most stable, defining domains of existence according to the growth rate (according to Kurz and Fisher (1989) and Dantzig and Rappaz (2016)).*

In the presentation given, the phase diagram used is that at equilibrium, with domain limits that can be modified by the kinetic contribution via equations [1.8] and [1.9]. However, many systems present equilibria with metastable phases that must also be considered to determine any possible competing microstructures. There are many examples in the literature. The best known is probably that of the Fe-C diagram. While the stable eutectic of the phase diagram is defined by gray cast iron, composed of lamellae of a solid solution of iron, austenite and graphite (composed

of pure C), it is common to observe the formation of white cast iron, a metastable eutectic material with the same austenitic phase but also with the Fe_3C intermetallic phase. The microstructure selection map must then focus on calculating the growth temperature of the metastable eutectic (austenite + Fe_3C), even though the intermetallic is not initially present in the equilibrium phase diagram. The stable and metastable phase diagrams must therefore be used to plot the growth temperature curves in Figure 1.7. The nucleation phase kinetics have not been considered here either. We confined ourselves to comparing growth temperatures, assuming that the phases are already present or can germinate as soon as their thermodynamic equilibrium temperature is reached. Otherwise, nucleation must be added to the mechanisms governing the competition between microstructures. Finally, it should also be mentioned that the theories concerning growth competition between microstructures are mainly developed for binary model alloys. Extensions are necessary for application to industrial alloys.

1.1.6. *Selection of grain structures*

So far, we have considered the microstructure. The primary grain structure, or primary solidification macrostructure, is defined on a larger scale. It results from the growth of the primary microstructure, which can be dendritic or eutectic according to the principle of selection seen in section 1.1.5. The grain is generally defined as the domain grouping together the microstructure resulting from the same germ. When the microstructure growth is done by successive branches of the crystal, a relative uniformity of the crystallographic orientation of the microstructure within the same grain can exist. Similarly, in AM where remelting and solidification alternate to build the part layer after layer, the crystallographic orientation can be propagated in the direction of the temperature gradient. The grain structures can then reach very large dimensions, close to those of the manufactured part in the direction of manufacture (i.e. the temperature gradient). Figure 1.1 shows the growth of dendritic grains developing in a liquid subjected to a temperature gradient G, cooling evenly at the rate $G \cdot V_L$ with V_L the velocity of the liquidus isotherm. Three grains, numbered 1 to 3, are each composed of two dendrites of the same color. For these grains, the color corresponds to a crystallographic orientation, here defined by a simple rotation θ with respect to the direction of the temperature gradient. The directions of the trunks and arms of dendrites of the same grain are therefore identical, generally oriented in the <100> crystallographic direction in the case of materials with a cubic dendritic microstructure. Figure 1.1 also shows the distances between the liquidus isotherm of the alloy and the tip of the columnar dendrites. In steady-state growth, the velocity $V_{s,0}$ of dendrites in grain 1, with orientation $\theta = 0°$, is equal to the isotherm velocity, V_L. The dendrites are located on isotherm $\Delta T_{\theta=0°}$, at a distance

$\Delta z_{\theta=0°} = \Delta T_{\theta=0°}/G$ of the liquidus isotherm of the alloy. In the case of a grain with orientation $\theta \neq 0°$, such as grain 2 at the center of figure, so that stationary growth is established, allowing the solidification front to follow the displacement of the isotherms at the rate V_L, and the distance to travel in direction <100> is greater than for $\theta = 0°$. The speed in direction <100> is therefore greater, that is, $V_{s,\theta\neq 0°} = V_L/\cos\theta$. As seen previously for a dendritic microstructure, greater undercooling corresponds to a higher rate, $\Delta T_{\theta\neq 0°} > \Delta T_{\theta=0°}$, and therefore a greater distance $\Delta z_{\theta\neq 0°} = \Delta T_{\theta\neq 0°}/G > \Delta z_{\theta=0°}$. As a result, the tips of the grain 2 dendrites are geometrically blocked in their progression by the dendrite arms of grain 1. Blocking phenomena occur at the interfaces between the grains, in particular between grains 2 and 3. However, the consequence of these competitions leads to the progressive elimination of the grains disoriented with respect to the temperature gradient (high θ values), thus creating a crystallographic texture <100> aligned with the temperature gradient (low θ values).

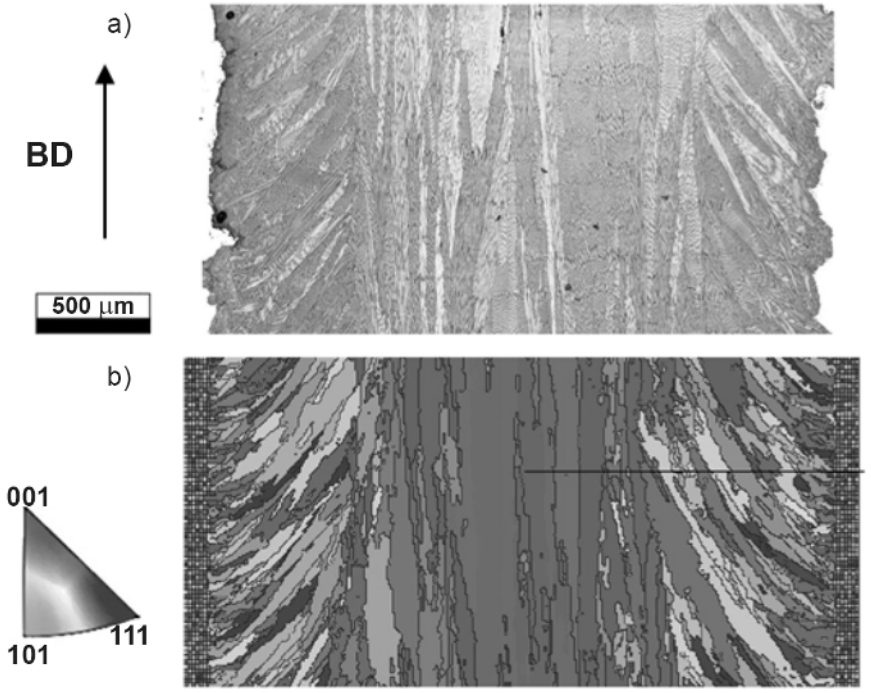

Figure 1.8. *Section of a sample produced by E-PBF from a CMSX-4 nickel base superalloy powder revealing (a) the columnar grain structure (metallography) and (b) the associated strong texture (simulation), the direction of projection of the crystallographic orientations being vertical, corresponding to the direction of construction. For a color version of this figure, see www.iste.co.uk/peyre/alloys2.zip*

COMMENTS ON FIGURE 1.8.– *Power and speed of the electron beam, P_0 = 300 W and V_0 = 0.5 m s^{-1}, preheat temperature, T_i = 900°C, thickness of successive deposits, 50 μm (according to Koepf et al. 2019).*

Figure 1.8 provides an example of a columnar grain structure obtained by E-PBF for a nickel-based superalloy (Koepf et al. 2019) and its modeling using the cellular automata method (Gandin and Rappaz 1997; Carozzani et al. 2013). Particular attention to the metallographic cross-section makes it possible to distinguish about 10 layers built from bottom to top. It is the manufacture method implemented and the parameters of the process which allow the growth of columnar grains by epitaxy. The simulation combines a three-dimensional description of the thermal process (e.g. Figure 1.3) with a spatial description in the form of cells whose state (liquid or belonging to the microstructure) and crystallographic orientation evolve over time. To do this, the kinetics of the primary solidification microstructure (i.e. dendritic here) are integrated over time, proportionally to the undercooling defined by the temperature field and equation [1.4]. It should be noted that, despite the velocity of the heat source used, no effects due to modification of the thermodynamic equilibrium are accounted for (equations [1.7] and [1.8]). Similarly, the dendritic growth kinetics are not coupled with the calculation of the multicomponent phase diagram and its properties. Finally, the coupling between the temperature fields and the development of the microstructure is weak, that is, temperature is only used to calculate the grain structure without the structure itself influencing the temperature fields. The comparison is nevertheless remarkable, and the method can also give rise to comparisons with pole figures or maps characterizing the crystallographic orientation relationships between grains (Chen et al. 2016; Pineau et al. 2020).

The columnar growth competition explained above assumes that no new grain appears in the liquid. The origin of such columnar grains can be from nucleation in the undercooled liquid, at the undercooling ΔT_N, as shown in Figure 1.1, at a distance $\Delta z_N = \Delta T_N/G$. The equiaxed structure can then grow and end up blocking the growth of columnar grains, causing the CET. It should be noted that the origin of the equiaxed grains can also be the fragmentation or partial refusion of the existing dendritic microstructure and transport by convection of the fragments in front of the columnar growth front. The directions of the arms of the equiaxed grains are random. The simplest CET criterion is based on the integration of the growth kinetics of the envelopes of the equiaxed grains, with velocity $V_s(\Delta T)$, assuming a constant cooling rate, $G \cdot V_L$. The grains, although growing, are immobile, so that their undercooling ΔT only increases during cooling. By doing so, their size may be sufficient to mechanically halt the growth of columnar grains (Hunt 1984). Integration between nucleation positions Δz_N and the columnar front easily shows that the CET is a function of the ratio G/V_s and nucleation undercooling, ΔT_N, but also the growth

kinetics of the dendrites and the density of the equiaxed grains. Other CET criteria exist to account for fragmentation (Gandin 2000), solutal interaction between columnar and equiaxed dendrites (Martorano et al. 2003) and transport of equiaxed grains in the liquid (Leriche et al. 2015).

1.1.7. *Solidification in additive manufacturing*

The previous sections provide an overview of the phenomena occurring during the formation of solidification microstructures in AM processes. We can emphasize several points:

– first, the dendritic and eutectic microstructures can be described by the temperature field by considering the velocity of the liquidus isotherm of the alloy and the temperature gradient in the liquid on this same isotherm;

– theories for the kinetics of the formation of solidification microstructures date back to the 1980s and 1990s. They concern the morphologies of the solid–liquid interfaces resulting from the growth of a single-phase or two-phase solid, mainly for binary metal alloys and single remelting passes of the material;

– effects at high solidification rates are pertinent for metallic alloys only when the solidification speed approaches 1 m s^{-1}. This speed is encountered in the upper part of the melt-pool. Given the multilayer nature of the deposits made in AM, leading to a systematic remelting of the previously deposited layers, it is not easy to know if these conditions can be encountered on the microstructures finally formed, unless one is only interested in the last solidified layers. Further microstructural analysis of the beads is required. This would require conditions allowing the formation of microstructures typical of rapid solidification, for one and several layers, and associated simulations;

– the coupling of theories with a complete description of thermodynamic equilibria remains to be systematized, although it has begun (Gilgien 1996; Senninger et al. 2018). This is necessary to allow more direct application to multi-component alloys;

– simulating the grain structures results from the calculation of the microstructure kinetics. Therefore, work on grain structures directly depends on work done on microstructures. The advantage of grain structure modeling is to provide the crystallographic orientation field and the grain size, information not available from a simple theoretical analysis of the kinetics of the formation of microstructures.

1.1.8. *Acknowledgments*

The author expresses his thanks to Théophile Camus, Gildas Guillemot and Oriane Senninger for their contributions to this section.

1.2. Microstructures of steels

1.2.1. *Steels and additive manufacturing*

Known and used for millennia, steels are Fe-C alloys containing less than 2.1% by mass of carbon. Other chemical elements, called alloying elements, are usually added to improve the material properties (mechanical properties, corrosion resistance, etc.). Currently, the industrial use of steels produced by AM mainly concerns austenitic stainless steels, maraging steels, precipitation hardening stainless steels and tool steels for heat resistance. The chemical compositions of four grades representative of these classes of steels are presented in Table 1.1.

Historically, austenitic stainless steels 304L and 316L were the first steels to have been studied in AM due to their widespread industrial use arising from their excellent resistance against corrosion. The attention of the industry soon focused on another class of steels: maraging steels (for martensite aging). These steels exhibit a very low carbon content and owe their excellent hardness to the precipitation of Ni_3X intermetallics in a martensitic matrix. Mainly used by the aerospace and tooling industries, maraging steels are preferred to produce geometrically complex parts in relatively small quantities and are thus ideally suited to AM. However, when corrosion resistance is required, 15-5PH and 17-4PH precipitation hardening stainless steels are preferred. The good mechanical strength of these steels is based on the precipitation of the Cu-rich ε phase in a martensitic matrix, while their high chromium content gives them excellent corrosion resistance. These three classes of steels are characterized by a very low carbon content: in fact, steels best suited to AM are characterized by their good weldability, that is, by a low carbon content making it possible to avoid cold cracking phenomena. However, for several years, steels known to be difficult to weld, such as H11 and H13 hot-work tool steels with a very high carbon content (greater than 0.3% by mass), have been produced by AM. These steels are used in particular for making inserts for plastic and especially metal injection molds due to their very high hardness and excellent resistance to thermal shock. For these industries, the freedom of geometry offered by AM makes it possible to design complex inserts with internal cooling channels that are impossible to machine.

Section 1.2 written by Sylvain DÉPINOY and Christophe COLIN.

Today, these four classes of steels can be produced in AM to build parts that are more than 99% dense with a minimal fraction of defects. On the other hand, due to extremely fast solidification and cooling rates, their final microstructures are significantly different from those obtained by more conventional continuous casting or casting processes.

	316L (austenitic stainless steel)	18Ni-300 (maraging steel)	17-4PH (hardened stainless steel)	H13 (tool steel)
C	<0.03	<0.03	<0.07	0.32–0.45
Cr	16–18	<0.5	15–17	4.75–5.5
Ni	10–14	17–19	3–5	–
Mo	2.0–2.5	4.5–5.2	≤0.5	1.1–1.75
Mn	<2	<0.1	≤1	0.2–0.6
Si	<0.75	<0.1	≤1	0.8–1.2
Other elements	–	0.6–0.8 Ti 0.05–0.15 Al 8.5–9.5 Co <0.5 Cu	3–5 Cu 0.15–0.45 Nb	0.8–1.2 V

Table 1.1. *Chemical compositions in mass percentage of four grades representative of the four classes of steels most used in additive manufacturing*

1.2.2. *Rapid solidification of steels in AM*

1.2.2.1. *Types of solidification*

As explained in section 1.1, the type of solidification depends on the thermal gradient G at any point of the melting isotherm behind the melt-pool and on the solidification rate V_s, and more precisely on the ratio G/V_s. With the L-PBF process inducing a higher G/V_s ratio than in the DED process, steels produced by L-PBF are of the columnar cellular type and steels produced by DED are mainly of the columnar dendritic type. For simplicity, the term "cells" will be used in this section to describe both cells and columnar solidifying dendrites. As the deposition of a new layer leads to the partial or total refusion of one or more already consolidated layers, new cells grow epitaxially on the already solidified cells. This results in a microstructure organized in

large columnar grains oriented in the building direction and crossing several tens of layers. Each grain consists of several hundred solidification cells forming an intragranular substructure. Process parameters, through their effect on the cooling rate $\dot{T}$ represented by the product $G \times V_s$, have a direct effect on the size of the solidification cells. Thus, a steel produced by L-PBF will present a finer substructure compared to the same steel produced by DED.

1.2.2.2. *Microstructural characteristics*

1.2.2.2.1. Segregation phenomena during solidification

Some alloying elements have a lower solubility in the solid phase than in the liquid phase and will then be rejected by the solid cells into the intercellular liquid during solidification. There is therefore a variation in chemical composition between the core of the cells, which solidifies first, and the intercellular spaces, which solidify last. The tendency of solutes to segregate depends on the temperature, composition and crystal structure of the solidified phase (section 1.2.3.2). It can be estimated using the equilibrium partition coefficient $K_e = C_s/C_l$, where C_s and C_l are, respectively, the equilibrium concentrations of a given solute at the temperature T of the solid/liquid interface in the solid and liquid phases. A K_e value of less than 1 indicates a tendency to segregation, all the more so when this coefficient is low. However, as its name suggests, the K_e coefficient corresponds to a state of equilibrium, and therefore to an infinitely slow solidification of matter. In fact, the rate of solidification has a strong impact on chemical segregation, since the diffusion process of the solute at the solid–liquid interface is in competition with the displacement of this interface. The dependency of the partition coefficient K on an alloying element i at the solidification rate V_s is written as follows, according to the so-called "solute trapping" model:

$$K(V_s) = \frac{K_e + \delta_i \,.\, V_s/D_i}{1 + \delta_i \,.\, V_s/D_i} \qquad [1.10]$$

where δ_i and D_i are the atomic jump distance and the diffusion coefficient of solute i at the solid–liquid interface, respectively. According to equation [1.10], a zero-solidification rate yields the equilibrium partition coefficient K_e, while an infinitely fast rate leads to a partition coefficient $K = 1$, that is, the absence of chemical segregation (planar solidification). Thus, the type of AM process has an effect on the intensity of local chemical heterogeneities in the as-built material.

1.2.2.2.2. Presence of dislocations

A high dislocation density is observed in the materials produced by AM. These dislocations can be organized in different ways depending on the type of process

used: in L-PBF, a network of dislocations superimposed on the solidification substructure is commonly observed, in such a way that the dislocations are localized to the intercellular boundaries.

The origin of these dislocations has still not yet been fully elucidated. One theory postulates that the high dislocations density is due to the competition between two phenomena governing the direction of cell solidification (Andreau et al. 2019). On the one hand, cell growth is thermodynamically favored in the direction of the highest thermal gradient, that is, from the periphery of the melt-pool (colder) toward the point of impact of the beam (hotter). On the other hand, the melt-pool generally has a depth comprising several layers already deposited. This leads to the growth of new cells by epitaxy on the old ones already solidified at the outer periphery of the melt-pool. These two phenomena do not necessarily promote the same direction of growth, and each cell therefore grows in a direction close to but different from its neighbors. Since the interfaces between these cells are represented by geometrically necessary dislocations and the substructure is composed of a large number of cells, the material therefore has a high dislocation density.

Another theory considers that dislocations result from the plastic deformation of the material during the heating–cooling cycles, induced by the deposition of new layers (Figure 1.9). The observation of dislocation networks not superimposed on the cellular substructure, as well as the absence of disorientations between neighboring cells, tend to validate this second theory (Bertsch et al 2020; Dépinoy et al. 2021).

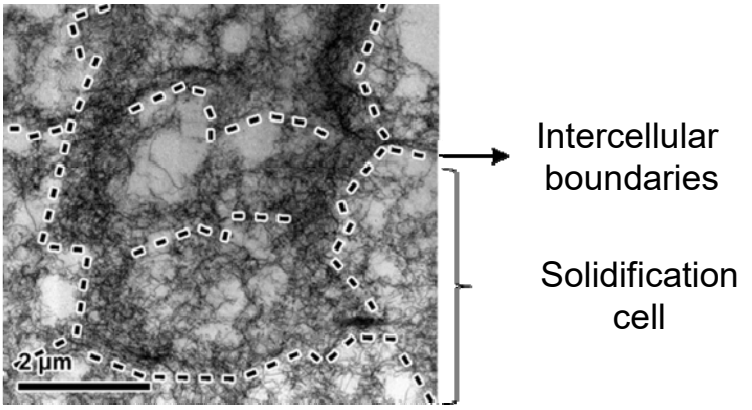

Figure 1.9. *Substructure in 316L steel produced by DED showing localized dislocations in the intercellular boundaries (highlighted in dotted lines) and fewer dislocations inside the solidification cells (Bertsch et al. 2020)*

1.2.3. *Phases and phase transformations*

1.2.3.1. *Equilibrium phases in steels and effect of chemical composition*

Depending on temperature and carbon content, different matrix phases can exist at thermodynamic equilibrium in Fe-C alloys (Figure 1.10). The ferrite, with a centered cubic lattice, is denoted δ (at high temperature, between T_1 and T_2) or α (at low temperature, lower than T_5). Austenite γ, with a face-centered cubic lattice, is stable between temperatures T_3 and T_4. There are two ferrite + austenite biphasic domains between T_2 and T_3 (δ + γ) and between T_4 and T_5 (α + γ). Due to their importance in the field of heat treatment (HT), temperatures T_4 and T_5 are known as Ac_3 and Ac_1, respectively.

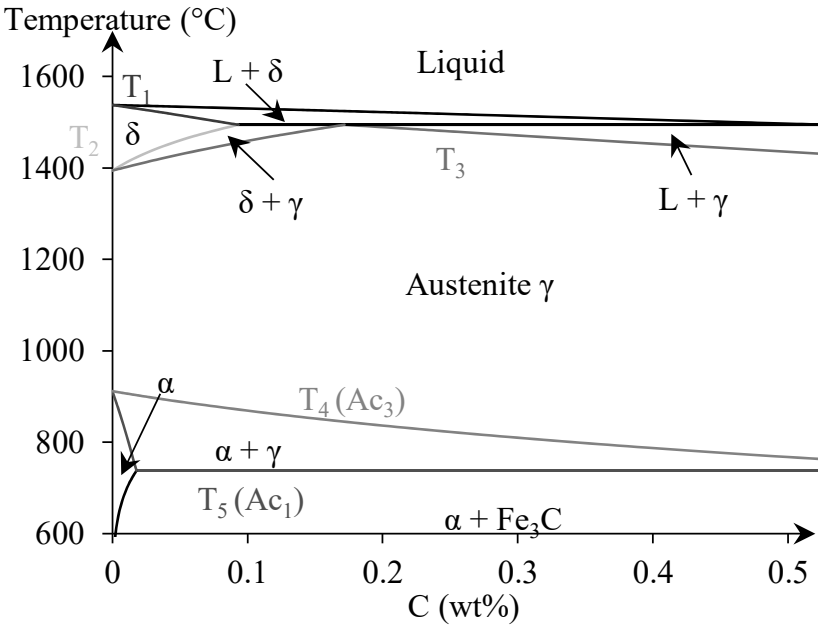

Figure 1.10. *Equilibrium phase diagram of the Fe-C system for carbon contents below 0.5% by mass. For a color version of this figure, see www.iste.co.uk/peyre/alloys2.zip*

The alloying elements added to steels can be divided into two main categories: those favoring the existence of ferrite (α or δ), so-called α-stabilizer elements; and those stabilizing austenite γ, known as γ-stabilizer elements. Chromium

(Figure 1.11a), molybdenum, silicon and even titanium are α-stabilizer elements, whereas nickel (Figure 1.11b), manganese, carbon (Figure 1.10) and nitrogen are γ-stabilizer elements. These elements are mostly purposely added into the material (alloying elements) but can also come from environmental contamination. Thus, the atomization of powders or the manufacture of parts by L-PBF under an N_2 atmosphere can lead to nitrogen contamination of the finished product.

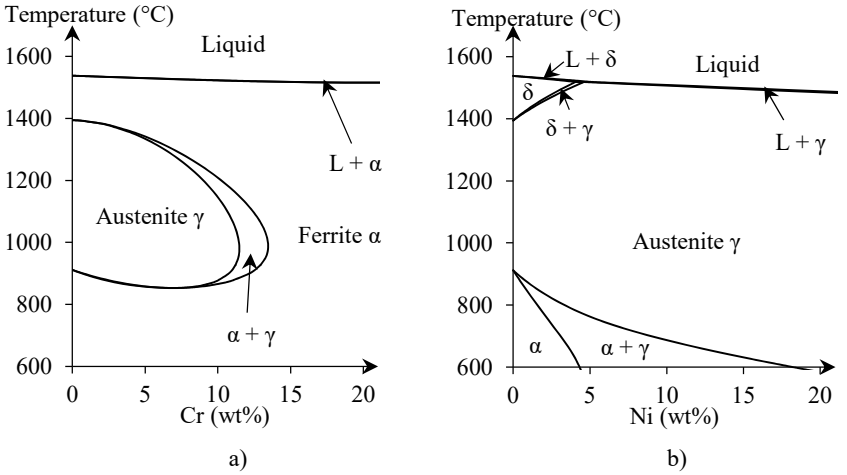

Figure 1.11. *Partial phase diagrams of the systems (a) Fe-Cr and (b) Fe-Ni*

Initially developed for welding studies, the "chromium equivalent" Cr_{eq} and "nickel equivalent" Ni_{eq} indicators make it possible to quantify the α-stabilizer or γ-stabilizer character of a steel according to its chemical composition (mass percentage). There are many equations in the literature, all empirical, to calculate these indicators. An example is given in equations [1.11] and [1.12] (Pickering 1978). Table 1.2 represents the domains of Cr_{eq} and Ni_{eq} for steels presented in Table 1.1, as well as their Cr_{eq}/Ni_{eq} ratios:

$$Cr_{eq} = \%Cr + 2\%Si + 1.5\%Mo + 5\%V + 5.5\%Al + 1.75\%Nb + 1.5\%Ti + 0.75\%W \quad [1.11]$$

$$Ni_{eq} = \%Ni + \%Co + 0.5\%Mn + 0.3\%Cu + 30\%C + 25\%N \quad [1.12]$$

	Cr_{eq}	Ni_{eq}	Cr_{eq}/Ni_{eq}
316L (austenitic stainless steel)	20–23	12–16	1.3–2
18Ni-300 (maraging steel)	8–11	26–29	0.3–0.4
17-4PH (hardened stainless steel)	17–20	6–8	2–3
H13 (tool steel)	12–16	10–14	0.9–1.7

Table 1.2. *Values of chromium-equivalent and nickel-equivalent indicators as mass percentages for the steels presented in Table 1.1*

Finally, the diffusion coefficient D and the equilibrium partition coefficient K_e of a given alloying element at a given temperature are not the same in austenite and in ferrite due to the different crystal structures of these phases.

As mean of illustration, values of K_e for a binary Fe-X system and D at 1,500°C for different alloying elements in ferrite and austenite are presented in Table 1.3.

X	C	Cr	Mn	Mo	Ni	N	Ti
			K_e				
Ferrite δ	0.13	0.95	0.84	0.80	0.80	0.28	0.14
Austenite γ	0.36	0.85	0.95	0.60	0.95	0.54	0.07
			D (10^7 cm²/s)				
Ferrite δ	1 600	3.4	1.2	–	1.6	420	–
Austenite γ	100	0.3	1.8	–	0.01	100	–

Table 1.3. *Values of the coefficient K_e in a binary Fe-X system (Ghosh 2001) and of the diffusion coefficient D at 1,500°C (Gale and Totemeier 2004) of different chemical elements in δ ferrite and γ austenite of pure iron*

1.2.3.2. *Liquid–solid transformations*

The liquid–solid transition can result in the primary solidification of δ ferrite or γ austenite (Figure 1.10). The existence of one or the other phase depends on the chemical composition (via the ratio Cr_{eq}/Ni_{eq}) and on the solidification rate.

A low Cr_{eq}/Ni_{eq} ratio (typically less than 1.3) induces fully austenitic solidification (L → γ), whereas a higher Cr_{eq}/Ni_{eq} ratio (greater than 2) results in fully ferritic solidification (L → δ) (Elmer et al. 1989). For intermediate Cr_{eq}/Ni_{eq} ratios there is a two-phase austenite-ferrite domain, or conversely ferrite-austenite, resulting from chemical segregation during solidification. In the austenite-ferrite

case, the cells will be austenitic in nature and will reject the α-stabilizer elements in the intercellular liquid, which will therefore solidify into ferrite (L → L + γ → γ + δ) (Figure 1.12). On the other hand, in the ferrite-austenite case, the cells will be made up of ferrite and the intercellular spaces of austenite (L → L + δ → δ + γ).

The solidification conditions, and in particular the solidification rate V_s, influence the nature of the solidified phases (Figure 1.13) due to their effect on the partition coefficient K of a given element (equation [1.10]). Indeed, to return to the example in Figure 1.12, a fast enough solidification rate can inhibit the segregation of α-stabilizer elements from the austenitic cells to the intercellular fluid. The resulting microstructure will then be entirely austenitic, although chemical composition gradients may still exist. As an indication, the changes in the K coefficients at 1,500°C of various alloying elements as a function of V_s in ferrite and in austenite, determined using the values reported in Table 1.3, are shown in Figure 1.14. The diffusion coefficient at the solid–liquid interface is here taken as the diffusion coefficient in the solid phase, and the atom jump distance δ_i is taken as the lattice parameter of ferrite and austenite at room temperature. While the C and N elements, having very high diffusion coefficients, are only slightly affected by the solidification rate, this is not the case for the Cr, Mn and Ni elements. It therefore appears that the same steel produced by L-PBF or by DED will not contain the same local chemical heterogeneities or even the same solidification phases.

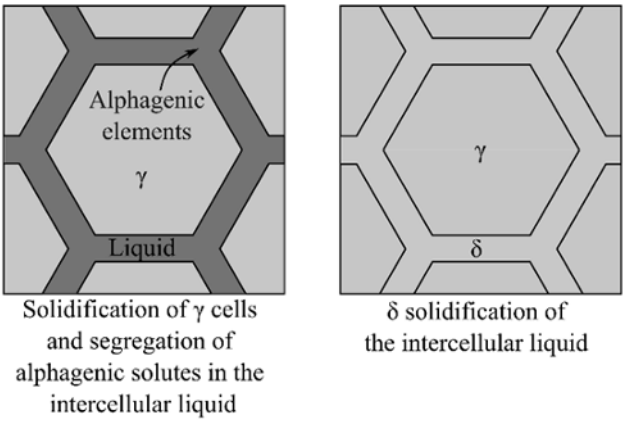

Figure 1.12. *Mechanisms leading to austenite-ferrite solidification microstructure. For a color version of this figure, see www.iste.co.uk/peyre/alloys2.zip*

As indicated by the values reported in Table 1.2, 17-4PH stainless steels solidify in a predominantly ferritic manner and 18Ni-300 maraging or H13 tool steels in a

predominantly austenitic manner. 316L stainless steels are in between and can solidify in a predominantly ferritic or austenitic manner depending on their composition and solidification rates, and therefore on the parameters and type of process. In fact, 316L has a fully austenitic solidification microstructure in L-PBF and an austenitic-ferritic one in DED.

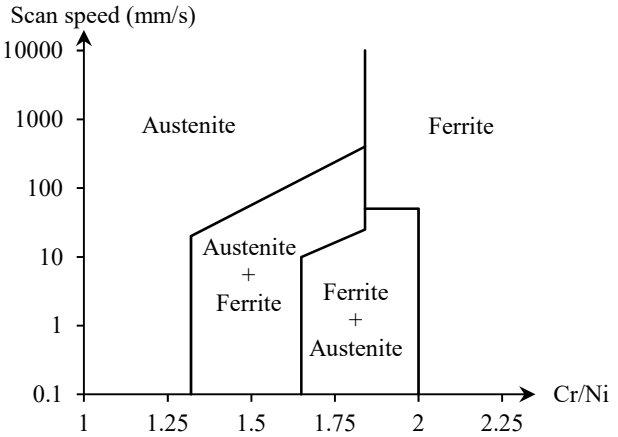

Figure 1.13. *Effect of the Cr/Ni ratio and the scan rate related to the solidification rate on the nature of the solidification phases for Fe-Cr-Ni model alloys (Elmer et al. 1989)*

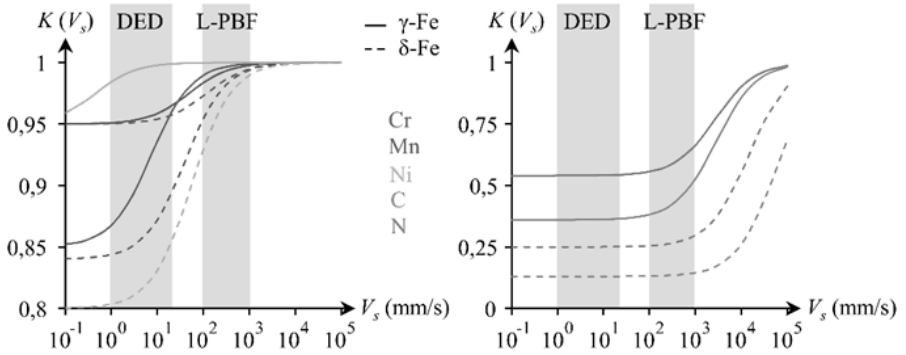

Figure 1.14. *Evolution of the partition coefficient K of different alloying elements at 1,500°C in δ ferrite and γ austenite as a function of the solidification rate V_s, determined using equation [1.10] and Table 1.3. The shaded areas indicate the order of magnitude of V_s, induced by the DED and L-PBF processes. For a color version of this figure, see www.iste.co.uk/peyre/alloys2.zip*

1.2.3.3. *Solid–solid transformations*

In most steels, the two phases resulting from the solid–liquid transformation are likely to transform during further cooling in the solid state and during the entire thermal cycle induced by the AM process. δ ferrite can be transformed at temperatures below T_2 into γ austenite, itself stable only above the temperature Ac_1 (Figure 1.10). Austenitic steels are an exception in that austenite is stable at room temperature due to its high nickel content (Figure 1.11(b)).

1.2.3.3.1. δ → γ transformation

The δ → γ transformation occurs below the temperature T_2 after total solidification of the material (Figure 1.10). Since the ferrite is once again stable below the temperature Ac_1, very fast cooling between temperatures T_2 and Ac_1 can prevent this transformation from taking place. Thus, the choice of the parameters and the type of process, through their effect on the cooling rate $\dot{T}$, could lead to a complete or partial inhibition of the δ → γ transformation. Furthermore, the chemical composition of the δ ferrite, which depends on the base powder but also on possible segregation phenomena during solidification, has a strong influence. Indeed, δ ferrite that is richer in α-stabilizer elements (high Cr_{eq}/Ni_{eq} ratio) implies a narrower temperature interval between the beginning and the end of the δ → γ transformation (Figure 1.11(a)), which is therefore more likely to be inhibited (Vunnam et al. 2019). For high enough Cr_{eq}/Ni_{eq} ratios, ferrite is thermodynamically stable (α + γ domain) and therefore the δ → γ transformation can only be incomplete regardless of the cooling rate.

After deposition, a layer containing δ ferrite can again reach, and this on several occasions, the temperature range of the δ → γ transformation during the heating–cooling thermal cycles linked to the deposition of new layers. However, the cooling rates involved are still too fast to allow complete destabilization of the ferrite, which will then be present in the final microstructure. It is thus possible to obtain a microstructure containing δ ferrite in 17-4PH steels, as in Alnajjar et al. (2019). In these cases, a thermal post-treatment at a temperature above Ac_3 is necessary to transform the ferrite into austenite.

1.2.3.3.2. Decomposition of austenite

γ-austenite, whether it arises from solidification or from the δ → γ transformation, can transform into many different phases depending on the cooling rate. With the exception of austenitic steels and under conditions of thermodynamic equilibrium, austenite transforms into α ferrite below the Ac_3 temperature (Figure 1.10). Due to their different crystal lattices, these two phases (γ and α) cannot accommodate the same amount of carbon: face-centered cubic austenite can contain up to 2% by mass against 0.02% in centered-cubic ferrite. The transformation of

austenite into ferrite is therefore accompanied by the diffusion of carbon out of the austenitic lattice and its precipitation in the form of carbides. In the case of the AM process, the cooling is too rapid to allow this diffusion. The ferrite then becomes supersaturated with carbon, inducing a distortion of its crystalline structure which gives rise to a new phase: the martensite α' with centered tetragonal crystal structure. Compared to ferrite and austenite, martensite is very hard, but also very brittle. The martensitic transformation is characterized by two temperatures, which are independent of the cooling rate: the M_s temperature, at which the transformation starts, and the M_f temperature, corresponding to the end of the transformation. The M_s temperature can be estimated using empirical equations depending on the mass chemical composition of austenite, the best known of which is Andrews' formula (equation [1.13]) (Andrews 1965):

$$M_s(°C) = 539 - 423\%\mathrm{C} - 30.4\%\mathrm{Mn} - 17.7\%\mathrm{Ni} - 12.1\%\mathrm{Cr} - 7.5\%\mathrm{Mo} \qquad [1.13]$$

When the M_s temperature is lower than the room temperature, the martensitic transformation does not take place and the austenite is therefore stable at room temperature. As an indication, the M_s temperatures of the four steels presented in Table 1.1 are between 80°C and –20°C for 316L, 180°C and 140°C for 18Ni-300, 240°C and 180°C for 17-4PH and 330 and 250°C for H13. The low M_s temperatures for 316L steel reflect the stability of its austenitic structure at room temperature. Although not mentioned in equation [1.13], nitrogen tends to decrease the M_s temperature and thus stabilize the austenite.

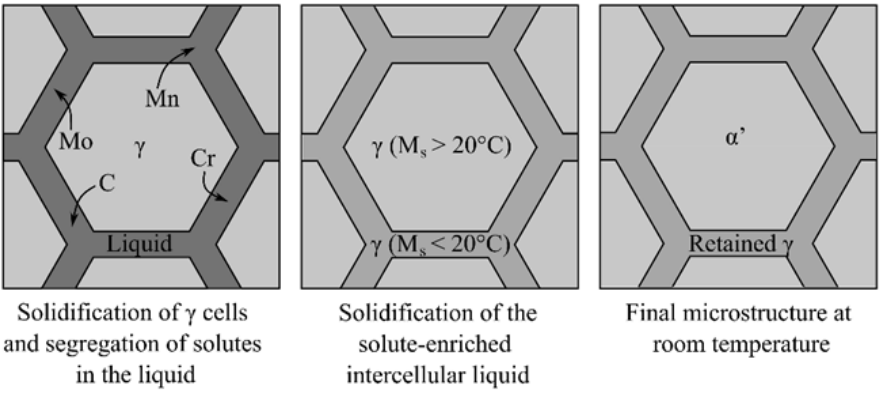

Figure 1.15. *Schematic representation of the process leading to an austeno-martensitic microstructure from austenitic solidification. For a color version of this figure, see www.iste.co.uk/peyre/alloys2.zip*

Due to the chemical heterogeneities arising from solidification (section 1.2.2.2), it is possible to obtain microstructures at room temperature where the cell core is martensitic and the intercellular spaces austenitic (Figure 1.15). This is the case, for example, in H13 tool steels (Deirmina et al. 2019), in 18Ni-300 maraging steels (Jägle et al. 2016) and in 17-4PH stainless steels (Rafi et al. 2014). In addition, the succession of thermal cycles linked to the deposition of new layers, or the preheating of the build plate can act as an HT on the martensite formed in the first layers. This in situ HT can lead to the precipitation of carbides (tempered or softened martensite). In such cases, a heterogeneous microstructure is obtained, where the base of the formed part consists of tempered martensite, and the last deposited layer consists of fresh martensite. This microstructural gradient leads to a gradient in mechanical properties, and more particularly a gradient in hardness in the part.

1.2.4. *Cold cracking*

The phase transformations arising during manufacturing can lead to cracking and failure of the built part, either at the end of solidification (hot cracking) or during cooling in the solid state (cold cracking). In AM, hot cracking mainly concerns 316L stainless steels and has long since ceased to be a technological challenge. On the other hand, cold cracking remains a hot topic, and an obstacle to the development of industrially interesting steels in AM. This type of cracking is produced by the combination of two factors: the presence of hard and brittle martensite in the material and the existence of strong gradients of mechanical stresses, here induced by the thermal cycle of the process. Some alloying elements, particularly carbon, increase the hardness and therefore the brittleness of martensite. The weldability of a steel, that is, its sensitivity to cold cracking, can thus be estimated from its chemical composition through the carbon equivalent criterion C_{eq}, first introduced in welding studies (equation [1.14]). Cold cracking is likely to happen for steels exhibiting a carbon content greater than 0.1% by mass and a carbon equivalent greater than 0.4% by mass. The risk of cracking further increases with the thermal gradients and therefore the residual stresses: as such, the L-PBF process is particularly likely to induce cold cracking. Conversely, this risk can be limited by reducing these thermal gradients, whether by preheating the build plate, using a preheating laser or optimizing the lasing strategy in order to better distribute the temperature over one layer or from one layer to another:

$$C_{eq} = \%C + \frac{\%Mn}{6} + \frac{\%Cr + \%Mo + \%V}{5} + \frac{\%Ni + \%Cu}{15} \qquad [1.14]$$

Among the various steels presented in Table 1.1, and as mentioned in section 1.2.1, only H13 steel is sensitive to cold cracking since its carbon content is greater

than 0.1% by mass and its carbon equivalent is between 1.7 and 2.2% by mass. It is therefore recommended to produce it by preheating the build plate to a minimum temperature of 200°C.

1.2.5. *Examples of as-built microstructures*

1.2.5.1. *Austenitic stainless steels (316L)*

316L steels produced by AM do not undergo solid–solid transformations, with their as-built microstructure corresponding to their solidification microstructure. This microstructure is organized at different scales.

At the micrometer scale, the microstructure consists of a cellular substructure resulting from solidification. In DED, these cells are austenitic, and the intercellular spaces are ferritic due to the segregation of α-stabilizer chromium and molybdenum during solidification (section 1.2.3.2, Figure 1.11). In the case of elaboration by L-PBF, the microstructure is entirely austenitic, although the intercellular spaces are also enriched in chromium and molybdenum (Wang et al. 2018; Dépinoy et al. 2021) (Figure 1.16). These differences are explained by the effect of the solidification rate on the nature of the solidification phases (Figures 1.13 and 1.14). The material also contains a high dislocation density.

At a larger scale, these solidification cells are organized within large columnar grains oriented in the direction of solidification. Depending on the direction of the thermal gradient during solidification, these grains can have a crystallographic texture oriented in <100> or in <110> (Andreau et al. 2019). Controlling the shape of the fusion isotherm via the production parameters therefore makes it possible to control the final texture of the part (Figure 1.17).

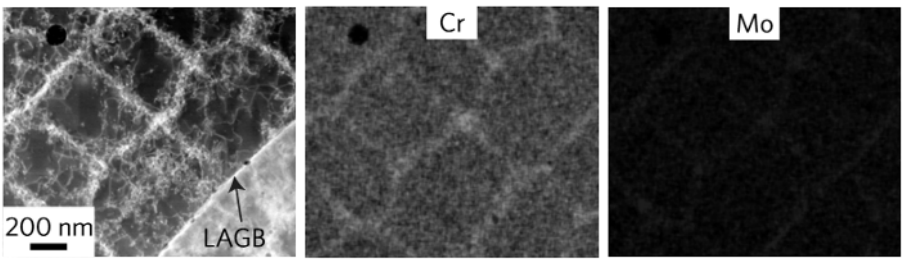

Figure 1.16. *Cellular substructure (HAADF-STEM) and segregations (STEM-EDS) of chrome and molybdenum in 316L steel elaborated via L-PBF (according to Wang et al. 2018). For a color version of this figure, see www.iste.co.uk/peyre/alloys2.zip*

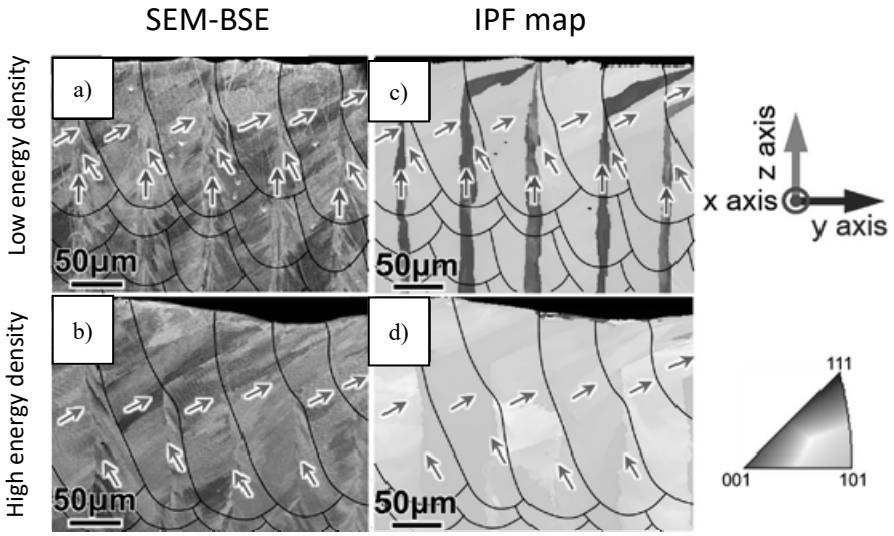

Figure 1.17. *Effect of operating conditions on the crystallographic orientation in the construction plane of a 316L steel (SEM micrographs in BSE mode on the left and IPF maps on the right). The arrows show the direction of cell growth (according to Sun et al. 2019). For a color version of this figure, see www.iste.co.uk/peyre/alloys2.zip*

1.2.5.2. *Hardened stainless steels (17-4PH)*

17-4PH steels show very large heterogeneity in microstructures depending on the conditions and the type of process used (Facchini et al. 2010; Rafi et al. 2014; Alnajjar et al. 2019). This versatility is a consequence of the L → δ (or L → δ + γ) solidification. Indeed, the two successive solid–solid transformations resulting from the δ ferrite (δ → γ then γ → α') can be incomplete or even completely inhibited. It is thus possible to obtain three totally different microstructures using L-PBF: (i) a predominantly α' martensitic microstructure containing retained austenite in the intercellular spaces (section 1.2.3.3.2), (ii) a predominantly ferritic δ due to the inhibition of the transformation δ → γ (section 1.2.3.3.1), or (iii) a predominantly austenitic γ microstructure due to nitrogen contamination inhibiting the transformation γ → α'.

The precipitation of hardening intermetallics (ε phase rich in Cu) can only occur during subsequent HT. A first step involving homogenization and quenching (sometimes at temperatures below 0°C) may be necessary to obtain the desired martensitic matrix.

1.2.5.3. *Maraging steels (18Ni-300)*

18Ni-300 steels produced by L-PBF (Kempen et al. 2011) and DED (Jägle et al. 2016) mainly consist of martensite with a non-negligible fraction of retained austenite. As shown in Figure 1.18, martensite is localized in the core of the solidification cells, whereas austenite is mainly found in the intercellular spaces enriched in titanium, nickel and molybdenum during solidification (see Figure 1.16 and section 1.2.3.3.2).

The precipitation of hardening intermetallics is very limited, and even non-existent during manufacturing. Maraging steels therefore require post-HTs in order to optimize their mechanical properties.

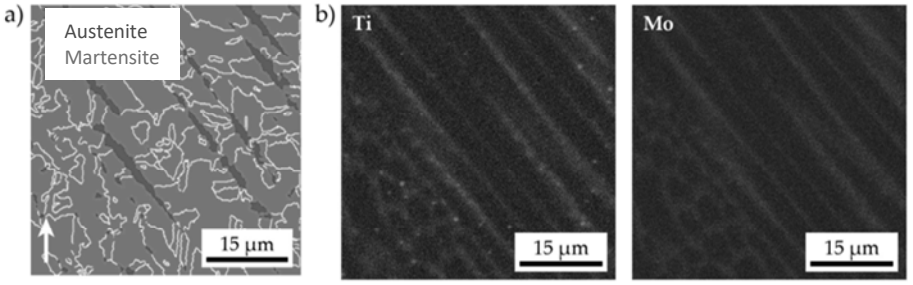

Figure 1.18. *(a) Electron back scattering diffraction (EBSD) mapping showing the retained austenite (in red) located between the martensite cells (in green) and (b) energy-dispersive X-ray spectroscopy (EDS) mapping showing the segregations of titanium and molybdenum in an 18Ni-300 steel produced with DED (according to Jägle et al. 2016). For a color version of this figure, see www.iste.co.uk/peyre/alloys2.zip*

1.2.5.4. *Carbon tool steels (H13)*

H13 steels produced by AM have a martensitic/austenitic microstructure similar to that of maraging steels (Figure 1.19). The stabilization of austenite occurs via the segregation of carbon, chromium, molybdenum and vanadium in the intercellular spaces (Deirmina et al. 2019). Since H13 steels are likely to crack when cold, they are produced by L-PBF with preheating of the build plate.

Carbide precipitation can be activated by this preheating or by the thermal cycles specific to the process, in particular in DED. In all cases, this precipitation may be incomplete and/or heterogeneously distributed in the material. Subsequent HT is therefore recommended to optimize the carbide precipitation.

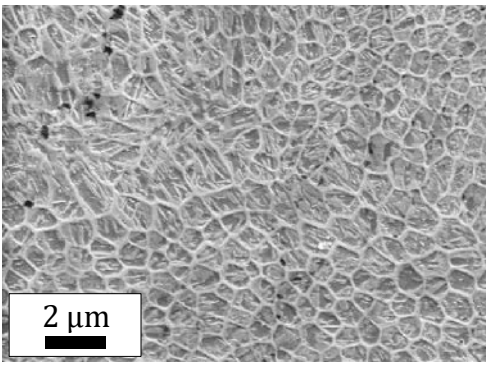

Figure 1.19. *Optical micrograph of an as built H13 steel showing an intragranular cellular network (Krell et al. 2018)*

1.2.6. *Summary of microstructural features of steels*

The microstructures of steels produced by AM are very different from those obtained by conventional processes due to the rapid solidification and cooling rates. Today, several types of steels, including steels known to be difficult to weld, can be produced by AM. Current work, driven in particular by the mold and tooling industry, aims at developing cold tool steels traditionally produced by powder metallurgy (sintering). These steels are particularly difficult to produce in AM by fusion, either because of a very high carbon content, making them particularly susceptible to cold cracking (between 1.4% and 1.6% by mass of carbon for D2 steel, more than 2% by mass for ASP 2078) or a very high melting point (higher than 3,600°C for M2 steel).

In parallel, many studies aim at better understanding the effect of AM parameters on the final microstructure, with the aim of controlling the microstructure by controlling the process. However, most studies on the AM of steels concern already existing grades which are not necessarily adapted to this new process: maraging steels, for example, require post-HT to optimize their mechanical properties. 17-4PH steel is an extreme case since three totally different microstructures can be obtained for a single grade of steel. A line of research still in its infancy today but destined to develop in the future is steels specifically designed for AM by fusion. The high dislocation density and the possibility of inhibiting specific phase transformations because of very fast solidification rates and cooling kinetics are examples of potentially beneficial effects of AM on the microstructure.

1.3. Microstructures of nickel-based superalloys

1.3.1. *Nickel-based superalloys and their applications*

Developed in the 1950s, superalloys were designed for high-temperature applications (>500°C), as they maintain good mechanical properties when hot (particularly in creep) and high resistance to corrosion or oxidation at high temperature. Based on iron, nickel or cobalt, they contain many alloying elements in significant quantities (such as chromium, titanium and aluminum, niobium and tantalum, molybdenum, tungsten or carbon), which give them their unique properties. They are found in many components such as gas turbines, rockets, heat exchangers, automotive turbochargers and even biomedical devices. Within this generic family, nickel-based superalloys are the most widely implemented in AM.

1.3.2. *General information on the metallurgy of nickel-based superalloys*

Nickel-based superalloys crystallize in a face-centered cubic (FCC) γ structure (Figure 1.20). They harden both in solid solution (by substitution of heavy elements like W, Mo and Ta as the major element) and by precipitation. The various chemical elements entering into the composition of superalloys and their respective roles are summarized in Figure 1.21. The main types of phases appearing in the form of precipitates at the heart of the microstructures formed are summarized below:

– *gamma prime* (γ') is an intermetallic compound of nominal composition $Ni_3(Al, Ti)$ whose lattice parameter is close to that of γ phase (Figure 1.20). It is stable over a relatively narrow range of compositions, and precipitates as spheroidal particles for alloys with low Al and Ti contents and cubic for higher Al and Ti contents;

– *gamma double prime* (γ") is a coherent precipitate of Ni_3Nb composition that precipitates in Nb-rich superalloys (Inconel 625 and 718). Under certain temperature/time conditions, an incoherent and embrittling delta (δ) phase precipitate of the same Ni_3Nb composition is formed in place of γ", which confers no reinforcement when present in large quantities. However, a small amount of δ refines the grain size, which improves the tensile, fatigue and creep properties;

– *Laves phases* generally precipitate during solidification or prolonged aging. They have a hexagonal crystallographic structure with the general formula $(Cr, Fe, Ni)_2(Si, Ti, Nb, Mo)$. They are brittle, and their precipitation deprives the matrix of hardening elements;

Section 1.3 written by Édouard CHAUVET, Florent FOURNIER-DIT-CHABERT and Patrice PEYRE.

– *carbides* (MC, $M_{23}C_6$, M_7C_3) have two effects: (1) at grain boundaries, they delay slip phenomena while allowing stress relaxation; (2) in the form of fine precipitation, they reinforce the γ matrix.

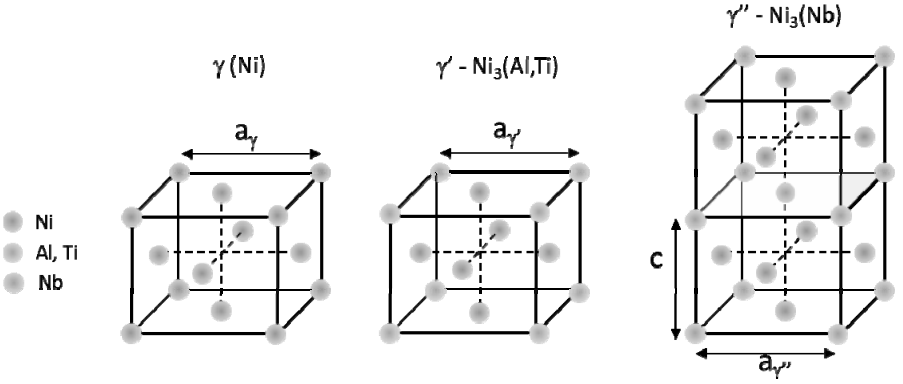

Figure 1.20. *Crystallographic structures of phases γ (CFC), γ' (Ni_3(Al,Ti)) and γ'' (Ni_3Nb). For a color version of this figure, see www.iste.co.uk/peyre/alloys2.zip*

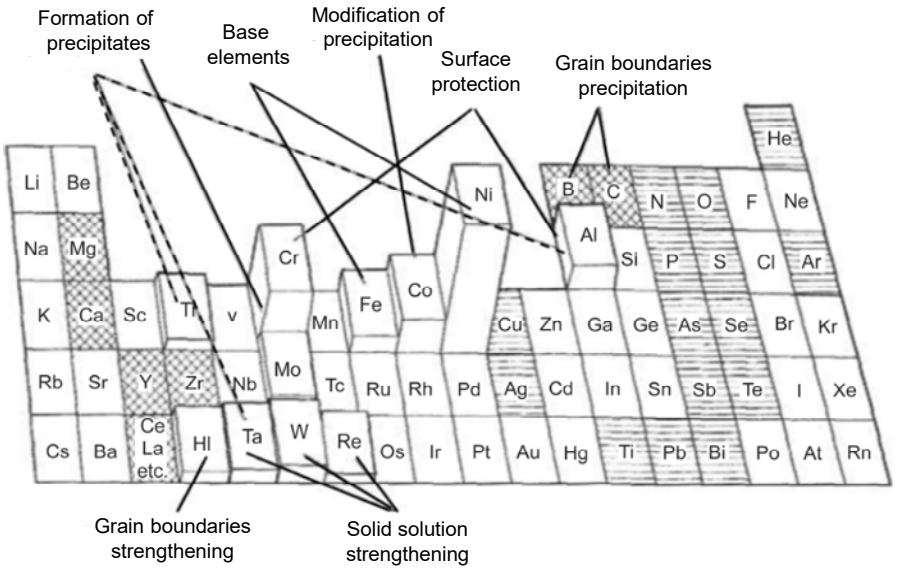

Figure 1.21. *Proportion of elements of the periodic table present in nickel-based superalloys and roles of the main ones (Davis 1997)*

1.3.3. *Two families of superalloys*

It is customary to separate nickel-based superalloys into two categories, depending on their weldability. The weldability of a material is a complex concept; the ISO 581:1980 standard offers a very broad definition: a metallic material is said to be weldable when, for a given process or application, its welding ensures good metallurgical health and the technical properties required of the welded part or the assembly of which it belongs. This property can be associated with a low susceptibility to cracking.

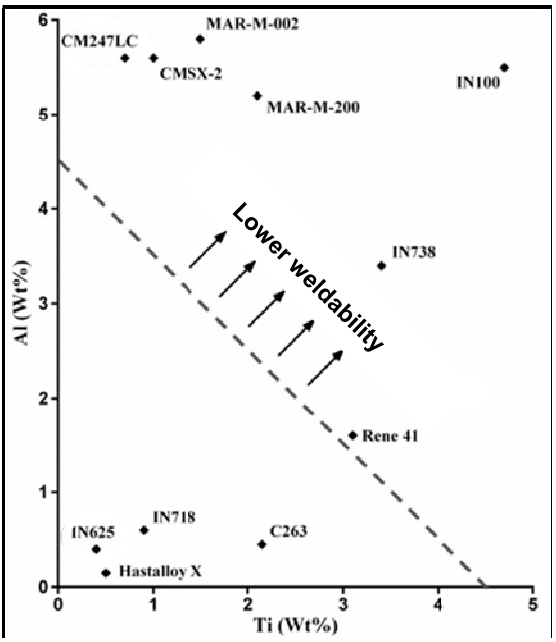

Figure 1.22. *Weldability of nickel-based superalloys. Beyond an Al + Ti mass fraction > 4.5%, the materials have a high fraction of γ' phase which increases their sensitivity to solid phase cracking during thermal tempering. For a color version of this figure, see www.iste.co.uk/peyre/alloys2.zip*

There are two categories of superalloys: so-called weldable alloys, with a low fraction of precipitates, and alloys that are difficult to weld, with fractions of precipitated γ' phases that can exceed 50% by volume and which exhibit cracking during cycles of fusion-solidification. In the superalloy welding literature, a classification according to Al and Ti composition (proportional to the volume fraction of γ' precipitates) is commonly used to establish the crack susceptibility of

the alloy. The limit between the two families of alloys is represented in the graph in Figure 1.22 by a straight line for an Al + Ti sum equal to 4.5% by mass.

Most alloys conventionally implemented in AM (Inconel 625, Inconel 718, see Table 1.4) are located in the lower part of the diagram (Catchpole-Smith et al. 2017). For so-called non-weldable alloys, we discuss the possible technological solutions to implement them without harming their integrity.

Alloy elements	Al	Ti	Fe	Nb/Ta	Mo	W	Co	Cr	Ni
Inconel 718	0.2–0.8	0.7–1	15–20	5–5.5	3	–	–	17–21	50–55
Inconel 625	<0.4	<0.4	<5	3–4	8–10	–	<1	20–23	57–61
Inconel 738	3.2–3.5	3.2–3.7	<0.5	2.5	1.5–2	2.4–2.8	8–8.5	15.7–16	60–62
CM247LC	5–6	0.5–1	<0.5	3	0.5	9.3	9–10	8–9	60–63

Table 1.4. *Chemical compositions (% mass) of four nickel-based superalloys (%C < 0.1–0.2% for all alloys, % Mn + % Si < 1%)*

1.3.4. *Microstructures of nickel-based alloys resulting from AM: weldable alloys*

The optimization of AM processes for so-called weldable superalloys (without cracking) involves, as for other alloys, the search for a parameter (P_0, V_0, hatch vector) of optimal densification and then, in most cases, optimization of post-manufacturing HTs, which condition the microstructures of use. We present below the as-built microstructures of two emblematic superalloys: Inconel 625 and Inconel 718. As a reminder, as with all cubic crystallography materials, the directions of preferential growth of nickel-based superalloys show <001> orientations of columnar grains parallel to the direction of manufacture, regardless of the AM process.

1.3.4.1. *Microstructures of Inconel 625*

Inconel 625 was developed in the 1950s for critical piping applications in steam power plants. In the forged or cast state, it is widely used for high temperature applications or in corrosive environments. This is the case for the petrochemical (piping, tanks), aeronautics and space (turbine blades and disks) industries, medical applications (prostheses, tools) and in the energy sector (gas turbines, heat exchangers-reactors). It has been the subject of a large number of recent studies in its raw state in AM (in particular DED and L-PBF) or after HT. Like all alloys made with L-PBF, the bulk fast solidification microstructure is columnar (Figure 1.23(a))

and oriented <100> (Murr et al. 2012), with grain slenderness ratios all the greater as the process parameters are energetic and promote significant remelting of the previous layers. At a lower scale, there is a cellular microstructure, with cell sizes of the order of 1–2 μm. In comparison, the as-built material fabricated with LMD exhibits a highly oriented cellular-dendritic microstructure, with intercellular spaces around 10–15 μm (Figure 1.24) due to cooling rates $\dot{T}$ (K/s) about a hundred times lower than in L-PBF (De Terris 2019).

In the unrefined state in L-PBF and in particular EBM, Inconel 625 may exhibit a fine precipitation of γ'' or NbC (size between 10 and 30 nm; see Figure 1.25; Murr *et al.* 2012) and has accelerated precipitation kinetics (in particular δ phase) during HT compared to a material produced in a foundry, probably due to the chemical segregation of Mo and Nb near the intercellular joints (Zhang et al. 2017a) and to the supersaturation of the γ matrix in alloying elements. Still in the raw state in L-PBF, it presents Nb, Cr and Mo in segregated intercellular zones and contains a high density of dislocations s (~10^{15} m^{-2}), which favors recrystallization (Figure 1.23(b)) during annealing around 1,100°C (Kreitcberg et al. 2017). This high dislocation density is probably due to the high solidification rate (V_s ~ 0.1–1 m/s) and, according to De Terris (2019), is perhaps associated with an equivalent mechanical hardening rate of around 15%. On the other hand, the as-built material fabricated by LMD does not recrystallize in the usual temperature cycles due to a 10 times lower dislocation density (De Terris 2019). The resulting static mechanical properties are, in the L-PBF or LMD raw state, anisotropic (weaker according to the manufacturing axis). They are also higher (in particular the elastic limit) than those obtained in forging (around σ_Y = 600 MPa versus 500 MPa for forged Inconel 625), contrary to the rupture elongation (around A = 25–30% against A = 35–40%).

Different post-treatments are recommended for Inconel 625 produced by L-PBF (Kreitcberg et al. 2017): (1) stress relaxation between 650°C and 800°C, (2) recrystallization annealing (950–1,100°C), (3) redissolving (1,050–1,200°C) to dissolve carbides and Laves phases and (4) hot isostatic pressing (HIP) (1,100–1,250°C/100–160 MPa). After re-dissolution treatment (section 2.3 of this volume) or HIP (section 2.2), Inconel 625 regains isotropic mechanical behavior and mechanical strengths close to those of the forged material (σ_Y ~ 400 MPa, R_m = 800 MPa and A ~ 50%). The microstructures from tempering treatment (TT) are accompanied by the formation of macles, absent from the as-built materials fabricated with L-PBF. Direct aging treatments between 600°C and 900°C on as-built Inconel 625 produced with L-PBF promote γ'' nanometric precipitation in the intercellular spaces at 600–700°C, which evolves into δ and Laves phases at 900°C. In both cases, the material then becomes harder, tougher and less ductile (Marchese et al. 2018) than the as-built material fabricated with L-PBF.

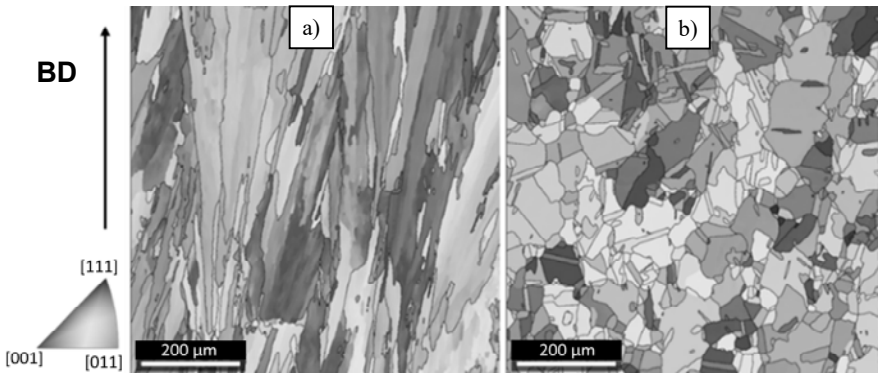

Figure 1.23. *EBSD maps of Inconel 625 (a) as-built from L-PBF (columnar grains and texture <001>) and (b) heat-treated at 1,100°C for 2 h and recrystallized (equiaxed grains, without preferential texture) (De Terris 2019). For a color version of this figure, see www.iste.co.uk/peyre/alloys2.zip*

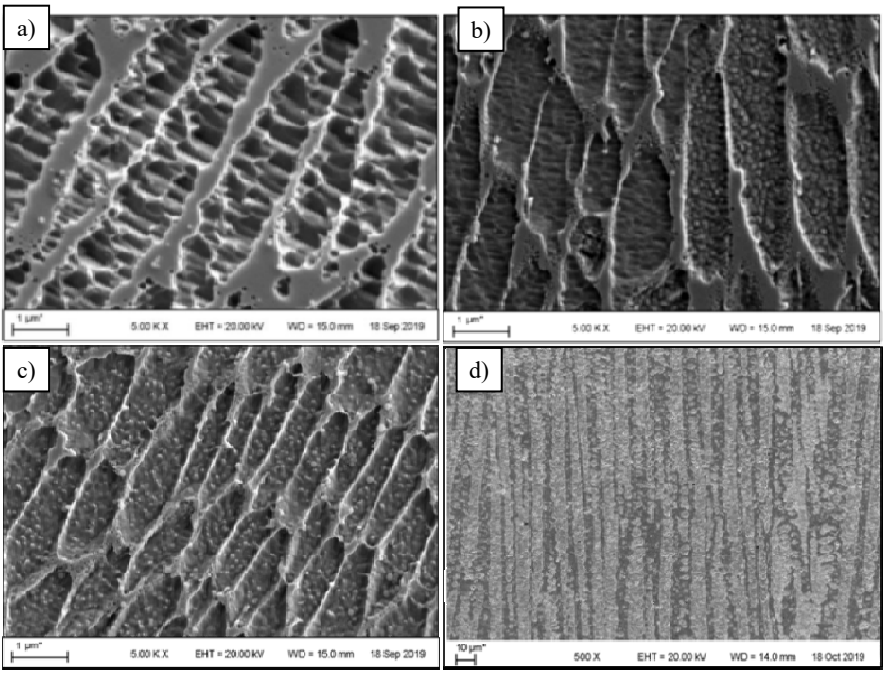

Figure 1.24. *Solidification microstructures (cellular) obtained for Inconel 625 after (a–c) L-PBF with less and less energetic conditions and (d) LMD (De Terris 2019)*

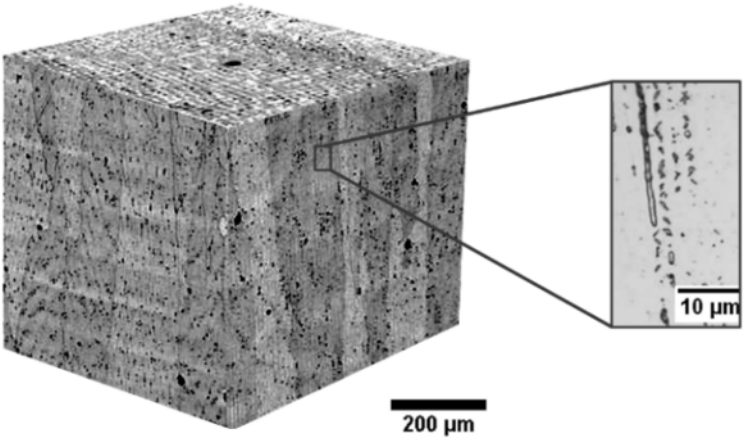

Figure 1.25. *Microstructure of Inconel 625 produced with EBM. (a) Three-dimensional optical micrograph of grain structure and (b) γ'' (Ni_3Nb) precipitates (Ni_3Nb) (Murr et al. 2012)*

1.3.4.2. *Microstructures of Inconel 718*

Inconel 718 is, like Ti-6Al-4V and 316L, one of the first materials to have been used in metal AM (Maisonneuve 2008). It is also the superalloy most used industrially, mainly in the hot parts of aircraft engines (>700°C), partly because of its moderate cost thanks to a high iron content. Usually, it is obtained by ingot-forging, that is, by (1) fusion then re-fusion under vacuum, (2) forging above (super-solvus) or below (sub-solvus) the solvus temperature δ (= dissolution of the δ phase), between 920°C and 1,100°C, and (3) precipitation of hardening phases (see section 2.3.3). As for Inconel 625, its high Cr content gives it good resistance to oxidation at high temperature and its main hardening phase is the γ'' Ni_3(Nb, Ta) phase in the form of nanometric discs combined with the γ' phase. For optimized conventional processes, the respective contents of phases γ'' and γ' are around 16% and 4%. In the as-manufactured L-PBF state, the γ grains are larger and more columnar than materials from conventional processes (Figure 1.26).

The crystallographic orientation (<100> // manufacturing direction), the nature and size of the γ'' Ni_3(Nb, Ta) precipitates formed are close to those obtained on Inconel 625. An important difference comes from the location of the γ'' precipitates, on {100} planes for Inconel 718 and on {111} planes for Inconel 625 (Murr et al. 2012). The as-built materials are also less hard than their forged equivalent due to a lower content of γ''/γ' precipitation for typical L-PBF cooling rates (~10^6 K/s). On the

other hand, the cast-forged samples exhibit the δ phase (Figure 1.26(a)), which has the effect of limiting the growth of the grains (Pröbstle et al. 2016).

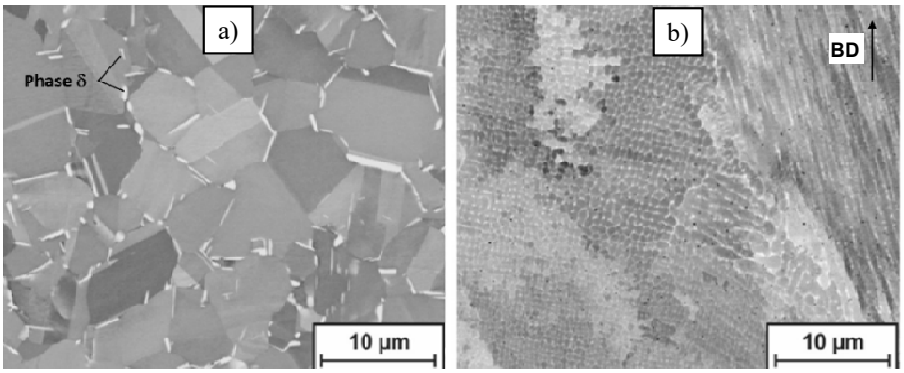

Figure 1.26. *Microstructure of Inconel 718 produced by (a) casting and forging and (b) L-PBF (Pröbstle et al. 2016)*

For materials developed by LMD, there is a generally columnar dendritic microstructure, oriented in the manufacturing direction. Certain experimental conditions, favoring the low dilution of the last layer (an insufficient ratio P_0 relative to the powder mass flow D_m), induce an equiaxed microstructure (Maisonneuve 2008). As with L-PBF, as-built materials produced by LMD are also less hard than the forged equivalent (about 280 HV vs. 380-400 HV), despite slower thermal cycles. In both cases (L-PBF and LMD), the alloys contain embrittling Laves phases (around 10–50 nm in L-PBF and a few µm in LMD) in the interdendritic spaces enriched in alloying elements Mo and Nb.

HTs carried out on Inconel 718 post-LMD, -EBM or -L-PBF are intended to dissolve the Laves phases and bring the γ''/γ' precipitates back into solution, then facilitate their controlled precipitation (Figure 1.27) via a solution–quenching-staged tempering process (at 720°C and then 620°C), which is followed by slow cooling.

The mechanical properties of AM Inconel 718 before HT compiled by Hosseini and Popovich (2019) show average mechanical strengths and rupture elongation between those of cast and forged alloys before and after HT. After tempering, the mechanical resistances (σ_Y and R_m) increase by +400 MPa in the materials produced by AM, compared to +200 MPa for the other processes, and the rupture elongation decreases in accordance with the formation of γ''/γ' precipitates.

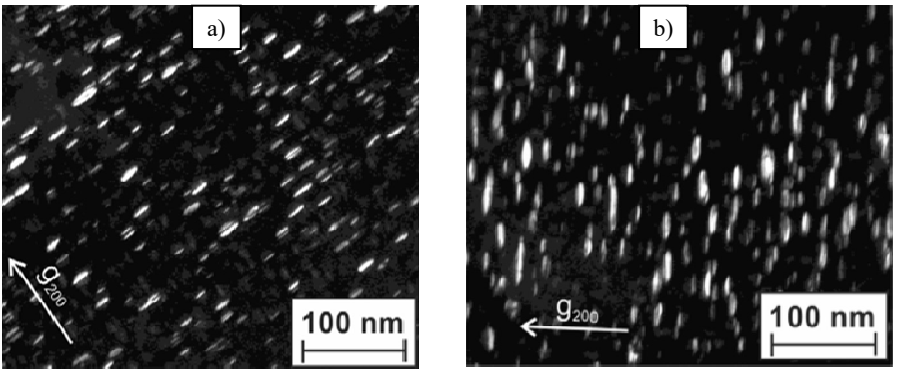

Figure 1.27. *γ''/γ' precipitation state after heat treatment of Inconel 718 produced by (a) foundry and forging and (b) L-PBF (Pröbstle et al. 2016)*

1.3.4.3. *Effects of manufacturing parameters on microstructures*

As mentioned at the beginning of this chapter, it is possible to modify microstructures by changing the manufacturing conditions. This results in modifications to the solidification front velocity V_s and thermal gradient at the solid–liquid interface G, which modifies both the solidification mode and the fineness of the microstructure. Hunt (1984) and Gong et al. (2014) show that when the scanning speed used for EBM fusion of Ti-6Al-4V increases, the width of the primary grains decreases. The grains of equiaxed morphologies can also be obtained by EBM due to the fragmentation of the secondary dendrite arms or by germination upstream of the solidification front (Körner and Bauereiß 2014). An EBM study (Figure 1.28) thus highlights the influence of melting parameters on the columnar or equiaxed microstructure (Körner et al. 2014; Dehoff et al. 2015). The possibility of a CET by modifying the manufacturing conditions of Inconel 718 has also been demonstrated with the LMD process (Parimi et al. 2014).

Overall, the crack density in samples of nickel-based superalloys (such as CM247LC) fabricated by L-PBF depends on the melting parameters (P_0, V_0) and scanning strategy (Carter et al. 2014). Ramsperger et al. (2016) indicate the possibility of obtaining non-cracked samples in CSMX-4 by EBM fabrication for high beam powers and low scanning speeds. It also seems that the density of cracks in as-built Inconel 738 from L-PBF is proportional to the depth of the fusion zone (or melt-pool), which itself depends on the operating conditions (Cloots et al. 2016). Finally, differences in microstructure are typically generated by modifying the fusion strategy (unidirectional or bidirectional scanning) during the manufacture of Inconel 718 in LMD (Parimi et al. 2014).

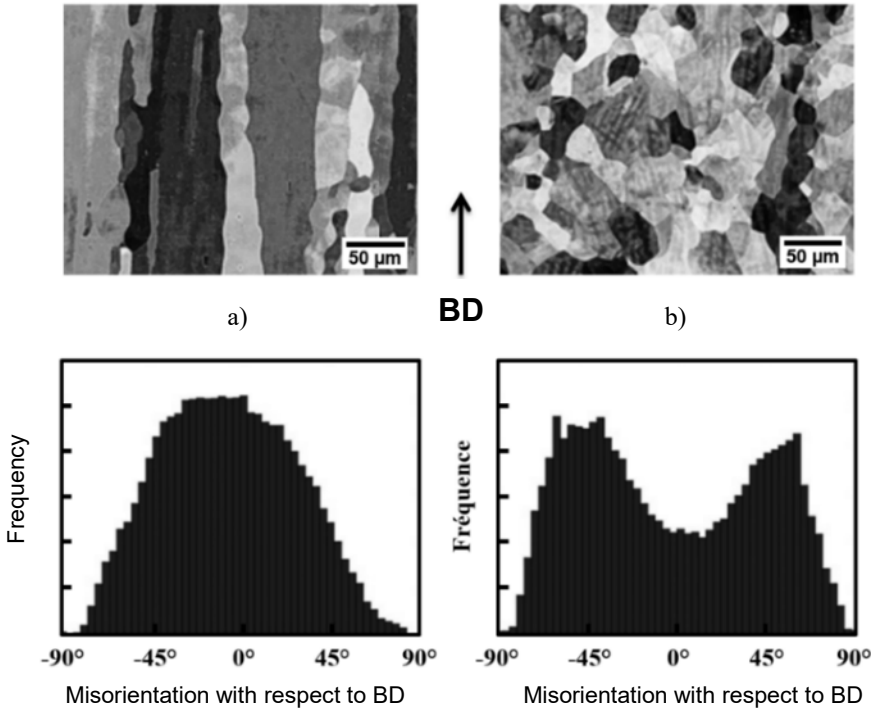

Figure 1.28. *SEM-BSE micrographs and change in orientation of the thermal gradients (by numerical simulation) of Inconel 718 with respect to the direction of construction (DC). (a) V_0 = 2,200 mm/s, hatch = e_V = 150 µm; (b) V_0 = 8,800 mm/s, hatch = e_V = 35.7 µm (Körner et al. 2014)*

1.3.5. *Hard-to-weld superalloys*

1.3.5.1. *Cracking problems*

The cracking mechanisms of superalloys (and several other materials) can be classified into two categories:

– solid-state mechanisms that develop when matter is fully solidified but at a relatively high temperature. Cracking by strain-age cracking during tempering is thus linked to a lack of accommodation of thermal stresses on materials with a high reinforcement rate (Figure 1.22) ((Al+Ti) > 4.5 wt.%), whereas cracking by ductility dip cracking is associated with a drop in solid phase ductility;

– the mechanisms in the liquid phase, which are associated with the existence of a liquid film in the microstructure, that is, before the end of solidification or during local melting/remelting of the material;

– associated problems can be encountered either during the direct AM of 3D parts or during repair by adding material, for example with the DED-LMD and WAAM processes.

1.3.5.1.1. Cracking at the end of solidification

Liquid phase cracking is often the cause of the cracks generated during L-PBF manufacturing. This mechanism can be summarized in several steps:

– during cooling of the fusion zone, there is a preferential growth of the material according to the direction of orientation [001], that is to say the manufacturing direction and the main direction of the thermal gradients;

– during solidification, local enrichment in alloying elements leads to the formation of chemical heterogeneities at the grain boundaries;

– the layer is then remelted several times, which leads to a greater and more localized enrichment in alloying elements;

– subsequently, with the construction of additional layers, the material is only partially melted in the areas where the melting temperature is the lowest. A liquid film is then persistent, especially at highly disoriented grain boundaries;

– at the same time, thermal contraction and solidification shrinkage lead to deformations in the semi-solid state. When these deformations can no longer be accommodated, this leads to cracking.

Within the framework of a dendritic columnar solidification when there is coexistence of the liquid phase and the solid phase, three zones can be distinguished (Figure 1.29). In zone 1, the circulation of the liquid in the solid structure makes it possible to accommodate the deformations, while in zone 3, the bridges created between the secondary arms of dendrites form a solid structure capable of resisting stresses (transmission of forces). In zone 2, near the future grain boundary, there is still a liquid film between the solidification dendrites, but the liquid supply is no longer sufficient. Thus, the deformations cannot be properly accommodated by the supply of new liquid or transmitted by the solid bridges created between the arms of secondary dendrites (Wang et al. 2004). The spaces between the still unsolidified dendrite networks then open up. This is the cracking phenomenon at the end of solidification. It generates a dendritic fracture surface.

As soon as cracking has started in the microstructure, the cracks can propagate. The growth by epitaxy caused by the remelting of the layers generates a growth of the grains on both sides of the propagation path of the crack. This type of crack propagation pattern is similar to that observed during the shaping of non-weldable superalloys by L-PBF (Cloots et al. 2016) or by EBM (Chauvet et al. 2018). Finally, on the CM247LC, Boswell et al. (2019) show cracking problems during HTs (between 450 and 800°C) for L-PBF samples. Cracking due to tempering or loss of ductility (ductility dip cracking) in heat-affected zones (HAZs) over the 700–800°C range then occurs.

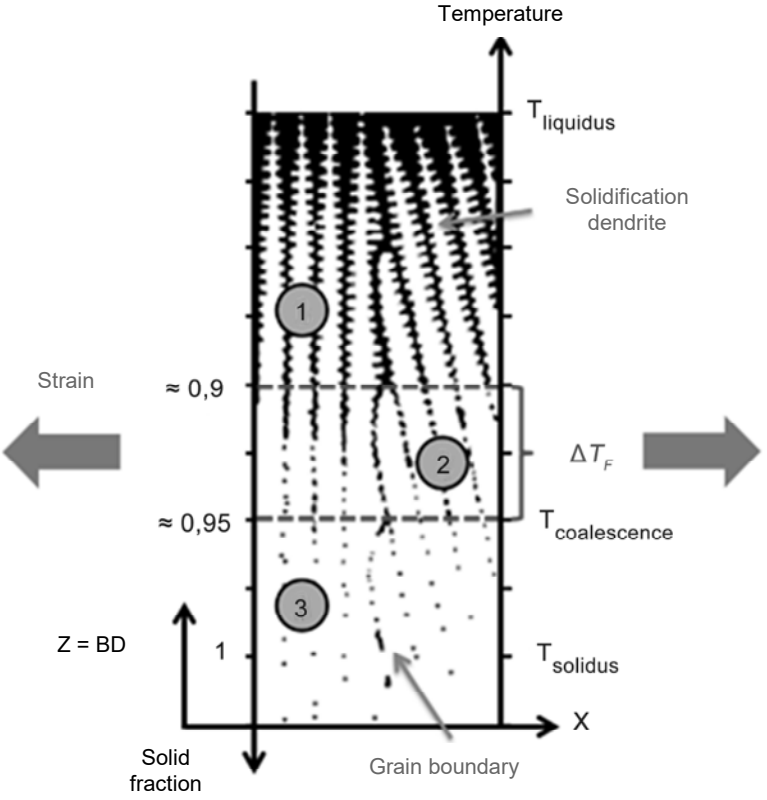

Figure 1.29. *Diagram of the solidification of a columnar dendritic structure*

1.3.5.1.2. Liquation cracking

Liquation refers to the phenomenon of melting of a heterogeneity in a metallic alloy, at a temperature below the solidus temperature of the alloy. During a rise in

temperature, a liquid film will thus be formed on these heterogeneities. As with cracking at the end of solidification, under the effect of cooling and solidification shrinkage, the solid will contract and cause cracking in the zone of the liquid film often located at the grain boundaries. Additional stresses can also develop during the precipitation of hardening phases. The ability of the material to accommodate the deformations is then reduced, which accentuates the cracking mechanism. This mechanism is therefore associated with local melting of the alloy and the presence of thermal or mechanical stresses (Figure 1.30).

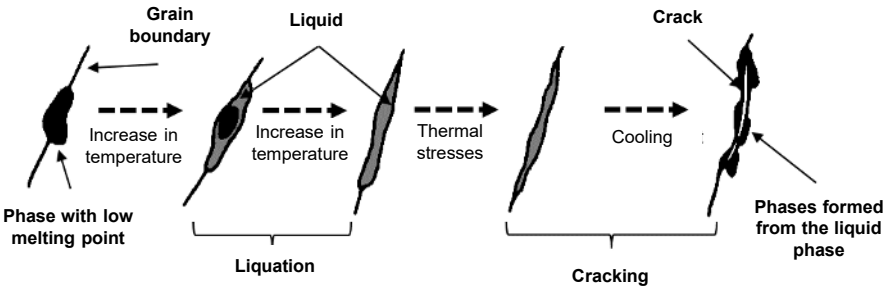

Figure 1.30. *Principle of the mechanism of cracking by liquation (DuPont et al. 1998)*

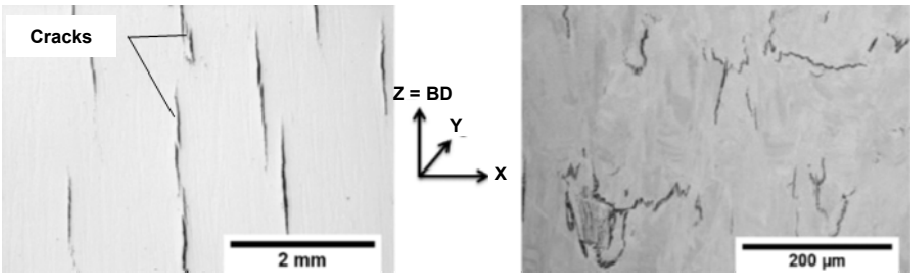

a) b)

Figure 1.31. *Cracking phenomenon in additive manufacturing: (a) CMSX-4 obtained from EBM (according to Körner et al. 2014) and (b) CM247LC obtained from L-PBF (according to Carter et al. 2014)*

Age-hardened nickel-based γ' superalloys are particularly sensitive to cracking by liquation due to the additional contribution of mechanical stresses generated by precipitation (Royer 2014). Thus, in Inconel 738, secondary phases such as MC-type carbides or M_3B_2-type borides are melted by liquation and lead to the formation of a liquid film in the partial fusion zone (PFZ) during welding, which

leads to cracking. At the same time, the γ′ precipitation causes hardening of the matrix and the precipitates can participate in the formation of liquid by constitutional liquefaction (Ojo et al. 2006).

The implementation of powder bed processes with this type of difficult-to-weld superalloy has also been the subject of a large number of recent studies. Almost all of these studies indicate the presence of cracks (Figure 1.31).

1.3.5.2. *Solutions implemented in AM*

Different solutions can be used to combat this cracking. The possibility of using the DED-LMD technique to repair/rebuild certain damaged areas of aeronautical parts either after use, or because they present raw manufacturing defects was recently studied with Inconel 738 (Doghri 2019) and CM247LC (Bidron et al. 2020). In both cases, the materials have a high content of γ′ cuboids (55–60% of γ′), which predestine them to cracking. However, the cracks that appeared during LMD were more a reflection of HAZ liquefaction phenomena, with rapid and partial remelting of the large primary γ′ near the grain boundaries. Preheating slightly below the dissolution temperature of γ′ (solvus = 1,180°C), that is to say in the region of 1,000–1,100°C (with inductive heating), made it possible to carry out reloading without cracking on damaged and scoured areas (Figure 1.32).

For Guraya et al. (2019), the use of a deep melting regime (keyhole) in L-PBF with Inconel 738 LC made it possible to obtain non-cracked materials, by limiting the vertical orientation of the γ grains, whereas Wang et al. (2019) failed to obtain completely uncracked materials, the cracks being formed in the γ/γ′ eutectics present at the grain boundaries. In this last study, an HIP treatment (1,175°C, 100 MPa, 4 h) followed by a re-dissolution HT and staged aging allowed defects to be closed (porosity and cracks) and made it possible to obtain equivalent mechanical properties to those of forged Inconel 738 LC. More precisely, the HIP had the dual effect of (1) re-dissolving the highly segregated Ti in the interdendritic spaces and (2) relaxing the residual stresses.

For L-PBF, studies are currently underway to couple the main laser source with a second laser source to reduce the pre- and post-heating kinetics, and therefore the thermal gradients and the associated stresses and strains. Manufacturing with EBM seems a priori more suitable for this type of cracking alloy due to the high temperature preheating that precedes the melting pass (see section 1.3 in Volume 1). Thus, Chauvet et al. (2018) fabricated nickel-based superalloys containing (Al+Ti) = 8.6 wt.%, with preheating around 1,050°C. However, even under these conditions, cracks were detected at the most crystallographically disoriented grain boundaries, essentially in the upper parts of the manufactured parts, presenting the largest grains. The tearing of residual liquid films in the fusion

zone (FZ) or in the HAZ close to the FZ (liquation) during solidification is at the origin of the cracks formed (Figure 1.33).

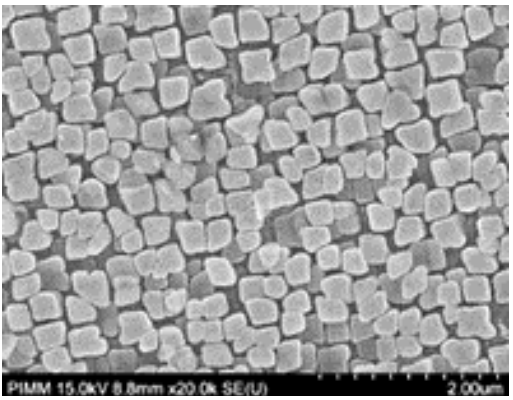

a)

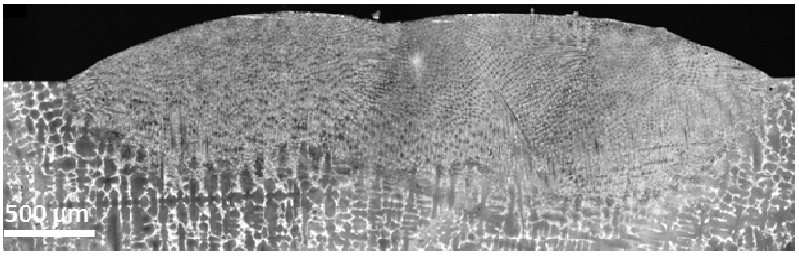

b)

Figure 1.32. *Repair of CM247LC via LMD: (a) initial microstructure (60% of γ'); (b) area repaired by overlapping two beads with preheating at 1,050°C (Bidron et al. 2020)*

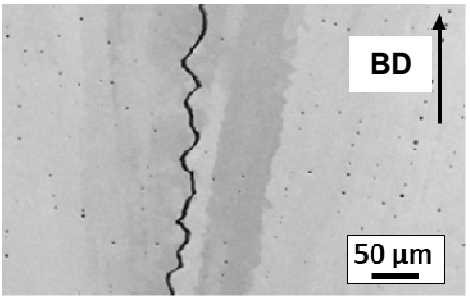

Figure 1.33. *EBM microstructure of an 8.6 wt.% (Ti + Al) superalloy with an intergranular crack (Chauvet et al. 2018)*

However, different strategies have been proposed in order to eliminate this cracking: (1) increase the density of highly disoriented grain boundaries, that is, fine-grained micro-structure: better accommodation of the thermal deformations generated during the process and more homogeneous distribution of segregations; (2) eliminate grain boundaries, that is, a single-crystal microstructure, meaning no initiation site for cracking and (3) create porosities, that is, a porous microstructure, meaning disruption of growth by grain epitaxy and preservation of a fine microstructure, as well as relaxation of part of the thermal stresses.

1.3.6. *Overview of the microstructures of superalloys*

In summary, nickel-based superalloys are very widely implemented in AM. They can be classified into two categories: (1) those which, like Inconel 718 and 625, are weldable and with Al + Ti content less than 4.5% by mass and (2) those which, like Inconel 738, are difficult to weld, whose Al + Ti content exceeds 4.5% by mass and which contain a large volume fraction of γ'- Ni_3 (Al Ti) precipitates. To develop nickel-based superalloys in AM, most of the work involves limiting porosities and avoiding cracking during manufacturing. This requires mastery of the implementation parameters and optimization of HTs (annealing → quenching → tempering), without which this type of material is never used industrially. In terms of microstructures, it is therefore a question of ensuring a state of optimal γ' or γ'' precipitation, while avoiding certain detrimental phases such as Laves phases.

1.4. Microstructures of titanium alloys

Due to their high specific strength, biocompatibility and high temperature stability, titanium alloys are used for high value applications in various industries, such as the automotive, naval, aerospace, chemistry and biomedical industries. The AM of titanium is a subject of considerable interest from both the industrial and scientific community. With 70% of world production, Ti-6Al-4V (still denoted TA6V) is the most widely used titanium alloy in industry. It is a type α + β alloy where α is the hard phase and β is the ductile phase. In addition to titanium, it contains 6% by mass of aluminum, 4% by mass of vanadium and other elements in the form of traces (Fe, C, O, N and H) according to the F136 ASTM standard. This alloy offers a good compromise between mechanical strength and rupture elongation, but can only be used below a temperature of around 300°C. On the other hand, it is very sensitive to oxidation and ambient humidity, requiring suitable

Section 1.4 written by Guilhem MARTIN, Christophe COLIN, Charlotte DE FORMANOIR, Stéphane GODET and Jean-Jacques BLANDIN.

storage conditions. Indeed, its ductility is greatly reduced by dissolved oxygen and hydrogen (Kahveci et al. 1986; Pitt et al. 2004). For example, aeronautical standards impose a dissolved oxygen level of less than 2,000 ppm (i.e. 0.2% by mass) fir the certification of aircraftable parts in TA6V (Vinson 2015). The hydrogen level must remain below 200 ppm because beyond that an embrittlement of the alloy by the precipitation of titanium hydrides is likely to occur. Finally, aluminum is an element with high vapor pressure (700 Pa at 1,727°C) compared to the other two elements (Ti and V). As a result, aluminum has a strong ability to vaporize from the melt-pool formed under a beam of electrons or high-energy photons.

1.4.1. *Phases and phase transformations*

There are two allotropic forms of titanium at thermodynamic equilibrium: the pseudo-compact hexagonal α phase (a_α = 2.950Å and c_α = 4.683Å) and the cubic centered β phase (a_β = 3.290Å) (Combres et al. 1995). The prevalence of one or the other phase depends on two parameters: the temperature and the chemical composition of the alloy (Figure 1.34). Thus, the transus temperature Tβ separates phases α ($T < T_\beta$) and β ($T > T_\beta$). Some alloying elements affect the relative stability of each phase by changing the temperature T_β: one thus distinguishes the α-stabilizer elements (aluminum, oxygen, carbon, nitrogen) stabilizing the α phase from β-stabilizer elements (molybdenum, vanadium, niobium, etc.) stabilizing the β phase. The addition of β-stabilizer elements can cause a mixed α + β domain to appear controlled by temperatures T_α and T_β. Thus, according to their chemical composition, titanium alloys can be classified according to thermodynamically stable phases at room temperature: α alloys, β alloys and α + β alloys, among which Ti-6Al-4V belongs (Lampman et al. 1990).

Besides α and β phases, a third metastable α' martensitic phase, with a hexagonal structure and lattice parameters almost identical to phase α ($a_{\alpha'} \approx a_\alpha$ and $c_{\alpha'} \leq c_\alpha$), can form without diffusion during rapid cooling (greater than 410°C/s; Ahmed et al. 1998) from the β phase below temperature M_s. This temperature depends on the chemical composition of the alloy and, in particular, on the addition of β-stabilizer elements, which has the effect of lowering M_s, unlike α-stabilizer elements which increase it. The $\beta \rightarrow \alpha'$ transformation is considered complete after the representative point of the alloy has reached temperature M_f at the end of transformation, which is also a function of the chemical composition of the alloy, but also of the quenching speed, unlike the temperature M_s (Combres et al. 1995). The α' phase is characterized by a chemical composition identical to that of β phase from which it originates.

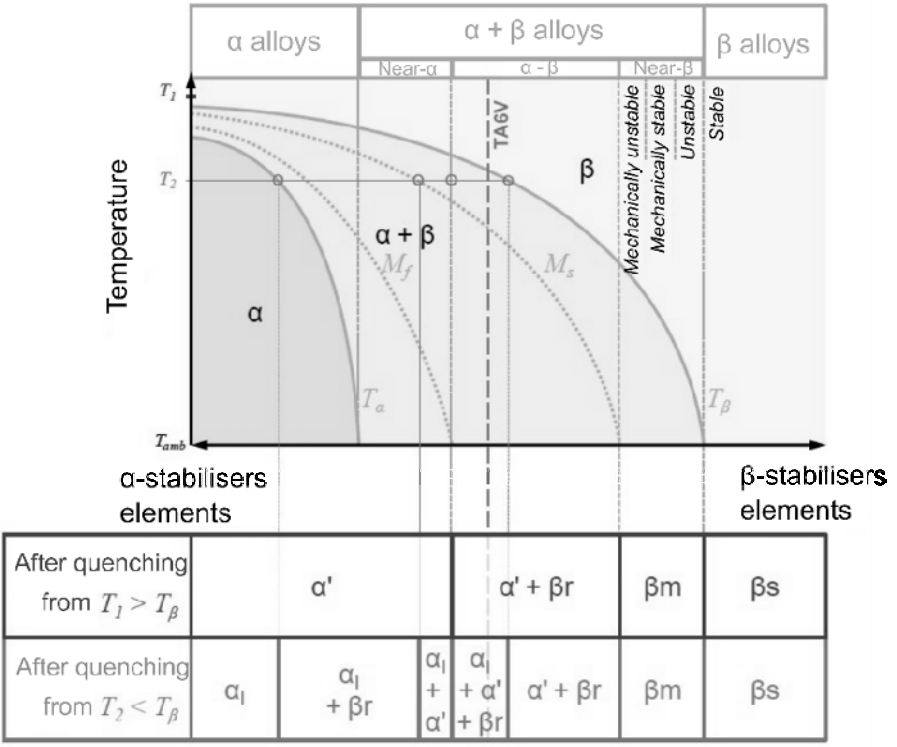

Figure 1.34. *Pseudo-binary diagram and potential microstructures of titanium alloy families (Vinson 2015). Note here that the M_f temperature of the TA6V is below ambient temperature but researchers are still divided on the value of this temperature (Seraphin 1965; Hocheid et al. 1970; Brooks 1982; Combres et al. 1995). For a color version of this figure, see www.iste.co.uk/peyre/alloys2.zip*

As a rule, titanium alloys are mainly made up of one or more of these three phases, the morphology and chemical composition of which will depend on the thermal history and the composition of the alloy. In the case of alloys cast or fused by different energy sources, the α phase is essentially in the acicular or lamellar form, its globular form being essentially the result of a thermomechanical shaping process (hot forging). At room temperature T_{amb}, it is possible to differentiate between the residual phase β_r and the metastable phase β_m from the incomplete martensitic transformation $\beta \rightarrow \alpha'$ ($M_f < T_{amb}$) after rapid cooling from the β domain ($T > T_\beta$). The residual phase β_r results from out-of-equilibrium cooling of an alloy whose nominal composition is such that its cooling "curve" on Figure 1.34 intersects the M_s line but not the M_f one (Brooks 1982), and the metastable phase β_m is the

β phase retained at ambient temperature with its high temperature chemical composition, but subsequent HTs may result in its transformation into more stable phases (Maisonneuve 2008). Alloys containing enough β-stabilizer elements to lower the temperature M_s at the start of martensitic transformation down to T_{amb} are likely to retain the β_m phase at room temperature (Table 1.5). The stable phase β_s is the β phase retained at room temperature after cooling of an alloy whose nominal composition no longer crosses the T_β line. We then speak of a β phase chemically stabilized by the enrichment of β-stabilizer elements such that it is impossible to transform by thermal and thermo-mechanical processing, unlike the β_m phase. Figure 1.34 describes the phases present at room temperature as a function of the chemical composition of the alloy depending on whether the alloy is quenched from the single-phase range β ($T_1 > T_\beta$) or the two-phase domain α + β ($T_2 < T_\beta$). The difference between these two quenching domains results in the presence of a pre-existing phase α_I (also called primary α) until the composition of the alloy intersects the line T_β.

Elements	Mo	V	Nb	Ta	Mn	Fe	Cr	Co	W	Ni	Cu
%min for β_m	10	15	36	45	6.4	3.5	6.3	7	22.5	9	13

Table 1.5. *Mass percentage of a β-stabilizer element necessary for the conservation of the β_m phase at room temperature (Seraphin 1965)*

Due to the particular thermal history caused by LMD (or DED), L-PBF and EBM (or E-PBF) processes, defects are frequently observed, and a specific microstructure is generated within titanium alloys. These aspects are detailed below for Ti-6Al-4V and for each of the three processes.

1.4.2. *Microstructures of titanium alloys resulting from the DED process*

1.4.2.1. *Evolution of the phase distribution of Ti-6Al-4V during manufacture*

During the construction of a Ti-6Al-4V part in the DED process, the successive deposition of layers induces an in situ HT in the layers already constructed, causing their microstructure to evolve after solidification (Maisonneuve 2008; White 2017). This HT that an already constructed layer undergoes can be broken down into four stages, as shown in Figure 1.35, where the first heating–cooling cycle corresponds to the deposition of the layer in question and each subsequent cycle corresponds to the deposition of a new layer. The in situ HT of a given layer is characterized by two temperatures, minimum T_0 and maximum T_{peak}, as well as by the heating and cooling rate between these two temperatures associated with each cycle. Remember

that the heating rate is much higher (≈2.5 times) than the cooling rate (Maisonneuve 2008).

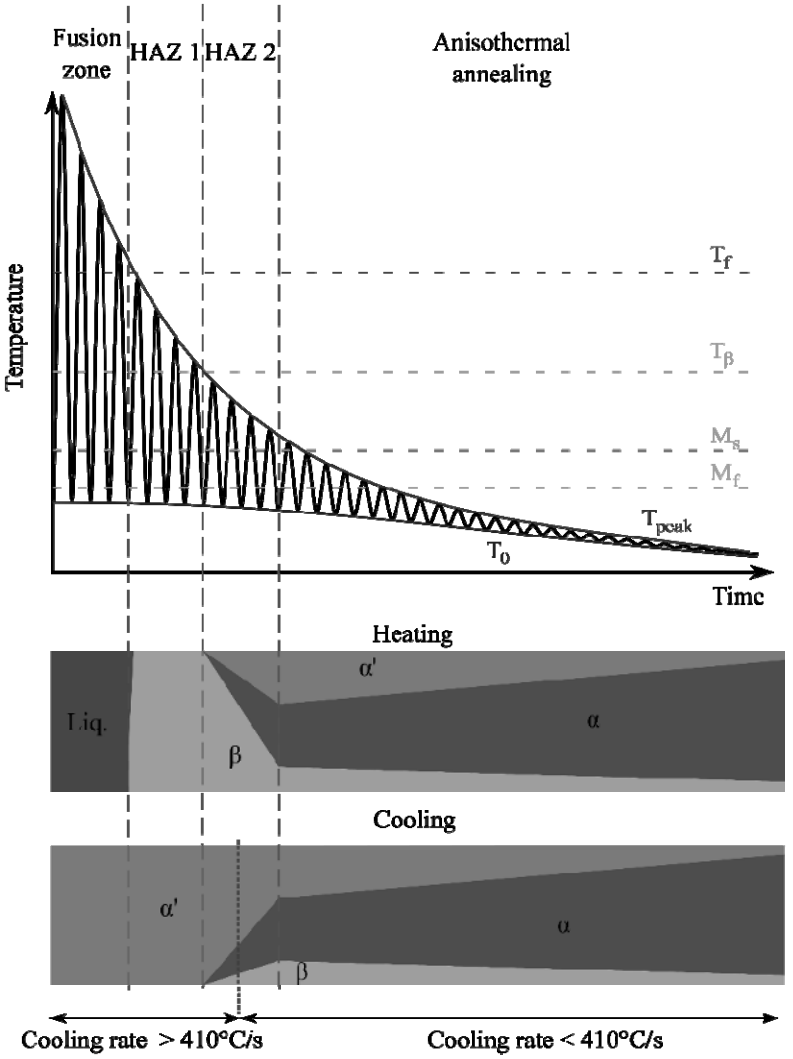

Figure 1.35. *Schematic representation of the thermal history of a given layer undergoing temperature cycling during the construction of a Ti-6Al-4V part and the resulting microstructure (here we do not distinguish between β_r phases and the eventual β_m of phase β). For a color version of this figure, see www.iste.co.uk/peyre/alloys2.zip*

During its deposition, the layer is in the liquid state. On cooling, the liquid solidifies into the β phase, and then transforms into the α' martensite due to rapid quenching rates of around 1,000°C/s. This fusion–solidification–transformation cycle is repeated for a certain number of successive layer depositions as long as the maximum T_{peak} temperature reached by the considered layer, whose thermal history is followed, is higher than the melting temperature T_f (=1,660°C). After a certain number of deposited layers, the T_{peak} temperature becomes lower than T_f but remains higher than the transus temperature T_β (=980°C). In this thermal regime, corresponding to HAZ_1 in Figure 1.35, the layer under consideration undergoes a complete α' → β transformation on heating, then, with the cooling rate always being higher than 410°C/s, a complete β → α' transformation is observed when passing M_f (650–800°C according to the cooling rates; Combres et al. 1995) during cooling. Note that in the fusion zone and HAZ_1, the minimum temperature T_0 is assumed to be lower than M_f, so that no residual β is present after cooling.

As new layers are deposited, the T_{peak} temperature continues to decrease until it becomes lower than the transus temperature T_β. The layer is then in a thermal regime controlled by T_β and M_s (780–900°C according to Hocheid *et al.* (1970) and Combres et al. (1995)) corresponding to HAZ_2. During heating, the α' martensite inherited from previous thermal cycles decomposes into α + β. This transformation is only partial, and the kinetics induced by the thermal cycling are still too fast to ensure the total transformation of the α' martensite. The proportion of α and β phases transformed during heating depends on both the heating rate and the T_{peak} temperature. The lower the speed, the more the α phase is favored to the detriment of the β phase. Thus, during the successive deposition of new layers, more and more α phase will be formed on heating in the layer considered as long as the peak temperature is high enough. This α phase, being thermodynamically stable at T_0, will not transform during cooling, and only its composition will change. Conversely, the β phase formed during heating initially transforms into α' martensite during cooling as long as the cooling rate remains above 410°C/s (the case of the first layers in HAZ_2). However, as thermal cycles and successive α' → α + β transformations progress, the β-stabilizer elements diffuse from the α phase to the β phase, chemically stabilizing the latter and lowering the temperature at the end of martensitic transformation M_f. Thus, less and less α′ phase will be formed during cooling and more and more β phase will be stabilized as successive layers are deposited. From a certain moment, the amplitude between the T_0 and T_{peak} temperatures becomes too small for the cooling rate to be less than 410°C/s. Consequently, there is no longer any formation of α' martensite during cooling and the β phase formed during heating is mainly transformed into α. After a fairly large number of new layers deposited, the amplitude between T_0 and T_{peak} becomes so low that the temperature oscillations due to the deposition of new layers become almost

negligible. The layer considered then enters an anisothermal annealing regime, where the distinction between heating and cooling no longer must be made. During this annealing, the metastable α' and β phases inherited from previous thermal cycles are gradually and mainly transformed into thermodynamically stable α, becoming quicker as the T_0 increases.

The minimum temperature, T_0, is very dependent on the position of the considered layer with respect to the build plate, which at the start is at ambient temperature. Indeed, because of the thermal pumping that it induces, the temperature T_0 of the layers near the plate is close to the ambient temperature. In fact, the cooling rates are always greater than 410°C/s and an anisothermal annealing regime cannot quickly set in. The first layers therefore consist mostly of α' martensite (Maisonneuve 2008). As one moves away from the build plate, its pumping effect decreases and the temperature T_0 of the layers already built increases until it reaches an asymptotic value independent of the position of the layer.

Thus, the microstructure of a Ti-6Al-4V part built in DED is very heterogeneous in the construction direction. With the last deposited layers (top of the part) not having been re-exposed to the laser beam, the fusion zone and the HAZ_1 will be entirely martensitic. Further down, the part consists of an α' + α + β mixture, resulting from the HAZ_2 thermal regime and anisothermal annealing, where the proportion of each phase varies according to the distance from the plate such that the fraction of the α phase increases when the layer considered approaches the plate. However, due to the thermal pumping of the latter, the first layers deposited mainly consist of α' martensite as long as the T_0 temperature remains sufficiently low with respect to the decomposition temperature of the α' phase into α + β for the duration of manufacture (Gil Mur et al. 1996; Marion 2016).

1.4.2.2. *Grain morphology: CET*

As seen in section 1.1, grains can solidify according to a columnar or equiaxed morphology depending on the solidification rate V_s and the thermal gradient G recorded on the melting isotherm (Kobryn et al. 2003; Bontha et al. 2006). In fact, the appearance of equiaxed or columnar grains depends on how the part cools locally: by conduction in the build plate, by natural or forced convection from the surrounding gaseous medium or by radiation from the fusion zone. Of these three modes of heat dissipation, conduction remains the most important mechanism, favoring heat flow directed toward the bottom of the part and parallel to the manufacturing axis (Longuet 2010). Moreover, the number of layers remelted at each deposit influences the growth by epitaxy of the grains. Thus, depending on the parameters of the process alone, the Ti-6Al-4V produced by DED can thus, and

more easily than L-PBF, have a varied microstructure, either entirely columnar or entirely equiaxed, or even mixed columnar-equiaxed (Figure 1.36).

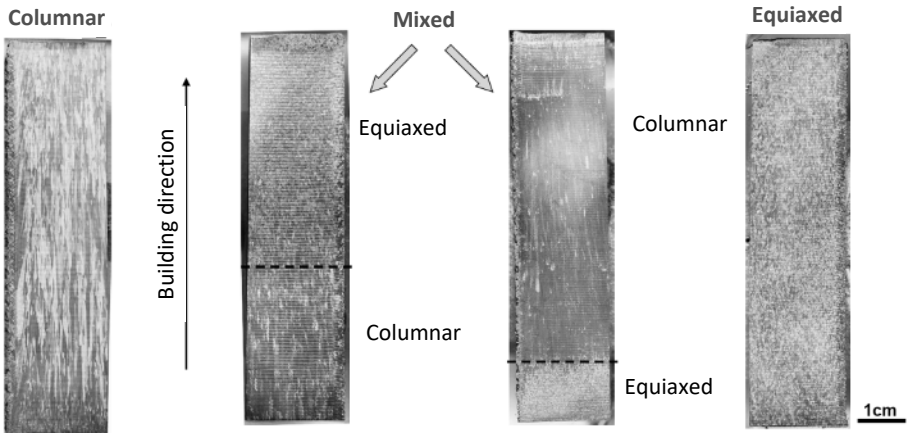

Figure 1.36. *Possible grain morphologies after construction of a Ti-6Ai-4V wall (Maisonneuve 2008)*

It is thus possible to obtain a part with equiaxed grains in a few layers in the part close to the plate, then columnar in the rest of the part. This CET can be explained by the fact that the first layers deposited cool very quickly by conduction in the plate. As the deposition of the following layers makes it possible to sufficiently remelt the top of the already solidified grains, the new grains solidify in an equiaxed manner. As the construction progresses, cooling by conduction becomes less and less effective as the new layers deposited are further away from the plate. The T_0 temperature therefore increases and the remelted zone becomes increasingly large in volume, leading to the remelting of the already solidified grains. Moreover, with dissipation by conduction remaining greater than that of convection, thermal gradients perpendicular to the plate appear. These two phenomena then lead to the growth of columnar grains. Conversely, it is possible to start by forming columnar grains in the layers close to the plate, then equiaxed grains in the rest of the part. Indeed, if a sufficient number of layers are remelted from the first layers deposited, dissipation by conduction linked to the presence of the cold substrate will cause very strong thermal gradients in the direction of construction and lead to the growth of columnar grains. As the construction progresses, these gradients will decrease in intensity due to the increase in T_0 temperature and the new grains will then be equiaxed. In general, increasing the laser power and decreasing the deposition rate will promote the appearance of columnar grains.

1.4.3. *Microstructures of titanium alloys from the L-PBF process*

1.4.3.1. *Porosity*

Porosity within the Ti-6Al-4V formed by the L-PBF process originates in multiple ways. Two essential types of porosity are generated during the L-PBF process: keyhole type pores and pores resulting from a lack of fusion.

The keyhole type pores are quasi-spherical and small in size (10–50 μm) (Figure 1.37), resulting from the formation in the laser incidence zone of a deep gaseous or a plasma depression in the melt-pool, the collapse of which traps argon (Figure 1.38). These pores are typically observed when the energy input is excessive, which promotes the vaporization of the melt-pool surface (metallic vapor pressure) and generates a recoil pressure (proportional to the saturated vapor pressure), which vertically deforms the surface of the melt-pool and causes liquid to rise along the capillary. Although the formation of the keyhole type of pore is stochastic in nature, this type of pore is more frequently observed at the laser cusps, where the energy input increases locally (Martin et al. 2019).

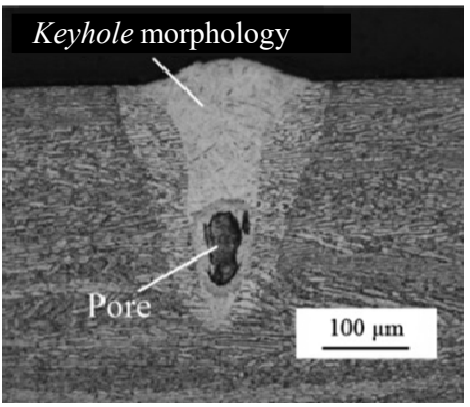

Figure 1.37. *Micrograph showing the cross-section of a keyhole-type melt-pool within Ti-6Al-4V formed by L-PBF (Gong et al. 2014)*

When, in contrast, the supply of energy is insufficient, another type of pore, resulting this time from a lack of fusion, is observed. These pores are distinguished by their non-spherical morphology, their elongated and irregular shape and their significantly larger size (>100–150 μm) than keyhole-type pores. They are therefore much more critical from the point of view of their effect on the mechanical

properties, which is why it is necessary to optimize the process parameters to minimize their occurrence.

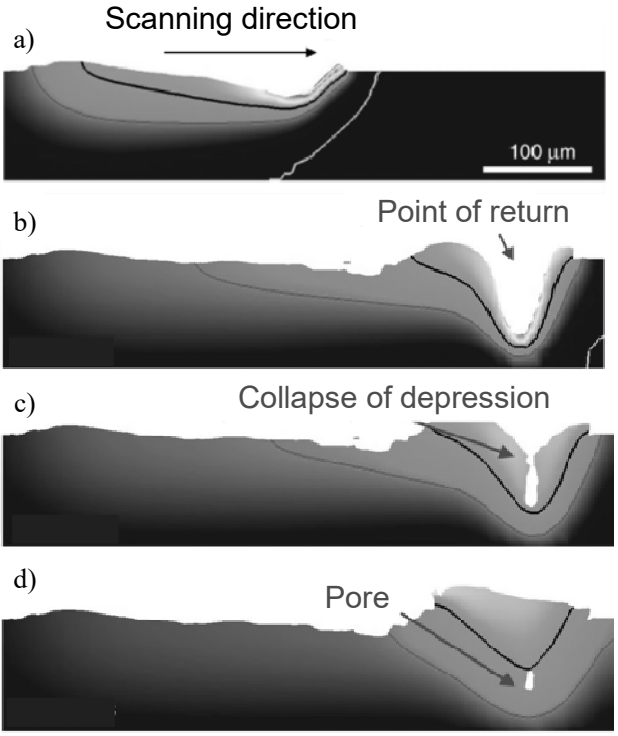

Figure 1.38. *Schematic representation of the formation of a keyhole-type pore (adapted from Martin et al. 2019). For a color version of this figure, see www.iste.co.uk/peyre/alloys2.zip*

Global energy per volume manufactured ($= \frac{P_0}{e_V.\Delta Z_{powder}.V_0}$), where P_0 is the power delivered by the laser beam, V_0 is the scanning speed, e_V is the distance between two adjacent laser lines and ΔZ_{powder} is the thickness of the powder layer, is the easiest energy variable to use and the most widely used (Kasperovitch et al. 2016; Cunningham et al. 2017; Han et al. 2017) to characterize the presence of keyhole type pores or lack of fusion. This volumetric energy density E_V^g has been widely used to determine parameter windows (P_0,V_0, ΔZ_{powder}, e_V) to minimize porosity when manufacturing Ti-6Al-4V parts with the L-PBF process. Various intervals of volumetric energy density E_V^g reaching a relative density greater than 99.9% are

reported in the literature: 83–120 J/mm^3 (Kasperovitch et al. 2016), 49–194 J/mm^3 (Cunningham et al. 2017) and 120–202 J/mm^3 (Han et al. 2017).

Although easy to use, the volumetric energy density E_V^g does not make it possible to predict with certainty the presence or absence of defects within the material. The literature reveals that for values of the parameters (P_0,V_0, ΔZ_{powder}, e_V) significantly different but leading to identical E_V^g values, the porosity rate can vary significantly (Shipley et al. 2018).

The normalized enthalpy is the ratio between the volumic enthalpy delivered by the laser, ΔH and the volumic enthalpy of fusion, ΔH_F : $\frac{\Delta H}{\Delta H_F} = \frac{A.P_0}{\rho(C_p.\Delta T+L_F)\sqrt{\pi.(\frac{D_0}{2})^3.V_0.a_{th}}}$, where A is the absorptivity, ρ is the density, C_p is the mass-specific heat, ΔT is the difference between the melting temperature T_F and the initial build plate temperature T_0, L_F is the latent heat of fusion, $D_0/2$ is the radius of the laser beam and a_{th} is the thermal diffusivity of the material.

This normalized enthalpy is a variable more suitable for predicting the melting mode and the type of associated defects, independently of the material (King et al. 2014). It translates perfectly well the dimensionless depth of the fusion zonel defined by H_{FZ}/D_0 where H_{FZ} is the height of the melt-pool (Hann et al. 2011; Scipioni Bertoli et al. 2017).

1.4.3.2. *Origin of the microstructure*

During the fabrication of Ti-6Al-4V parts by L-PBF, a columnar microstructure characteristic of AM processes is generated (Thijs et al. 2010; Vilaro et al. 2011; Simonelli et al. 2012). The material contains parent β grains, elongated in the construction direction, up to several millimeters long and 100–150 μm wide (Thijs et al. 2010) (Figure 1.39).

Such a microstructure results from the fact that during solidification in the β domain, the direction of growth of the β grains is parallel to the thermal gradient, itself perpendicular to the solidification front of the melt-pool. Due to the very elongated shape of the melt-pool during the L-PBF process, the heat flow is preferentially in the vertical direction toward the lower layers of the material and toward the build plate (DebRoy et al. 2018). The growth of the β grains proceeds as follows: when the laser beam scans the layer of powder, the top of the columnar grains formed during the manufacture of the previous layer is remelted over several layers. Solidification then takes place by epitaxy, generating highly textured columnar β grains (Vilaro et al. 2011). Parent β grains show a {100} texture along grain growth direction (Simonelli et al. 2012).

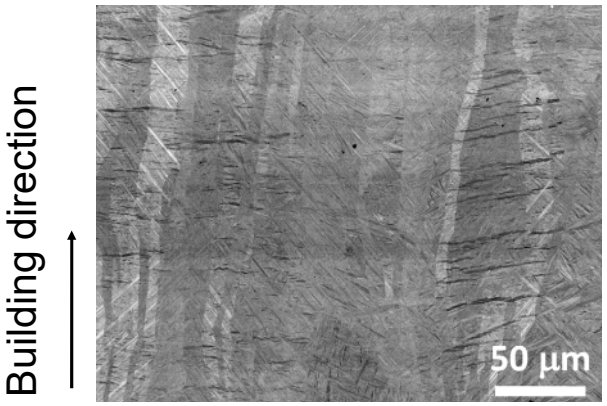

Figure 1.39. *SEM micrograph of a sample of Ti-6Al-4V produced by L-PBF (adapted from Xu et al. 2015)*

The direction and morphology of β grains can be affected by the scanning strategy, as demonstrated by Thijs et al. (2010). A unidirectional ("one way") strategy generates grains tilted by 19° with respect to the vertical (Figure 1.40) while a "zigzag or round trip" strategy produces grains aligned with the manufacturing direction (Figure 1.39). It therefore appears that the scanning strategy is an interesting tool to control the orientation of the parent β grains and the associated texture. Grain orientation is also influenced by scanning speed and part geometry (Thijs et al. 2010).

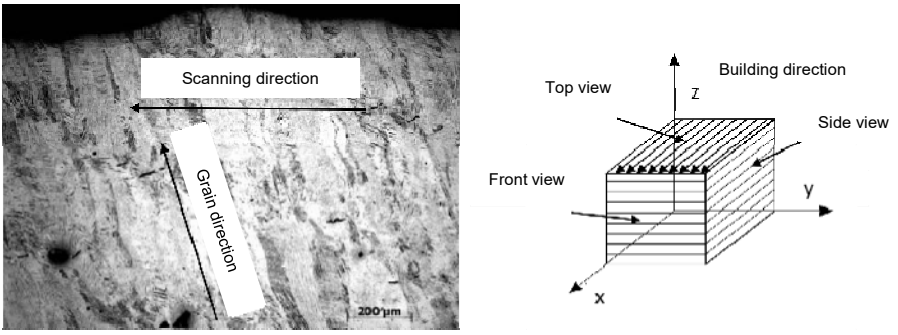

Figure 1.40. *Optical micrograph of a sample of Ti-6Al-4V fabricated by L-PBF with a unidirectional scanning (adapted from Thijs et al. 2010)*

In the case of the L-PBF process, the very rapid cooling (between 10^3 and 10^8 K/s; Shipley et al. 2018) of phase β below temperature M_s results in a martensitic transformation β → α'. The acicular morphology of this martensite is hierarchical, as illustrated in Figure 1.41. Primary martensite needles a few micrometers wide and several tens of micrometers long extend right through the parent β grains. Numerous needles of secondary martensite, about 10 µm long and a few hundred nanometers wide, oriented parallel or perpendicular to the primary martensite, are also visible. On a finer scale, tertiary and quaternary martensite are present between the needles of secondary martensite (Yang et al. 2016).

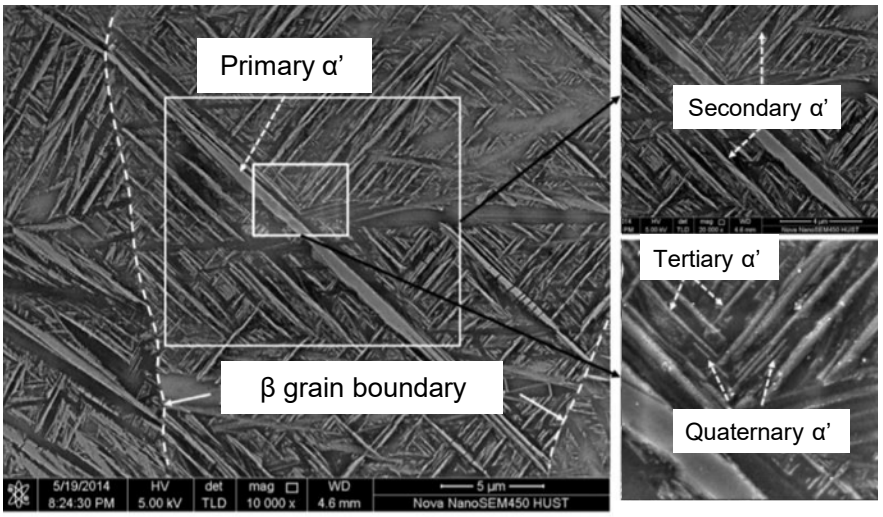

Figure 1.41. *SEM micrographs of the martensitic microstructure within a sample of Ti-6Al-4V produced by L-PBF (Yang et al. 2016)*

The formation mechanism of this hierarchical microstructure is directly related to the cyclic nature of the thermal history undergone by Ti-6Al-4V during the L-PBF process. As depicted in Figure 1.42, primary and secondary martensite needles form during early cooling cycles, while tertiary and quaternary martensites appear during later cycles, during which peak temperatures and cooling rates are lower (Yang et al. 2016).

The process parameters as well as the scanning strategy have a great influence on the thermal history of the material, on the cooling rate and, consequently, on the martensitic transformation. The hatch vector and the scanning speed both impact the morphology and the size of the martensite lamellae (Yang et al. 2016). For a range

of given parameters $(P_0, V_0, \Delta Z_{powder}, e_V)$, the geometry of the part also plays a decisive role, as demonstrated by Hocine et al. (2020). In the case where the laser beam scans a small section (for example, a 2 mm^2 side; Figure 1.43(a)), the frequent round trips of the laser beam keep a given point on the surface at a high temperature, higher than the transus for a long time. The subsequent cooling is then relatively slow. On the other hand, in the case of a wider section such as that represented in Figure 1.43(c), the greater distance traveled by the laser beam allows the material to cool below the transus between each round trip. As the cooling rate is thus increased, a much finer martensitic microstructure is then generated.

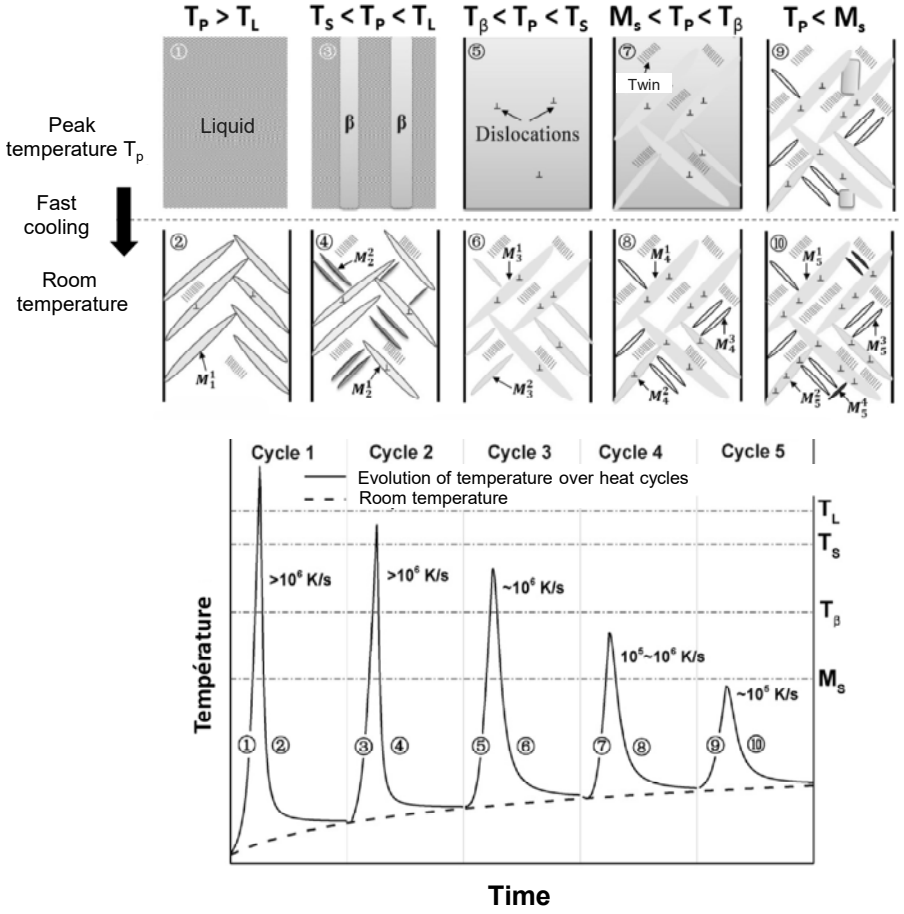

Figure 1.42. *Schematic representation of the formation mechanism of the hierarchical martensitic microstructure within Ti-6Al-4V (Yang et al. 2016). For a color version of this figure, see www.iste.co.uk/peyre/alloys2.zip*

Although the microstructure obtained by L-PBF is almost always martensitic in nature, some authors have demonstrated the possibility of decomposing this microstructure in situ (Xu et al. 2015, 2017). They thus obtained an ultrafine α + β type microstructure by optimizing the process parameters, in particular the defocusing of the laser beam, the layer thickness and the time lapse separating the deposition of two successive powder layers. The diffusion-controlled decomposition of martensite is favored by an increase in the holding time at an elevated temperature (Xu et al. 2017). Aspects such as the dimensions of the part and the contact area with the construction supports also play a major role.

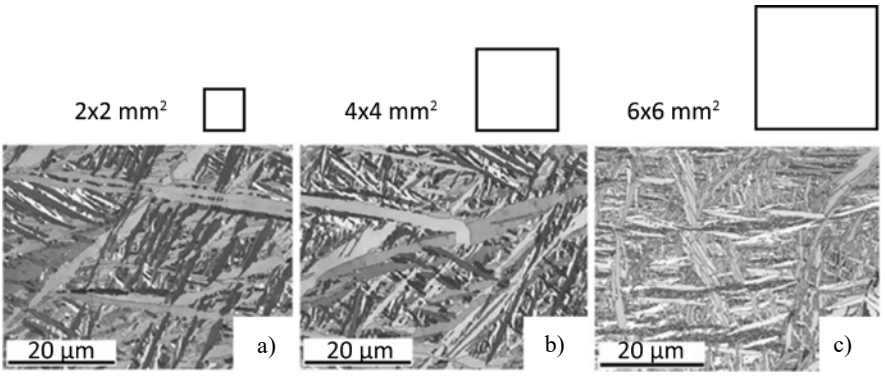

Figure 1.43. *Influence of scan length on the microstructure (IPF maps) of Ti-6Al-4V formed by L-PBF process (Hocine et al. 2020). For a color version of this figure, see www.iste.co.uk/peyre/alloys2.zip*

1.4.4. *Microstructures of titanium alloys from the E-PBF process*

Compared to L-PBF technology, E-PBF technology has several specificities which have a fairly significant impact on the microstructures in the case of titanium alloys (in particular Ti-6Al-4V) and, to a lesser extent, on the defects resulting from manufacture. The first specificity lies in the fact that it takes place in a hot chamber through the implementation of a so-called preheating temperature ensuring consolidation of the powders, thus making it possible to evacuate the electric charges. This has several consequences, namely lower cooling rates than in the case of laser processes and maintaining the temperature of the solidified zones during construction, which impacts the amplitude of the thermal gradients. In the case of Ti-6Al-4V, the required preheating temperature is most often between 600°C and 700°C. The second specificity of E-PBF lies in the fact that the work is carried out in a

vacuum, which, in the case of titanium alloys, known for their strong affinity for oxygen, can have beneficial consequences, but it may also lead to a loss of aluminum through vaporization. What is more, the vacuum makes it possible to limit the cooling rate of the melt-pool compared to L-PBF process, which is the powder bed process that generates the largest level of residual stresses.

1.4.4.1. *Microstructures*

As in the case of L-PBF, the microstructures of Ti-6Al-4V obtained by E-PBF differ quite significantly from those encountered on forged products. Indeed, they first develop a columnar morphology due to growth by epitaxy of the primary β grains during the L → β solidification, then the precipitation of the α phase via the β → α transformation to the state solid on cooling.

In the case of L-PBF, due to the particularly fast cooling rates, the α' martensitic phase develops preferentially, while in the case of E-PBF, due to much lower cooling rates and to preheating, an α (+ β residual) structure is usually obtained. The diagram in Figure 1.44(a) summarizes the thermal path followed during E-PBF manufacture. The result is a two-phase α + β microstructure with two α-phase morphologies depending on whether it is at the grain boundary (bordered with intergranular α, noted α_{GB}) or in grains with a slatted morphology ($\alpha_{slatted}$) (see Figure 1.44(b)). The primary grains of the β phase are difficult to discern. It is however possible to go back to their morphology and their crystallographic texture from reconstructions based on the orientation relationship that links the α and β phases (the so-called Burgers orientation relationship: <111> direction of the β phase parallel to the <1120> direction of the α phase, and the {110} plane of the β phase parallel to the {0001} plane of the α phase) (see Figure 1.45). It should be emphasized here that the β → α phase transformation makes the microstructure isotropic while that inherited from the solidification obtained by reconstruction shows a certain level of anisotropy (see the comparison between Figures 1.45(a–c) and 1.45(b–d)). It should be noted that the α' phase can nevertheless be detected in the last layer built insofar as the latter does not undergo remelting or preheating for an amount of time sufficient to allow the martensite to decompose via the α' → α + β transformation.

Working in a hot chamber leads to microstructures that are generally less fine than those produced by L-PBF, but consequently with a lower level of residual stresses. The reduction of the residual stresses thus means it is not necessary to carry out a post-HT. Thicknesses of intragranular slats close to 1 μm are most often obtained, even if they nevertheless depend to a certain extent on the manufacturing conditions adopted.

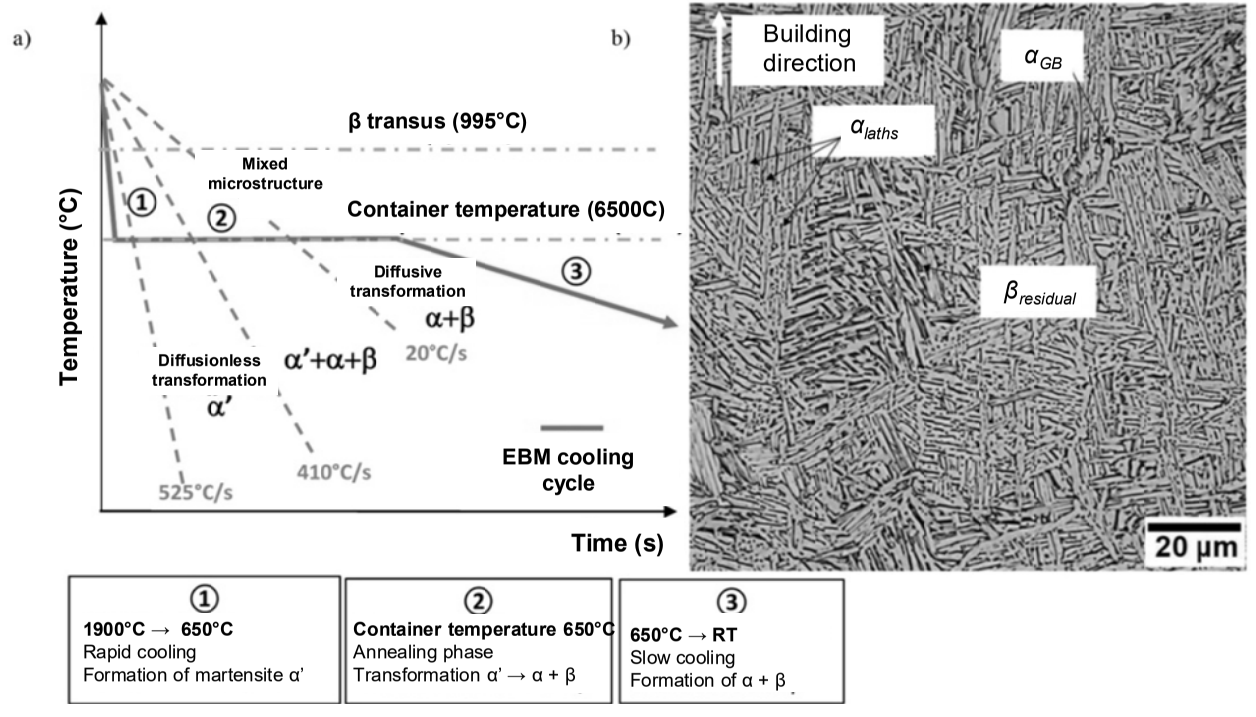

Figure 1.44. *(a) Typical cooling path explaining the α + β two-phase microstructure of Ti-6Al-4V formed in E-PBF. Critical cooling rates are also indicated. (b) Optical micrograph taken in the plane containing the manufacturing direction, illustrating the presence of inter- and intragranular α phase (slats) of grains and fine edges of residual β trapped between the α phase slats (Galarraga et al. 2017). For a color version of this figure, see www.iste.co.uk/peyre/alloys2.zip*

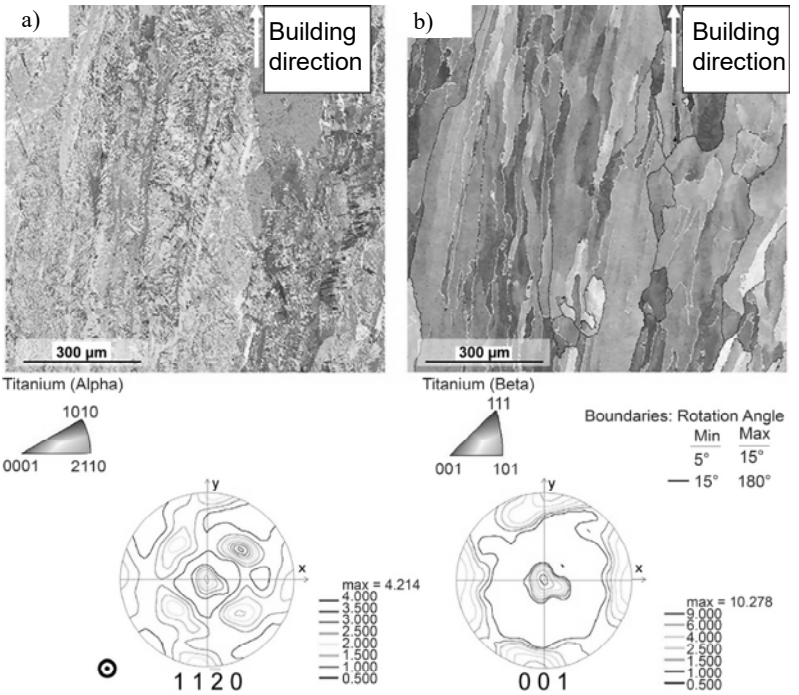

Figure 1.45. *(a) EBSD mapping of a Ti-6Al-4V microstructure manufactured by EBM and (b) reconstruction of β primary grains from the Burgers orientation relationship. The manufacturing direction is vertical. (c) Pole figure (1120) of α phase. (d) Pole figure (001) of the β phase. Illustrations from de Formanoir et al. (2016). For a color version of this figure, see www.iste.co.uk/peyre/alloys2.zip*

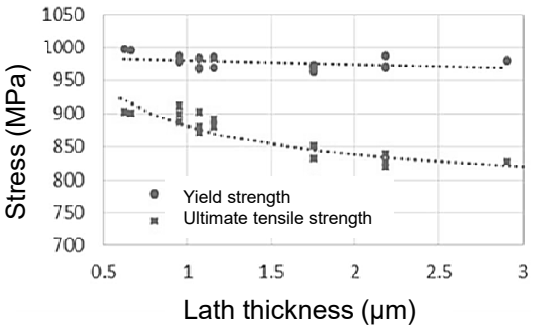

Figure 1.46. *Sensitivity of yield strength and maximum tensile stress as a function of the average thickness of the intragranular α slats; illustration taken from Galarraga et al. (2017). For a color version of this figure, see www.iste.co.uk/peyre/alloys2.zip*

E-PBF microstructures, in their raw state, generally result in lower yield strengths than those measured for microstructures obtained directly by L-PBF, but with larger ductility figures (Figure 1.46).

1.4.4.2. *Defects*

With the production conditions of Ti-6Al-4V by E-PBF being quite optimized today, the microstructures produced generally present a very low level of residual defects, mainly residual porosities of the occluded gas type resulting from the atomization of powders. Porosity rates well below 0.1% can thus be measured conventionally. It should be emphasized that such rates may nevertheless require the implementation of HTs, such as HIP, to meet certain requirements, particularly in terms of fatigue resistance. Due to the specific nature of the electron beam/material interaction, the sensitivity to the formation of keyhole-type defects is also less in the case of E-PBF, because the electrons have a much higher penetrating power than the photons of a laser beam (see section 3.2 of Volume 1). In the same register, the consolidation of the powder bed during preheating also has the advantage of limiting ejections such as "spatters" resulting from the interaction of the electron beam with the powder bed. These ejection phenomena are extensively studied in L-PBF because certain ejections can fall on the locally fused zones and become trapped in the parts, which can lead to a reduction in the mechanical properties.

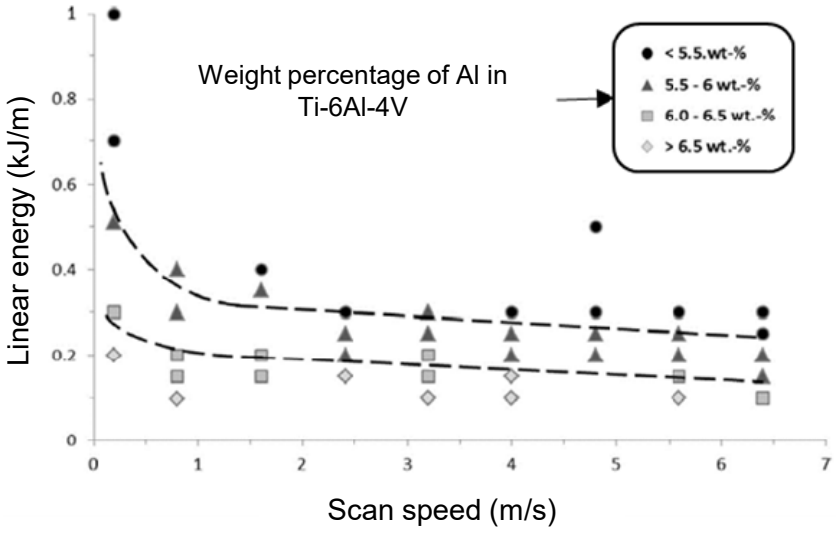

Figure 1.47. *Variation in the mass aluminum content of Ti-6Al-4V depending on the manufacturing conditions; illustration taken from Juetcher et al. (2014)*

Another point to highlight is the possible modification of the alloy composition during construction. Even if the E-PBF manufacture takes place in a hot chamber, working under a vacuum limits the contamination of the titanium alloys by oxygen during the process. On the other hand, this can be more problematic for volatile elements present in the alloy and in particular aluminum. Such an evaporation of aluminum has already been observed in the case of Ti-6Al-4V, its extent depending on the operating conditions (Figure 1.47), but this is particularly significant in the case of intermetallic grades of the TiAl type because a slight modification of the Al content modifies the solidification path and in particular the type of primary phase. In the latter case, it may then be necessary to anticipate this phenomenon by deliberately increasing the aluminum content in the powder if one wishes to remain within the target composition ranges after manufacturing.

1.4.5. *Overview of the microstructures of titanium alloys*

The main objective of this section was to identify the main microstructural differences in the Ti-6Al-4V alloy, following its elaboration in three distinct additive processes (LMD, L-PBF and E-PBF). Each of these processes is distinguished by very different melt-pool formation and solidification kinetics, but also by different melt-pool surface volumes and temperatures. The advantage of having chosen such an alloy is its ability to form several metastable phases (in particular α') depending on the speed and quenching temperature and whose return to equilibrium ($\alpha' \rightarrow \alpha + \beta$) is fairly rapid depending on the phase transformation paths, which vary according to the thermal history of a given layer.

It should be noted that in LMD, it is easy to switch from a columnar structure to an equiaxed structure by varying only the process parameters, unlike the L-PBF process. This is why other routes beside the so-called first-order process parameters (see Chapter 1 of Volume 1) are chosen to modify the morphology and size of the parent grains, but also their crystallographic texture. Among those that are still under-explored in the literature are scanning strategies, beam shaping, laser defocusing, the addition of germinating agents to the powder, etc. Being able to control the CET makes it possible to design parts with zones with different grain structures and different mechanical behaviors; in this case, it is necessary that the post-treatments do not cause recrystallization (see Chapter 2).

Furthermore, it has been shown that in the raw state of solidification, the LMD process makes it possible to generate a ($\alpha' + \alpha + \beta$) phase gradient between the top (completely α') and the bottom (mostly α) of the part and the proportions of each of these phases vary according to the distance from the build plate. However, the repeatability of such a phase gradient requires in situ control of the part's overall

thermal properties. On the other hand, as-manufactured parts in the L-PBF process have a predominantly martensitic microstructure, demonstrating that the successive annealings generated by the incremental construction are inefficient for a full annealing with T_0 temperature lower than the α' phase decomposition temperature (>400°C).

With regard to the E-PBF process, the microstructures are closer to those of the LMD process than to those of the L-PBF process. Indeed, electron beam technology is characterized by preheating the powder bed prior to the melting step as well as by a very low partial pressure of oxygen. This has the merit of generating α + β two-phase microstructures close to thermodynamic equilibrium, except at the top of the construction where the microstructure is α' single-phase. Recall that the α + β two-phase microstructure generated by E-PBF has better ductility and does not necessarily always require post-HTs compared to the α' single-phase microstructure generated by L-PBF. On the other hand, the microstructures produced by E-PBF are less fine than those produced by L-PBF, but with the advantage of lower residual stresses. It is this last specificity that has given the E-PBF process its reputation, as it is the first process to have produced uncracked intermetallic TiAl blades, an alloy known for its low toughness and its ductile–brittle transition at around 700°C. Finally, the vacuum is beneficial to limit oxidation of the material, but it can also be a disadvantage because it favors the evaporation of the elements with low vaporization points, such as aluminum in the present case, requiring the composition of the starting powder to be optimized to compensate this effect.

1.5. Microstructures of aluminum alloys

1.5.1. *Microstructures induced by L-PBF*

1.5.1.1. *Origin of porosity*

The porosities in aluminum alloys produced by L-PBF may have different origins, some of which are not specific to aluminum alloys:

– a too large distance between two laser lines (hatch vector) leading to a lack of local melting of the powder (Aboulkhair et al. 2014);

– instabilities linked to the interaction between a too linear energy laser beam and the melt-pool can lead to so-called keyhole defects (vapor capillary) (Thijs et al. 2013), related to the vaporization of the metal under the laser beam;

Section 1.5 written by Aude SIMAR, Olivier PONCELET, Éloïse EIMER and Christophe DESRAYAUD.

– a too low linear energy level, leading to so-called Plateau–Rayleigh hydrodynamic instability causing "balling", appears as a result of the minimization of the surface energy of the melt-pool (Yu et al. 2016);

– oxides can be integrated into the weld pool and prevent the wetting by the new layer on the previous layers (Thijs et al. 2013);

– porosities can come from the powder and in particular from the gas trapped in the powder particles during its atomization with argon (Aboulkhair *et al.* 2014);

– porosities due to the greater solubility of hydrogen in liquid aluminum compared to the solid state (Vilaro 2011; Delroisse et al. 2017).

1.5.1.2. *Al-Si casting alloys*

The most common aluminum alloys used for L-PBF AM are the Al-Si casting grades (4xxx series), and in particular the AlSi10 Mg and AlSi12 alloys, because the eutectic of the Al- Si binary-system is at 12.8 mass % Si. These alloys are therefore less prone to hot cracking.

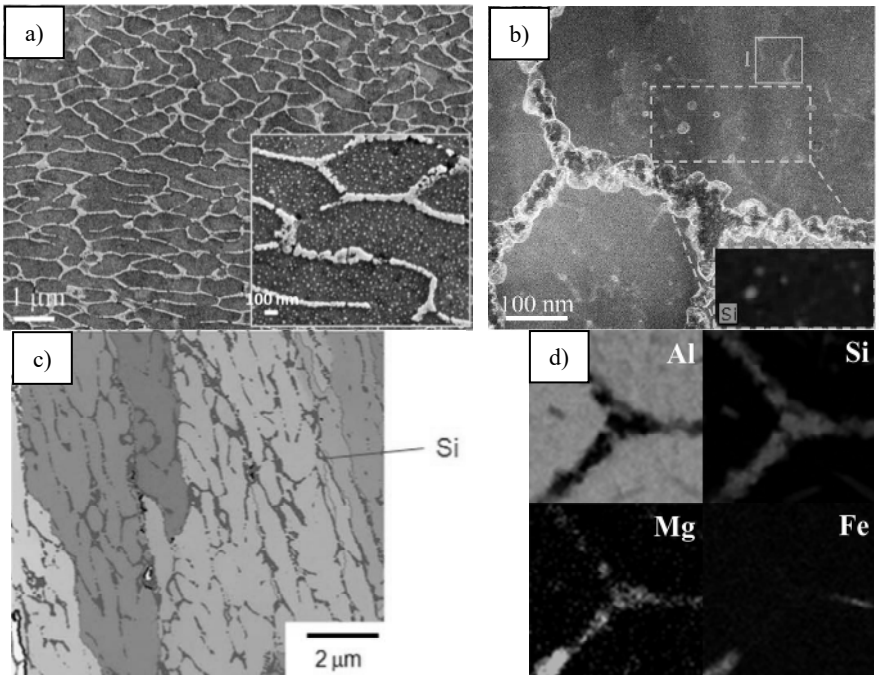

Figure 1.48. *Cellular microstructure of the AlSi10Mg alloy produced by L-PBF. For a color version of this figure, see www.iste.co.uk/peyre/alloys2.zip*

COMMENTS ON FIGURE 1.48.– *Microstructure observed by (a) SEM and (b) TEM (HAADF-STEM), and the integrated figure shows the presence of Si-rich precipitates through EDX mapping (Zhao et al. 2019). (c) Overlay of an EBSD crystallographic orientation map and a chemical Si-rich zone (EDX, in green) map showing the distribution of the Si-rich phase at the grain core and at its boundary (Takata et al. 2017). (d) Magnesium segregation in the Si-rich eutectic zone (Zhou et al. 2018).*

The microstructure of Al-Si alloys is generally cellular (Figure 1.48(a)) due to the high cooling rate and high thermal gradient upon solidification during the L-PBF process. The high cooling rate also favors the trapping of Si during solidification due to the undercooling of the liquid in front of the solid–liquid interface. This leads to an oversaturation of Si in the aluminum matrix, at the heart of the α-Al cell. The thermodynamic equilibrium concentration in the Si-rich eutectic (predicted by the CALPHAD method) is not reached in an AlSi10Mg produced by L-PBF just after manufacturing (Takata et al. 2017), confirming that the missing Si must be found at the heart of the α-Al cell (Liu et al. 2019). Furthermore, the Si fraction in the cell boundary phase is higher than in the equilibrium eutectic composition (Liu et al. 2019); thus it is called the "pseudo-eutectic" phase. Moreover, this supersaturation can lead to the precipitation of very fine Si-rich precipitates at the heart of the cell (Wu et al. 2016; Zhou et al. 2018; Santos Macías et al. 2019; Zhao et al. 2019) (Figure 1.48(b)).

A grain contains a large number of cells (Wu et al. 2016; Chen et al. 2017; Takata et al. 2017), as shown in Figure 1.48(c). In order to ensure epitaxial growth through the pseudo-eutectic phase, Chen et al. (2017) state that epitaxy must take place between the core of the cell (α-Al phase) and the Al-rich phase present in the pseudo-eutectic phase. The cells are elongated in the direction of grain growth, according to the thermal gradient (Wu et al. 2016), as highlighted by Figure 1.48(c).

The magnesium present in the AlSi10Mg alloy essentially segregates at the cell boundaries during solidification (Li et al. 2017; Zhou et al. 2018) (Figure 1.48(d)). Some authors (Aboulkhair et al. 2014) have highlighted the evaporation of the Mg initially present in the powder, attributed to its vapor pressure.

The cellular microstructure of the AlSi10Mg alloy made by L-PBF varies at the melt-pool boundaries. Three different zones can be observed (Thijs et al. 2013; Wu et al. 2016; Liu et al. 2019) (Figure 1.49):

– *zone 1* at the center of the weld pool, with a relatively fine microstructure and a cell size typically around 500 nm;

– *zone 2* at the edge of the melt-pool, with a slightly coarser microstructure and a cell size between 700 nm to a few micrometers (zone 2 in Figure 1.49);

– *zone 3* at the extreme edge of the melt-pool, called the HAZ, where the silicon-rich cell boundary are globularized and become discontinuous.

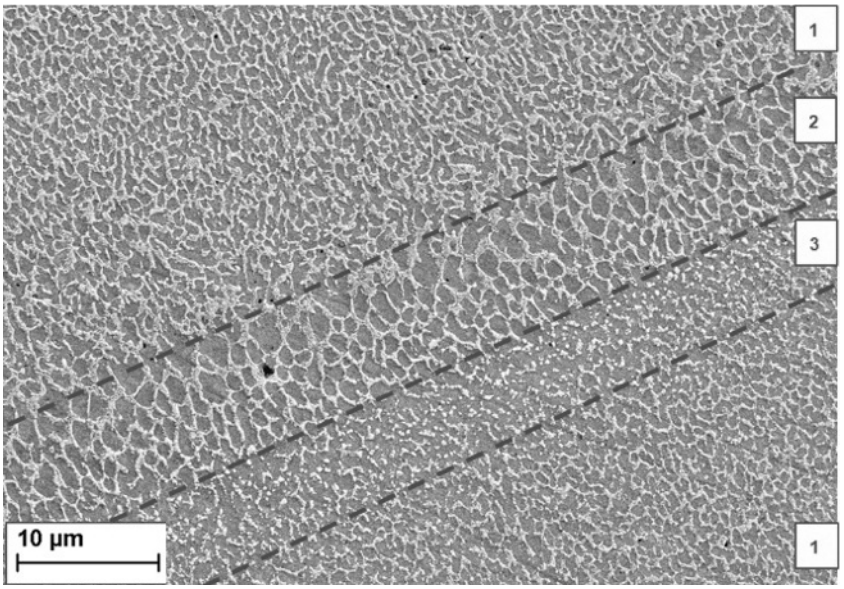

Figure 1.49. *Microstructure heterogeneity in an AlSi10Mg alloy produced by L-PBF. The three zones at the boundary of a melt-pool are (1) the fine microstructure melt-pool, (2) the coarse microstructure melt-pool and (3) the heat-affected zone. For a color version of this figure, see www.iste.co.uk/peyre/alloys2.zip*

Liu et al. (2019) discuss the formation of the coarse zone at the boundary of the melt-pool (zone 2). They associate this zone with the partly solid–liquid zone of the melt-pool (also called mushy zone), that is to say the zone where the temperature reached is between the solidus and the liquidus of the alloy and therefore corresponds to the partial remelting of an area already melted and solidified. The HAZ (zone 3) corresponds to the HT undergone by the unremelted layer.

The size of the three different areas of the melt-pool depends on the manufacturing parameters. Figure 1.50 shows the decrease in the width of zone 2 with increasing of scanning speed, the latter inducing a faster cooling rate.

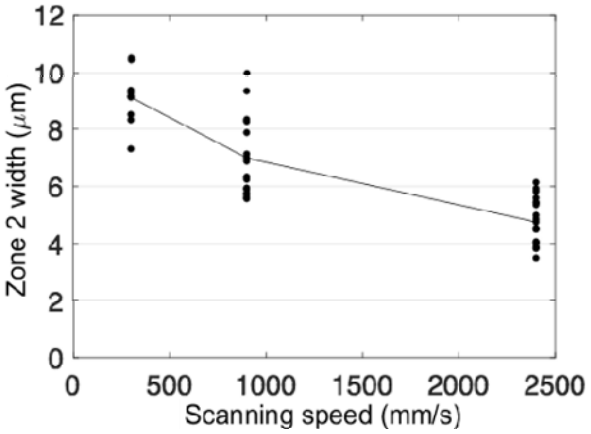

Figure 1.50. *Evolution of the width of zone 2 for the AlSi10Mg alloy as a function of the scanning speed for a laser power of 232 W*

The higher the cooling rate, the finer the cell structure. However, the scanning speed necessary to manufacture the contours of a part must be lower (with, therefore, a lower cooling rate) than that necessary to fill the core in order to optimize the surface roughness of the part. The direct consequence is a different microstructure between the contours and the core (Figure 1.51(a)). In the case of Figures 1.51(b) and (c), the cells have a size of around 800 nm for the contour and 300 nm for the core.

Manufacturing parameters are not the only ones that affect the cooling rate; the geometry of the part can also modify it, locally changing the size of the cellular structure (Delroisse et al. 2017). The cellular structure is finer in the upper part of a L-PBF construction than in the lower part. Indeed, the lower part serves as a heat sink for the upper part, promoting a faster cooling rate. The upper part then becomes harder than the lower part.

Directional solidification during the L-PBF process leads to a morphological and crystallographic texture. The grains grow toward the center of the melt-pool. Epitaxial growth only occurs at the bottom of the melt-pool and leads to elongated grains in the building direction of the part with texture <001> relative to the building direction of the part (Thijs et al. 2013; Takata et al. 2017; Liu et al. 2019) (Figure 1.52). On the sides of the melt-pool, a large number of grains nucleate and lead to an equiaxed grain structure (Takata et al. 2017) (Figure 1.52). The upper surface of the melt-pool also shows the nucleation of small equiaxed gains. However, these are remelted by the next layer and can therefore only be observed on the upper surface of the part (Thijs et al. 2013).

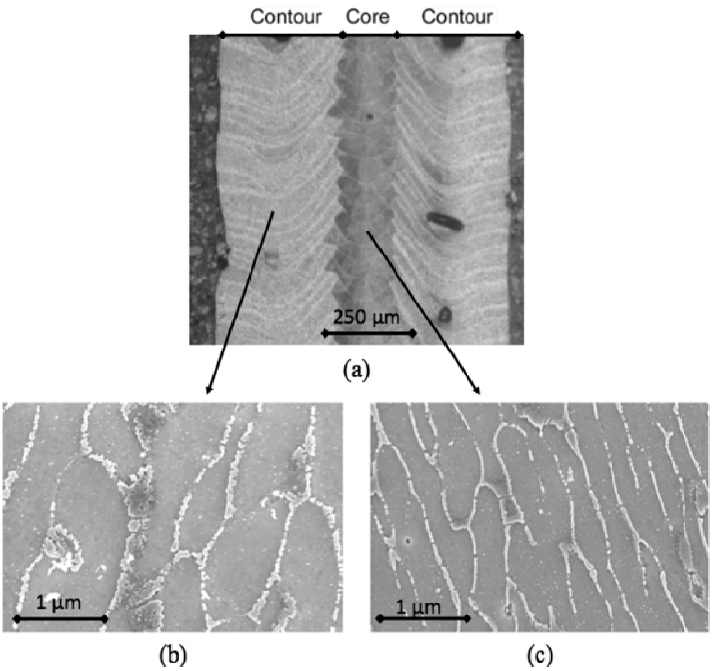

Figure 1.51. *(a) Optical microscopy of a thin wall fabricated by L-PBF. (b) Zoom using SEM imaging on the microstructure of the contour and (c) of the core (core parameters: 1,200 mm/s at 232 W; contour parameters: 300 mm/s at 273 W)*

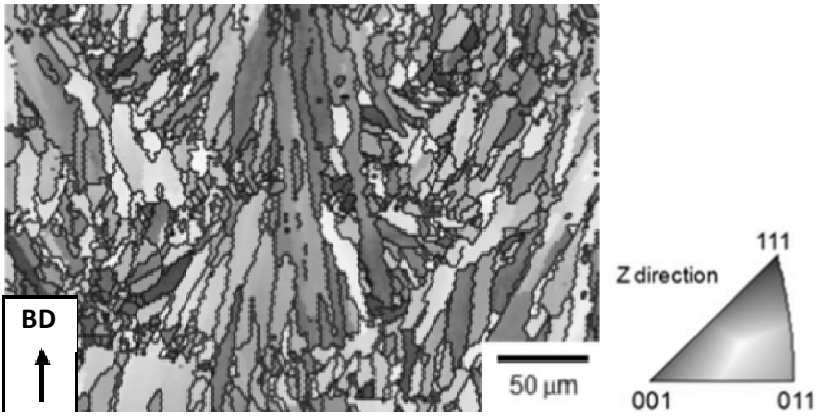

Figure 1.52. *EBSD image of the granular structure in a melt-pool (BD = building direction) (according to Takata et al. 2017). For a color version of this figure, see www.iste.co.uk/peyre/alloys2.zip*

HTs or hot isostatic pressing (see Chapter 2) have been proposed in the literature with the aim of homogenizing the microstructure (Delroisse et al. 2017) and improving the ductility of the alloy. Generally, high temperature treatments lead to a globularization of silicon precipitates (Takata et al. 2017; Zhou et al. 2018) and consequently to a significant drop in the rupture strength of the alloy but to the benefit of its ductility (Delroisse et al. 2017; Zhao et al. 2019). On the other hand, all these treatments have a minor effect on the granular structure, in terms of size and texture. An artificial aging (or tempering) treatment at low temperature (for example: 160°C and 10 h) makes it possible to harden the material again after it has been solutionized at temperatures above 500°C with the subsequent precipitation of hardening β" phases of less than 10 nm and GP zones of 2–3 nm (Zhou et al. 2018).

1.5.1.3. *High-strength aluminum alloys*

High-strength aluminum alloys, such as 2xxx (Al-Cu), 5xxx (Al-Mg), 6xxx (Al-Mg-Si) and 7xxx (Al-Zn-Mg) series alloys, are attractive for high-added-value applications, such as automotive, space and aeronautics applications. They have higher mechanical strength than Al-Si alloys (4xxx series), commonly used for AM, but are subject to hot cracking. Appropriate strategies must be set to produce dense and crack-free alloys. For example, Al-Cu-Mg alloys (Zhang et al. 2017b) can be produced by L-PBF without cracking using a low scan rate, less than 8 m/min or 133 mm/s (Figure 1.53).

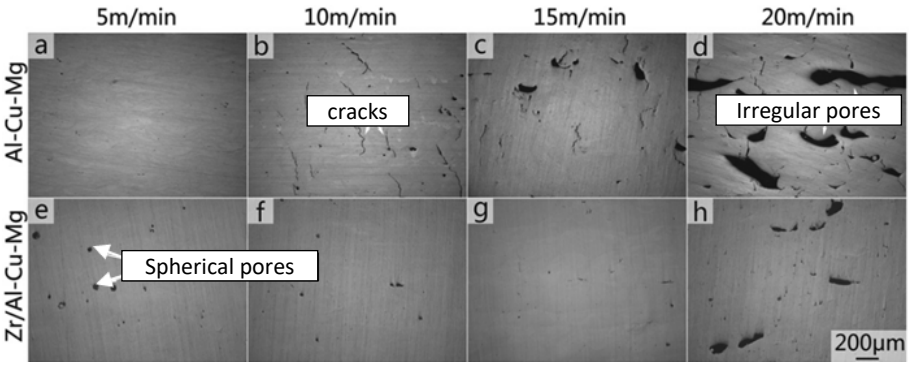

Figure 1.53. *Porosity and cracks as a function of scanning speed in an Al-Cu-Mg alloy compared to Zr/Al-Cu-Mg (Zhang et al. 2017b). Zr is a strong grain refiner*

To avoid hot cracking, a commonly applied strategy for 7xxx series alloys is to add Si to the alloy to reduce the solidification gap and promote its fluidity (Montero-Sistiaga et al. 2016) or to add AlSi10Mg powder by mixing (Casati et al. 2019). The microstructure formed resembles the cellular microstructure of Si-rich

aluminum alloys such as the AlSi10Mg alloy with the Si-rich phase at the edge of the cells. θ(Al_2Cu) and Q(AlCuMgSi) phases can also be formed (Casati et al. 2019).

The second strategy to avoid hot cracking of 2xxx, 5xxx, 6xxx and 7xxx alloys is the use of grain refiners, such as TiB_2 for a 6061 alloy (Carluccio et al. 2018); Zr for Al-Cu-Mg, 7075 and 6061 (Martin et al. 2017; Zhang et al. 2017b; Lei et al. 2019) (Figure 1.53); Sc for the 7075 alloy (Lei et al. 2019); and Sc and Zr for 5xxx alloys, including Scalmalloy®, developed by an Airbus subsidiary (Spierings et al. 2017).

These additions lead to the respective formation of Al_3Ti precipitates in a thin layer on the TiB_2, Al_3Zr, Al_3Sc and $Al_3(Sc_x, Zr_{1-x})$. These precipitates are unusual in that they have a crystalline lattice compatible with aluminum, favoring the nucleation of numerous fine and equiaxed grains. Furthermore when adding Sc to a hypereutectic alloy, a bimodal microstructure is obtained with alternating fine and equiaxed grain zones at the edge of the melt-pool, following the hypereutectic precipitation of Al_3Sc nanoparticles, and Sc-supersaturated columnar coarse-grained zones, following rapid cooling (Spierings et al. 2017). When adding grain refiners, it is important to have a good distribution of these in the melt-pool, which can be favored by a uniform electrostatic deposit on the particles of the powder (Martin et al. 2017).

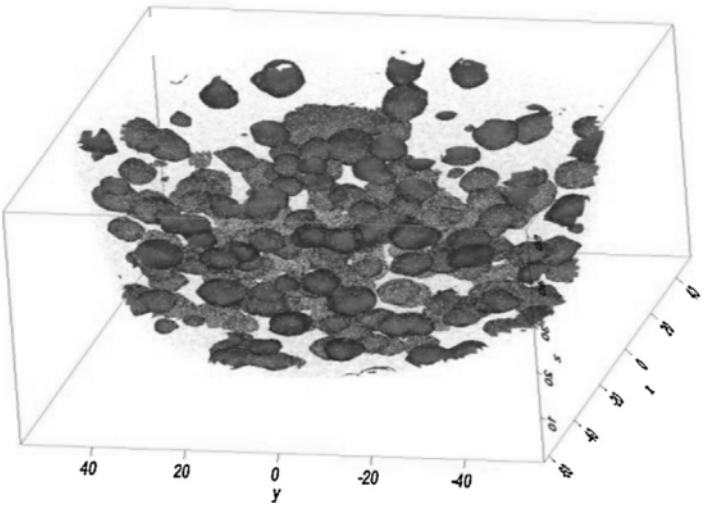

Figure 1.54. *Three-dimensional reconstruction of Al_3Sc nano-precipitation in an Al-Mg-Sc-Zr alloy obtained by L-PBF and followed by heat treatment at 325°C for 4 h (observation by atom probe tomography) (Spierings et al. 2018). For a color version of this figure, see www.iste.co.uk/peyre/alloys2.zip*

In these new alloys, another problem is the loss of alloying elements, notably Mg and Zn, due to their evaporation under the laser beam. This leads to a softening of the alloy compared to the wrought alloy with the composition of initial powder (Montero-Sistiaga et al. 2016; Martin et al. 2017).

The 2xxx, 6xxx and 7xxx series alloys are known for their age-hardening potential (see section 2.3.3). Thus, during a post-LPBF-fabrication T6 HT, it is possible to harden the alloy, leading to nano-precipitation. Spierings et al. (2018) observed the formation of a large density of Al_3Sc nano-precipitates in an Al-Mg-Sc-Zr alloy, as observed in Figure 1.54 using atom probe tomography.

1.5.2. *Microstructures induced by WAAM on aluminum*

1.5.2.1. *Effect of the deposition process and the quality of the filler wire on the microstructure and the level of porosity*

The solidification rates during the WAAM process are considerably slower than the solidification rates of laser or electron beam processes. This difference has a dramatic effect on the microstructure and compound distribution of an aluminum alloy deposited by the WAAM process. In the case of alloy 2319 (Al-6wt.% Cu), widely used with this process, significant eutectic microsegregations ($L \rightarrow \Theta\text{-}Al_2Cu + \alpha\text{-}Al$) have been observed in samples processed by cold metal transfer (CMT) (Gu et al. 2016b) and gas transfer arc (GTA) process (Bai et al. 2015).

The microsegregation of alloying elements also takes place during the deposition of other compositions. Two separate studies on the deposition of AlCuMg alloy with several filler wires have shown that these microsegregations are difficult to avoid and that they can be the cause of cracks for certain chemical compositions (Gu et al. 2018; Qi et al. 2018a).

The size and morphology of the grains largely depend on the deposition process and parameters. For example, Cong et al. have shown that for CMT processes, the nature of the current and the voltage used, that is, whether the process is alternating current or not and whether the short circuit phases are alternated with pulse waves, have an effect on the formation of columnar or equiaxed grains, as well as on the size of the grains (Cong et al. 2014).

The level of porosity depends mainly on the process, the deposition parameters and the quality of the filler wire. Regarding the deposition process, Cong et al. (2014) showed that the CMT deposition mode influences the level of porosity. In

their study, the authors showed that the "CMT Advanced" welding process considerably reduces the level of porosity compared to other CMT deposition methods.

The effect of filler wire quality has been reported by several authors. Gu et al. highlighted the differences in filler wire quality for alloy 4043 (Gu et al. 2014). The five filler wires used in this study had different surface qualities, microstructure and hardness. These differences led, in some cases, to instability in the electric arc during deposition. Pinter (2017) and Ryan et al. (2018) showed that porosity levels are very dependent on the filler wire. The large majority of the studies published on the WAAM of aluminum are based on MIG processes. For other processes where the filler wire is not one of the electrodes, i.e., tungsten inert gas (TIG) or plasma, the quality of the filler wire is not of prime importance. For example, Pinter demonstrated that the alternative current plasma transfer arc (ACPTA) process was less sensitive to the quality of the filler wire (Pinter 2017).

1.5.2.2. *Interlayer rolling*

The interlayer rolling is a process that consists of deforming the material deposited at each layer by compressing it using a roller or a hammering tool. This process was first developed to reduce the formation of columnar grains during the WAAM of the Ti-6Al-4V alloy (Martina et al. 2013). Using this process for WAAM aluminum has several advantages:

– reduction in grain size (Gu et al. 2016b, 2018). Rolling produces a large number of small grains and greatly reduces the number of larger grains (Figure 1.55);

– modification of the texture: the concentration of sub-grains increases and eventually dominates the structure of the material when the deformation exceeds 30% (Gu et al. 2016b). A texture can also be observed in the direction of deformation (Figure 1.55);

– a reduction in size and an increase in the number of second phases;

– a drastic reduction in the porosity level (Gu et al. 2016a). Hydrogen solubility increases linearly with dislocation concentration (Gu et al. 2016a). During rolling, hydrogen is stored in the dislocations and can also be released outside the material by diffusion along the dislocation networks, reducing porosity.

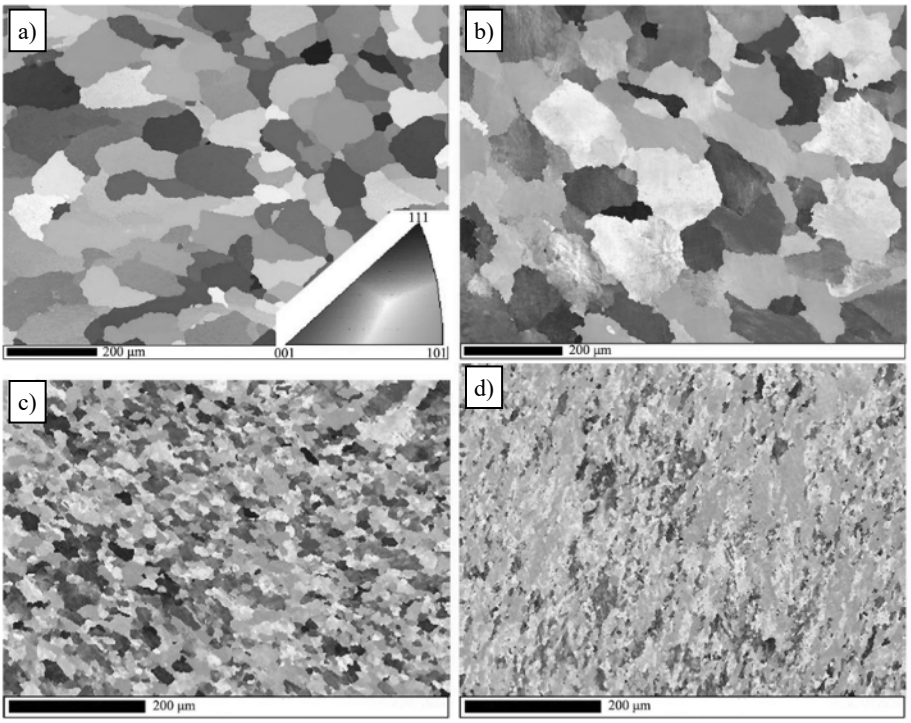

Figure 1.55. *Inverse pole figure (IPF) mappings of the WAAM 5087 alloy under various conditions: (a) as-deposited and (b, c, d) rolled with a load of 15, 30 and 45 kN, respectively (Gu et al. 2018). For a color version of this figure, see www.iste.co.uk/peyre/alloys2.zip*

1.5.2.3. *Effect of heat treatments*

As described above, the slow solidification rate associated with the WAAM process (compared to the L-PBF process) leads to the presence of rather wide segregations of eutectic phases. For alloys with precipitation hardening, it is necessary to dissolve these compounds by HT to increase the mechanical properties of the alloy. Gu et al. (2016b) have shown that solution treatment and tempering (T6) of 2319 alloy allows a large quantity of second phases to be reintroduced into the matrix. Regarding the type of grains, their structure is similar to that obtained during the initial deposit, with the majority of grains in the recrystallized state.

The level of porosity can be affected by HTs. For both 2319 and 5087 alloys, Gu et al. (2016b) showed that the number of pores of all sizes increased during solution treatment, and that the number of large pores increased considerably. The reason for

this change in porosity is known as the Ostwald ripening phenomenon, which describes the formation of large pores from smaller pores, as well as in the accelerated diffusion of hydrogen in the material at high temperature.

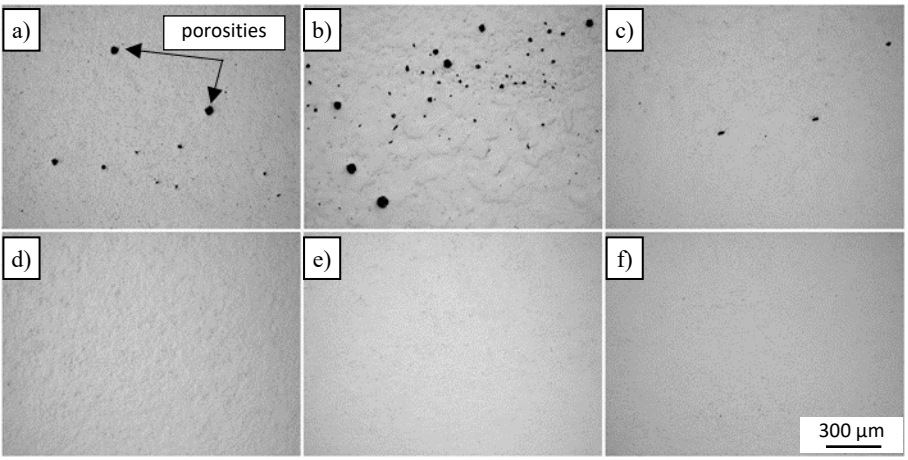

Figure 1.56. *Porosity of the WAAM 2319 alloy observed under an optical microscope under various conditions: (a) as-deposited; (b) heat-treated; (c–e) rolled with a load of 15 kN, 30 kN and 45 kN; and (f) rolled (45 kN) and heat-treated (according to Gu et al. 2016a)*

The use of the interlayer rolling process brings great benefits for the reduction of the porosity level after HT. Gu et al. showed that the 2319 alloy hardened and solution-treated has a significantly lower level of porosity than the non-hardened 2319 material after solution treatment (Gu et al. 2016a). This rolling effect, noticable in Figure 1.56(f) – the rolled and heat-treated condition – shows a considerably lower porosity level than Figure 1.56(b), after HT without rolling.

1.5.3. *Microstructures induced by DED-LMD*

Applied to aluminum alloys, DED processes allow microstructural optimization with larger sizes (a few µm) than for L-PBF processes due to slower cooling rates (Dubourg et al. 2005). Among these processes, LMD is a good candidate but is not necessarily easy to apply to aluminum. Among the parameters to be adjusted specific to aluminum alloys, the incidence angle of the laser beam makes it possible to limit the reflections of the light radiation on the optical system. Similarly, a too small nozzle-to-workpiece distance can cause problems, the particles being heated at

the nozzle outlet by the radiation of the fusion zone, thus obstructing the projection nozzles.

Melting powder in LMD requires high laser source power, given the limited absorbance of aluminum alloys. The deposit typically generates columnar dendritic microstructures (DebRoy et al. 2018). Unlike L-PBF, where the speed of the laser beam is high (greater than 1 m/s), the columnar structures along the [001] direction of the aluminum matrix can be oriented with a deviation angle of 25° (Figure 1.57) with respect to the building direction, linked to the competition between the crystallographic growth rate V_{hkl} and the advance rate of the solid/liquid front V_s (DebRoy et al. 2018).

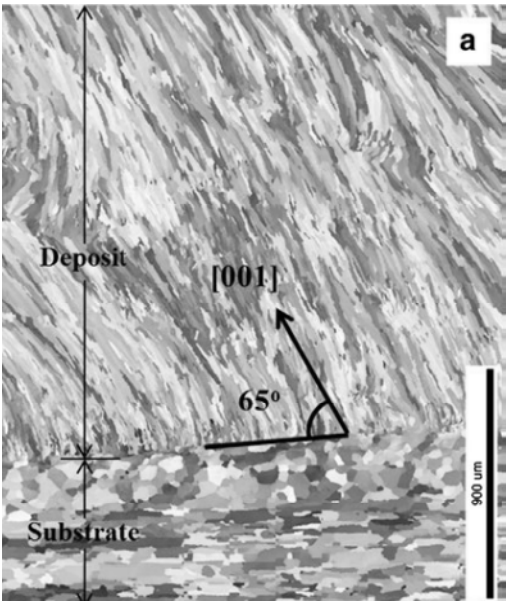

Figure 1.57. *Vertical deviation of columnar structures produced by LMD on aluminum alloy Al-11Si (according to Dinda et al. 2012). For a color version of this figure, see www.iste.co.uk/peyre/alloys2.zip*

The substrate can be heated for high-melting-temperature materials; this is less often the case for aluminum alloys with microstructures similar to those obtained by quenching and which can be tempered directly. As for L-PBF, silicon alloys are very suitable for this technology (Dinda et al. 2012) given their good weldability. On the other hand, AlCuMg or 6XXX series alloys are sensitive to cracking in both LMD

and L-PBF and their microstructure must also be refined by adding silicon, zirconium or scandium (Haldar and Saha 2018).

While the LMD process only enables obtaining a coarse-roughness surface for components with a fine geometry, massive aluminum component edification is preferred, with the opportunity of surface functionalization or finishing by post-treatment (DebRoy et al. 2018). These techniques have also made it possible to advance research in the development of aluminum-based composite materials (Dubourg et al. 2005). The aluminum powders are then mixed with particulate reinforcements during the LMD process. In this context, the problems of adding TiB_2-type grain refiners developed by Ravnikar et al. (2013) overlap, for example, with the problems of grades rich in copper and doped in TiB_2 developed by Du et al. (2018).

1.5.4. *Summary of the microstructures of aluminum alloys*

In summary, as for many of the alloys studied in the previous sections of this chapter, the microstructures of aluminum alloys produced by AM are very different from those obtained by conventional processes due to the rapid solidification and cooling rates.

Among the alloys conventionally produced by L-PBF (AlSi10Mg and AlSi12), a fine cellular microstructure with different sizes in the center and the edge of the melt-pool results from the process. The size of these microstructures is slightly dependent on the process parameters. The grains remain moderate in size, containing several cells, and are oriented in the building direction with epitaxial growth. The range of aluminum alloys that can be produced by L-PBF is gradually expanding, with the aim of high strength alloys for which grain refiners are necessary to avoid hot cracking.

In alloys produced by WAAM, the grain size is larger, and micro-segregation of alloying elements is generally observed due to lower cooling rates. Pore formation is also common, but can be avoided with the use of good quality wire. Hybrid WAAM processes, which include rolling and/or HT, can be implemented to improve the microstructure of deposited alloys.

In the DED processes, due to a lower cooling rate, the grain sizes obtained are larger than with the L-PBF process and the columnar growth is modified by the competition between the speed of the solidification front V_s and the crystallographic growth rate V_{hkl}. The addition of nucleating elements makes it possible to refine the grain size and to deposit (and build) grades known to be difficult to process.

1.6. Conclusion

Metallic materials resulting from AM are characterized by microstructures that differ significantly from those resulting from casting. Among those differences, we can cite the existence of a fine cellular or dendritic substructure presenting (1) local chemical heterogeneities (316L steel, nickel base alloys, aluminum alloys), (2) the stabilization of metastable phases at ambient temperature (residual austenite or ferrite in 17-4PH steels, martensitic phase in TA6V, limited gamma prime precipitation in many nickel base superalloys), (3) the presence of generally columnar grains and (4) a strong crystallographic texture. These characteristics are directly related to the rapid solidification rates and high thermal gradients inherent to AM processes. Thus, the choice of the process and its operating parameters will have a very significant influence on the final microstructure through their effects on the type of solidification (equiaxed dendritic, columnar dendritic, columnar cellular), on the behavior at the segregation during solidification and on the existence of an induced aniso-thermal annealing (case of the TA6V for example) or of annealing imposed by the preheating of the build plate. These raw microstructures can also prove to be effective: for certain materials, the existence of high densities of dislocations of thermal origin after production by L-PBF will induce an increase in the hardness and the elastic limit but to the detriment of ductility. In addition, controlling the solidification conditions makes it possible to create parts with microstructure gradients, presenting, for example, zones made up of equiaxed grains and others of columnar grains. This control of the CET during solidification has already been mastered for DED (the case of TA6V) without requiring the addition of nucleating elements, modifying the composition of the alloy. Research is underway to apply it in the same way to the L-PBF process.

However, AM can also have negative effects on the raw microstructure of the manufactured part. In addition to the existence of porosities, which is however becoming increasingly better controlled through the optimization of process parameters, the working atmosphere and the scanning strategy and also through better knowledge of the effects of powder and melt-pool instabilities, the appearance of residual stresses in the part during construction is one of the weak points of AM. These residual stresses appear during rapid heating–cooling cycles and are particularly damaging in the case of so-called hard-to-weld materials. Indeed, these constraints are, for such materials, present in conjunction with different physicochemical mechanisms which often lead to their deterioration. These include, for example, martensitic transformation in H13 steel, the end of solidification and liquefaction during the rapid temperature rise in Inconel 625 and fine and heavy precipitation in nickel-based alloys with a wide solidification range and a high-volume fraction of precipitation hardening elements, as well as in certain

structural hardening aluminum alloys. However, there has been significant progress in the control and reduction of these residual stresses in recent years, in particular through the development of tools for preheating and mechanical, or even thermo-mechanical, strain hardening between layers. As a result of those progresses, a number of these so-called non-weldable materials can now be produced with AM.

Finally, it should be noted that the vast majority of the materials presented in this chapter are rarely used in their raw manufactured state: thermal post-treatments are necessary, either to reduce residual stresses (annealing for stress relief or relaxation) or to optimize the microstructure with respect to the expected mechanical properties. In the latter case, HTs often include a solution treatment step followed by tempering (or aging), which results in the partial or total disappearance of the microstructure obtained from the process. Restoration treatments conferring a softening of the AM raw material and then recrystallization can also be used if the stored elastic energy associated with the thermal hardening and the temperature of the post-treatment are sufficiently high. These last two restoration phenomena are accompanied by a strong decrease in the dislocation density and possibly by a suppression of the texture of the material, making it isotropic. The treatment temperature at which these phenomena occur becomes lower as the stored elastic energy increases and therefore the dislocation density induced by AM (L-PBF) or imposed by the operator (WAAM) increases. The potential of AM as a microstructure control tool therefore requires the implementation of suitable HTs. This point will be discussed in more detail in Chapter 2.

1.7. References

Aboulkhair, N.T., Everitt, N.M., Ashcroft, I., Tuck, C. (2014). Reducing porosity in AlSi10Mg parts processed by selective laser melting. *Additive Manufacturing*, 1/4, 77–86.

Alnajjar, M., Christien, F., Wolski, K., Bosch, C. (2019). Evidence of austenite by-passing in a stainless steel obtained from laser melting additive manufacturing. *Additive Manufacturing*, 25, 187–195.

Andreau, O., Koutiri, I., Peyre, P., Penot, J.-D., Saintier, N., Pessard, E., De Terris, T., Dupuy, C., Baudin, T. (2019). Texture control of 316L parts by modulation of the melt-pool morphology in selective laser melting. *Journal of Materials Processing Technology*, 264, 21–31.

Andrews, K.C. (1965). Empirical formulae for the calculation of some transformation temperatures. *Journal of the Iron and Steel Institute*, 203, 721–727.

Antonsson, T. and Fredriksson, H. (2005). The effect of cooling rate on the solidification of INCONEL 718. *Metallurgical and Materials Transactions B*, 36(1), 85–96.

Aziz, M.J. (1982). Model for solute redistribution during rapid solidification. *Journal of Applied Physics*, 53(2), 1158–1168.

Bai, J.Y., Yang, C.L., Lin, S.B., Dong, B.L., Fan, C.L. (2015). Mechanical properties of 2219-Al components produced by additive manufacturing with TIG. *International Journal of Advanced Manufacturing Technology*, 86(1/4), 479–485.

Baker, J.C. and Cahn, J.W. (1971). The thermodynamics of solidification, seminar series on solidification. Seminar, ASM.

Bidron, G., Doghri, A., Malot, T., Fournier-dit-Chabert, F., Thomas, M., Peyre, P. (2020). Reduction of the hot cracking sensitivity of CM-247LC superalloy processed by laser cladding using induction preheating. *Journal of Materials Processing Technology*, 277, 116461.

Boettinger, W.J. and Coriell, S.R. (1986). Microstructure formation in rapidly solidified alloys. In *Science and Technology of the Undercooled Melt*, Sahm, P.R., Jones, H., Adam, C.M. (eds). Springer Netherlands, Dordrecht [Online]. Available at: http://link.springer.com/10.1007/978-94-009-4456-5_5 [Accessed 3 November 2020].

Boswell, J.H., Clark, D., Li, W., Attallah, M.M. (2019). Cracking during thermal post-processing of laser powder bed fabricated CM247LC Ni-superalloy. *Materials and Design*, 174, 107793.

Carluccio, D., Bermingham, M.J., Zhang, Y., StJohn, D.H., Yang, K., Rometsch, P.A., Wu, X., Dargusch, M.S. (2018). Grain refinement of laser remelted Al-7Si and 6061 aluminium alloys with Tibor® and scandium additions. *Journal of Manufacturing Processes*, 35, 715–720.

Carozzani, T., Gandin, C.-A., Digonnet, H., Bellet, M., Zaidat, K., Fautrelle, Y. (2013). Direct simulation of a solidification benchmark experiment. *Metallurgical and Materials Transactions A*, 44(2), 873–887.

Carter, L.N., Martin, C., Withers, P.J., Attallah, M.M. (2014). The influence of the laser scan strategy on grain structure and cracking behaviour in SLM powder-bed fabricated nickel superalloy. *Journal of Alloys and Compounds*, 615, 338–347.

Casati, R., Coduri, M., Riccio, M., Rizzi, A., Vedani, M. (2019). Development of a high strength Al–Zn–Si–Mg–Cu alloy for selective laser melting. *Journal of Alloys and Compounds*, 801, 243–253.

Catchpole-Smith, S., Aboulkhair, N., Parry, L., Tuck, C., Ashcroft, I.A., Clare, A. (2017). Fractal scan strategies for selective laser melting of 'unweldable' nickel superalloys. *Additive Manufacturing*, 15, 113–122.

Chauvet, E., Kontis, P., Jägle, E.A., Gault, B., Raabe, D., Tassin, C., Blandin, J.-J., Dendievel, R., Vayre, B., Abed, S., et al. (2018). Hot cracking mechanism affecting a non-weldable Ni-based superalloy produced by selective electron Beam Melting. *Acta Materialia*, 142, 82–94.

Chen, B., Moon, S.K., Yao, X., Bi, G., Shen, J., Umeda, J., Kondoh, K. (2017). Strength and strain hardening of a selective laser melted AlSi10Mg alloy. *Scripta Materialia*, 141, 45–49.

Chen, S., Guillemot, G., Gandin, C.-A. (2016). Three-dimensional cellular automaton-finite element modeling of solidification grain structures for arc-welding processes. *Acta Materialia*, 115, 448–467.

Cline, H.E. and Anthony, T.R. (1977). Heat treating and melting material with a scanning laser or electron beam. *Journal of Applied Physics*, 48(9), 3895–3900.

Cloots, M., Uggowitzer, P.J., Wegener, K. (2016). Investigations on the microstructure and crack formation of IN738LC samples processed by selective laser melting using Gaussian and doughnut profiles. *Materials and Design*, 89, 770–784.

Cong, B., Ding, J., Williams, S.W. (2014). Effect of arc mode in cold metal transfer process on porosity of additively manufactured Al-6.3%Cu alloy. *The International Journal of Advanced Manufacturing Technology*, 76(9/12), 1593–1606.

Dantzig, J.A. and Rappaz, M. (2009). *Solidification*, 1st ed. EPFL Press, Lausanne.

Davis, J.R. (1997). *ASM Speciality Handbook: Heat Resistant Material*. ASM International, Almere.

De Terris, T. (2019). Fabrication additive par fusion laser sélective (SLM) d'un superalliage base nickel : relations procédé-microstructures-propriétés mécaniques. PhD Thesis, École nationale supérieure d'arts et métiers, Paris.

DebRoy, T., Wei, H.L., Zuback, J.S., Mukherjee, T., Elmer, J.W., Milewski, J.O., Beese, A.M., Wilson-Heid, A., De, A., Zhang, W. (2018). Additive manufacturing of metallic components – Process, structure and properties. *Progress in Materials Science*, 92, 112–224.

Dehoff, R.R., Kirka, M.M., Sames, W.J., Bilheux, H., Tremsin, A.S., Lowe, L.E., Babu, S.S. (2015). Site specific control of crystallographic grain orientation through electron beam additive manufacturing. *Materials Science and Technology*, 31(8), 931–938.

Deirmina, F., Peghini, N., AlMangour, B., Grzesiak, D., Pellizzari, M. (2019). Heat treatment and properties of a hot work tool steel fabricated by additive manufacturing. *Materials Science and Engineering: A*, 753, 109–121.

Delroisse, P., Jacques, P.J., Maire, E., Rigo, O., Simar, A. (2017). Effect of strut orientation on the microstructure heterogeneities in AlSi10Mg lattices processed by selective laser melting. *Scripta Materialia*, 141, 32–35.

Dinda, G.P., Dasgupta, A.K., Mazumder, J. (2012). Evolution of microstructure in laser deposited Al–11.28%Si alloy. *Surface and Coatings Technology*, 206(8/9), 2152–2160.

Dobler, S., Lo, T.S., Plapp, M., Karma, A., Kurz, W. (2004). Peritectic coupled growth. *Acta Materialia*, 52(9), 2795–2808.

Doghri, A. (2019). Vers une maîtrise de la réparation par le procédé CLAD de pièces aéronautiques en Inconel 738 LC : compréhensions des mécanismes de fissuration et modélisations associées. PhD thesis, University of Lorraine, Nancy.

Dong, H.B. (2007). Analysis of grain selection during directional solidification of gas turbine blades. *World Congress on Engineering*, July 2–4, London.

Du, R., Gao, Q., Wu, S., Lü, S., Zhou, X. (2018). Influence of TiB2 particles on aging behavior of in-situ TiB2/Al-4.5Cu composites. *Materials Science and Engineering: A*, 721, 244–250.

Dubourg, L., Ursescu, D., Hlawka, F., Cornet, A. (2005). Laser cladding of MMC coatings on aluminium substrate: Influence of composition and microstructure on mechanical properties. *Wear*, 258(11/12), 1745–1754.

DuPont, J.N., Notis, M.R., Marder, A.R., Robino, C.V., Michael, J.R. (1998). Solidification of Nb-bearing superalloys: Part I. Reaction sequences. *Metallurgical and Materials Transactions A*, 29(11), 2785–2796.

Elmer, J.W., Allen, S.M., Eagar, T.W. (1989). Microstructural development during solidification of stainless steel alloys. *Metallurgical Transactions A*, 20(10), 2117–2131.

Facchini, L., Vicente, N., Lonardelli, I., Magalini, E., Robotti, P., Molinari, A. (2010). Metastable austenite in 17-4 precipitation-hardening stainless steel produced by selective laser melting. *Advanced Engineering Materials*, 12(3), 184–188.

de Formanoir, C., Michotte, S., Rigo, O., Germain, L., Godet, S. (2016). Electron beam melted Ti–6Al–4V: Microstructure, texture and mechanical behavior of the as-built and heat-treated material. *Materials Science and Engineering: A*, 652, 105–119.

Gale, W.F. and Totemeier, T.C. (2004). *Smithells Metals Reference Book*, 8th ed. Elsevier Butterworth-Heinemann, Oxford.

Gandin, C.-A. (2000). From constrained to unconstrained growth during directional solidification. *Acta Materialia*, 48(10), 2483–2501.

Gilgien, P., Zryd, A., Kurz, W. (1995). Microstructure selection maps for Al-Fe alloys. *Acta Metallurgica et Materialia*, 43(9), 3477–3487.

Gill, S.C. and Kurz, W. (1995). Rapidly solidified AlCu alloys – II. Calculation of the microstructure selection map. *Acta Metallurgica et Materialia*, 43(1), 139–151.

Gong, X., Lydon, J., Cooper, K., Chou, K. (2014). Beam speed effects on Ti-6Al-4V microstructures in electron beam additive manufacturing. *Journal of Materials Research*, 29(17), 1951–1959.

Gremaud, M. (1990). Solidification rapide : étude microstructurale des alliages Al-Fe après refusion superficielle par laser. PhD thesis, EPFL, Lausanne.

Gu, J., Ding, J., Cong, B., Bai, J., Gu, H., Williams, S.W., Zhai, Y. (2014). The influence of wire properties on the quality and performance of wire+arc additive manufactured aluminium parts. *Advanced Materials Research*, 1081, 210–214.

Gu, J., Ding, J., Williams, S.W., Gu, H., Ma, P., Zhai, Y. (2016a). The effect of interlayer cold working and post-deposition heat treatment on porosity in additively manufactured aluminum alloys. *Journal of Materials Processing Technology*, 230, 26–34.

Gu, J., Ding, J., Williams, S.W., Gu, H., Bai, J., Zhai, Y., Ma, P. (2016b). The strengthening effect of inter-layer cold working and post-deposition heat treatment on the additively manufactured Al–6.3Cu alloy. *Journal of Materials Processing Technology*, 230, 26–34.

Gu, J., Wang, X., Bai, J., Ding, J., Williams, S., Zhai, Y., Liu, K. (2018). Deformation microstructures and strengthening mechanisms for the wire+arc additively manufactured Al-Mg4.5Mn alloy with inter-layer rolling. *Materials Science and Engineering A*, 712, 292–301.

Guraya, T., Singamneni, S., Chen, Z.W. (2019). Microstructure formed during selective laser melting of IN738LC in keyhole mode. *Journal of Alloys and Compounds*, 792, 151–160.

Haldar, B. and Saha, P. (2018). Identifying defects and problems in laser cladding and suggestions of some remedies for the same. *Materials Today: Proceedings*, 5(5), 13090–13101.

Hann, D.B., Iammi, J., Folkes, J. (2011). A simple methodology for predicting laser-weld properties from material and laser parameters. *Journal of Physics D: Applied Physics*, 44(44), 445401.

Hosseini, E. and Popovich, V.A. (2019). A review of mechanical properties of additively manufactured Inconel 718. *Additive Manufacturing*, 30, 100877.

Hunt, J.D. (1984). Steady state columnar and equiaxed growth of dendrites and eutectic. *Materials Science and Engineering*, 65(1), 75–83.

Hunziker, O. and Kurz, W. (1999). Directional solidification and phase equilibria in the Ni-Al system. *Metallurgical and Materials Transactions A*, 30(12), 3167–3175.

Hunziker, O., Vandyoussefi, M., Kurz, W. (1998). Phase and microstructure selection in peritectic alloys close to the limit of constitutional undercooling. *Acta Materialia*, 46(18), 6325–6336.

Jägle, E., Sheng, Z., Kürnsteiner, P., Ocylok, S., Weisheit, A., Raabe, D. (2016). Comparison of maraging steel micro- and nanostructure produced conventionally and by laser additive manufacturing. *Materials*, 10(1), 8.

Kempen, K., Yasa, E., Thijs, L., Kruth, J.-P., Van Humbeeck, J. (2011). Microstructure and mechanical properties of selective laser melted 18Ni-300 steel. *Physics Procedia*, 12, 255–263.

Koepf, J.A., Soldner, D., Ramsperger, M., Mergheim, J., Markl, M., Körner, C. (2019). Numerical microstructure prediction by a coupled finite element cellular automaton model for selective electron beam melting. *Computational Materials Science*, 162, 148–155.

Körner, C., Helmer, H., Bauereiß, A. (2014). *Tailoring the Grain Structure of IN718 during Selective Electron Beam Melting.* EDP Sciences, Les Ulis.

Kou, S. (2003). *Welding Metallurgy*, 2nd ed. John Wiley, New York.

Kreitcberg, A., Brailovski, V., Turenne, S. (2017). Effect of heat treatment and hot isostatic pressing on the microstructure and mechanical properties of Inconel 625 alloy processed by laser powder bed fusion. *Materials Science and Engineering: A*, 689, 1–10.

Kurz, W. and Fisher, D.J. (1998). *Fundamentals of Solidification*, 4th ed. Trans Tech Publications, Zurich.

Kurz, W. and Trivedi, R. (1996). Banded solidification microstructures. *Metallurgical and Materials Transactions A*, 27(3), 625–634.

Lei, Z., Bi, J., Chen, Y., Chen, X., Qin, X., Tian, Z. (2019). Effect of energy density on formability, microstructure and micro-hardness of selective laser melted Sc- and Zr-modified 7075 aluminum alloy. *Powder Technology*, 356, 594–606.

Leriche, N., Combeau, H., Gandin, C.-A., Založnik, M. (2015). Modelling of columnar-to-equiaxed and equiaxed-to-columnar transitions in ingots using a multiphase model. *IOP Conference Series: Materials Science and Engineering*, 84, 012087.

Liu, X., Zhao, C., Zhou, X., Shen, Z., Liu, W. (2019). Microstructure of selective laser melted AlSi10Mg alloy. *Materials and Design*, 168, 107677.

Maisonneuve, J. (2008). Fabrication directe de pièces aéronautiques en TA6V et IN718 : projection et fusion sélective par laser. PhD thesis, École nationale supérieure des Mines de Paris, Paris.

Marchese, G., Lorusso, M., Parizia, S., Bassini, E., Lee, J.-W., Calignano, F., Manfredi, D., Terner, M., Hong, H.-U., Ugues, D., et al. (2018). Influence of heat treatments on microstructure evolution and mechanical properties of Inconel 625 processed by laser powder bed fusion. *Materials Science and Engineering: A*, 729, 64–75.

Martin, J.H., Yahata, B.D., Hundley, J.M., Mayer, J.A., Schaedler, T.A., Pollock, T.M. (2017). 3D printing of high-strength aluminium alloys. *Nature*, 549(7672), 365–369.

Martina, F., Williams, S.W., Colegrove, P. (2013). Improved microstructure and increased mechanical properties of additive manufacture produced Ti-6Al-4V by interpass cold rolling. *SFF Symposium*, August, Austin, USA.

Martorano, M.A., Beckermann, C., Gandin, C.-A. (2003). A solutal interaction mechanism for the columnar-to-equiaxed transition in alloy solidification. *Metallurgical and Materials Transactions A*, 34(8), 1657–1674.

Montero-Sistiaga, M.L., Mertens, R., Vrancken, B., Wang, X., Van Hooreweder, B., Kruth, J.-P., Van Humbeeck, J. (2016). Changing the alloy composition of Al7075 for better processability by selective laser melting. *Journal of Materials Processing Technology*, 238, 437–445.

Mullins, W.W. and Sekerka, R.F. (1964). Stability of a planar interface during solidification of a dilute binary alloy. *Journal of Applied Physics*, 35(2), 444–451.

Murr, L.E., Gaytan, S.M., Ramirez, D.A., Martinez, E., Hernandez, J., Amato, K.N., Shindo, P.W., Medina, F.R., Wicker, R.B. (2012). Metal fabrication by additive manufacturing using laser and electron beam melting technologies. *Journal of Materials Science and Technology*, 28(1), 1–14.

Ojo, O.A., Richards, N.L., Chatuverdi, M.C. (2006). Study of the fusion zone and heat-affected zone microstructures in tungsten inert gas-welded Inconel 738LC superalloy. *Metallurgical and Materials Transactions A: Physical Metallurgy and Materials Science*, 37(2), 421–433.

Parimi, L.L., Ravi, G.A., Clark, D., Attallah, M.M. (2014). Microstructural and texture development in direct laser fabricated IN718. *Materials Characterization*, 89, 102–111.

Pineau, A., Guillemot, G., Reinhart, G., Regula, G., Mangelinck-Noël, N., Gandin, C.-A. (2020). Three-dimensional cellular automaton modeling of silicon crystallization with grains in twin relationships. *Acta Materialia*, 191, 230–244.

Pinter, Z. (2017). Study of wire + arc additive manufacturing. PhD thesis, University of Cranfield, Cranfield.

Pröbstle, M., Neumeier, S., Hopfenmüller, J., Freund, L.P., Niendorf, T., Schwarze, D., Göken, M. (2016). Superior creep strength of a nickel-based superalloy produced by selective laser melting. *Materials Science and Engineering: A*, 674, 299–307.

Rafi, H.K., Pal, D., Patil, N., Starr, T.L., Stucker, B.E. (2014). Microstructure and mechanical behavior of 17-4 precipitation hardenable steel processed by selective laser melting. *Journal of Materials Engineering and Performance*, 23(12), 4421–4428.

Ramsperger, M., Singer, R.F., Körner, C. (2016). Microstructure of the nickel-base superalloy CMSX-4 fabricated by selective electron beam melting. *Metallurgical and Materials Transactions A*, 47(3), 1469–1480.

Ravnikar, D., Dahotre, N.B., Grum, J. (2013). Laser coating of aluminum alloy EN AW 6082-T651 with TiB2 and TiC: Microstructure and mechanical properties. *Applied Surface Science*, 282, 914–922.

Rosenthal, D. (1946). The theory of moving sources of heat and its application to metal treatments. *Transactions of the A.S.M.E*, 68, 849–865.

Royer, F. (2014). Fonctionnement et singularités du procédé de fusion laser sélective : Illustration par application à deux superalliages à base nickel et considérations énergétiques. PhD thesis, École nationale supérieure des Mines de Paris, Paris.

Ryan, E.M., Sabin, T.J., Watts, J.F., Whiting, M.J. (2018). The influence of build parameters and wire batch on porosity of wire and arc additive manufactured aluminium alloy 2319. *Journal of Materials Processing Technology*, 262, 577–584.

Scipioni Bertoli, U., Wolfer, A.J., Matthews, M.J., Delplanque, J.-P.R., Schoenung, J.M. (2017). On the limitations of volumetric energy density as a design parameter for selective laser melting. *Materials and Design*, 113, 331–340.

Senninger, O., Gandin, C.-A., Guillemot, G. (2018). Modeling of eutectic growth kinetics with thermodynamic couplings. *Acta Materialia*, 161, 110–126.

Simonelli, M., Tse, Y.Y., Tuck, C. (2012). Microstructure of Ti-6Al-4V produced by selective laser melting. *Journal of Physics: Conference Series*, 371, 012084.

Spierings, A.B., Dawson, K., Heeling, T., Uggowitzer, P.J., Schäublin, R., Palm, F., Wegener, K. (2017). Microstructural features of Sc- and Zr-modified Al-Mg alloys processed by selective laser melting. *Materials and Design*, 115, 52–63.

Spierings, A.B., Dawson, K., Dumitraschkewitz, P., Pogatscher, S., Wegener, K. (2018). Microstructure characterization of SLM-processed Al-Mg-Sc-Zr alloy in the heat treated and HIPed condition. *Additive Manufacturing*, 20, 173–181.

Sun, Z., Tan, X., Tor, S.B., Yeong, W.Y. (2016). Selective laser melting of stainless steel 316L with low porosity and high build rates. *Materials & Design*, 104, 197–204.

Takata, N., Kodaira, H., Sekizawa, K., Suzuki, A., Kobashi, M. (2017). Change in microstructure of selectively laser melted AlSi10Mg alloy with heat treatments. *Materials Science and Engineering: A*, 704, 218–228.

Thijs, L., Kempen, K., Kruth, J.-P., Van Humbeeck, J. (2013). Fine-structured aluminium products with controllable texture by selective laser melting of pre-alloyed AlSi10Mg powder. *Acta Materialia*, 61(5), 1809–1819.

Tourret, D., Reinhart, G., Gandin, C.-A., Iles, G.N., Dahlborg, U., Calvo-Dahlborg, M., Bao, C.M. (2011). Gas atomization of Al–Ni powders: Solidification modeling and neutron diffraction analysis. *Acta Materialia*, 59(17), 6658–6669.

Turnbull, D. (1962). On the relation between crystallization rate and liquid structure. *The Journal of Physical Chemistry*, 66(4), 609–613.

Vandyoussefi, M., Kerr, H.W., Kurz, W. (2000). Two-phase growth in peritectic Fe–Ni alloys. *Acta Materialia*, 48(9), 2297–2306.

Vinson, P. (2015). Fusion sélective par laser de lits de poudre : étude sur le recyclage de la poudre et détection de défauts au cours de la fabrication par imagerie thermique. PhD thesis, Mines Paris Tech, Paris.

Wang, H., Zhang, X., Wang, G.B., Shen, J., Zhang, G.Q., Li, Y.P., Yan, M. (2019). Selective laser melting of the hard-to-weld IN738LC superalloy: Efforts to mitigate defects and the resultant microstructural and mechanical properties. *Journal of Alloys and Compounds*, 807, 151662.

Wang, N., Mokadem, S., Rappaz, M., Kurz, W. (2004). Solidification cracking of superalloy single- and bi-crystals. *Acta Materialia*, 52(11), 3173–3182.

Wang, Y.M., Voisin, T., McKeown, J.T., Ye, J., Calta, N.P., Li, Z., Zeng, Z., Zhang, Y., Chen, W., Roehling, T.T., et al. (2018). Additively manufactured hierarchical stainless steels with high strength and ductility. *Nature Materials*, 17(1), 63–71.

Wu, J., Wang, X.Q., Wang, W., Attallah, M.M., Loretto, M.H. (2016). Microstructure and strength of selectively laser melted AlSi10Mg. *Acta Materialia*, 117, 311–320.

Yu, G., Gu, D., Dai, D., Xia, M., Ma, C., Shi, Q. (2016). On the role of processing parameters in thermal behavior, surface morphology and accuracy during laser 3D printing of aluminum alloy. *Journal of Physics D: Applied Physics*, 49(13), 135501.

Zhang, F., Levine, L.E., Allen, A.J., Campbell, C.E., Lass, E.A., Cheruvathur, S., Stoudt, M.R., Williams, M.E., Idell, Y. (2017a). Homogenization kinetics of a nickel-based superalloy produced by powder bed fusion laser sintering. *Scripta Materialia*, 131, 98–102.

Zhang, H., Zhu, H., Nie, X., Yin, J., Hu, Z., Zeng, X. (2017b). Effect of zirconium addition on crack, microstructure and mechanical behavior of selective laser melted Al-Cu-Mg alloy. *Scripta Materialia*, 134, 6–10.

Zhao, L., Santos Macías, J.G., Ding, L., Idrissi, H., Simar, A. (2019). Damage mechanisms in selective laser melted AlSi10Mg under as built and different post-treatment conditions. *Materials Science and Engineering: A*, 764, 138210.

Zhou, L., Mehta, A., Schulz, E., McWilliams, B., Cho, K., Sohn, Y. (2018). Microstructure, precipitates and hardness of selectively laser melted AlSi10Mg alloy before and after heat treatment. *Materials Characterization*, 143, 5–17.

Zimmermann, M. (1990). Solidification rapide de l'eutectique Al-Al2Cu par refusion laser. PhD thesis, EPFL, Lausanne.